

Università degli Studi di Genova, Facoltà di Fisica

**Measurements with the Upgraded Counting Test
Facility (CTF-2) of the Solar Neutrino
Experiment Borexino**

Elisa Resconi

Internal Advisor, Prof. Giulio Manuzio

External Advisor, Dr. R.S. Raghavan

Genova, February 2001

Introduction

Wolfgang Pauli in a private letter dated December, 1930 suggested for the first time the existence of the neutrino in order to solve an apparent violation of the energy conservation in nuclear β decay. In 1934 Enrico Fermi proposed a theory of β decay where the interaction occurred at a point. During the same year Bethe and Critchfield described the role of β decay in thermonuclear reaction chains powering the stars

$$(A, Z) \rightarrow (A, Z - 1) + e^+ + \nu_e \quad (1)$$

predicting that the sun is a powerful source of neutrinos. In 1956 Cowan and Reines detected for the first time neutrinos coming from a reactor. In 1957 the weak interaction mediating neutrino interactions was found to violate parity maximally. Later experiments found that three generations of neutrinos exist each accompanying a distinct charged lepton: $(\nu_e, e^-), (\nu_\mu, \mu^-), (\nu_\tau, \tau^-)$. After all this development the standard electroweak model succeeded in describing neutrino interactions with other particles.

Despite all this progress, different questions remain. On the base of solar and atmospheric neutrino observation we now believe that neutrinos are massive but no measurement of an absolute neutrino mass was yet realized. We do not understand why neutrino masses are so small and we do not know the particle-antiparticle conjugation properties of neutrinos. Finally, there are many questions about the role of neutrinos in astrophysics and cosmology. It is possible that cosmic background neutrinos contribute to dark matter and may influence large-scale structure formation. Supernova models predict that neutrinos play an essential role in the explosion mechanism and in the associated nucleosynthesis but there is disagreement about the success of neutrino driven explosion. Moreover there is a great interest in searches for very high energy astrophysical neutrinos that might be associated with active galactic nuclei, gamma ray burst, etc.

A unique beam ($10^{10}cm^{-2}s^{-1}$) of low energy (0-10 MeV) neutrino is constantly produced inside the sun. The detection of solar neutrinos on the earth allows the study of Δm^2 to values low as $10^{-12}eV^2$. Five different experiments reported until now solar neutrino detection. It is possible to show in a model independent way that the results of different solar neutrino experiments are not compatible if we assume no neutrino mixing. If neutrinos were standard particles, i.e. no oscillations occurred,

the combined analysis of the different experiments results in a strong suppression of the ${}^7\text{Be}$ neutrinos. Neutrino oscillation is the favored scenario to explain the experimental findings. The direct observation of the monoenergetic ${}^7\text{Be}$ neutrinos will discriminate amongst the different oscillation scenarios.

The Borexino experiment is designed in order to study solar neutrinos in the energy region of the ${}^7\text{Be}$ line (860 keV). Neutrinos are detected via elastic scattering on electrons. The electrons are contained in a liquid scintillator that works both as target and detector medium. Due to the very small $\nu - e$ cross section (10^{-44}cm^{-2} at 0.5 MeV) the target mass must be large. In Borexino 300 tons of liquid scintillator are used of which a fiducial volume of ~ 100 tons is defined by software. The main source of background in the energy region of interest (0.25-1 MeV for the scattered electron) is the natural radioactivity. For this reason the detector is designed in order to reduce the contamination. Ultra low level of ${}^{238}\text{U}$, ${}^{232}\text{Th}$, ${}^{40}\text{K}$, ${}^{222}\text{Rn}$ and other radioactive isotopes are requested. Different developments were realized by the collaboration in order to reach and detect such low level of trace contaminations. A key instrument in this development is the Counting Test Facility (CTF) of Borexino, a prototype detector with a mass of 5 tons.

The CTF was installed in Hall C of the Gran Sasso Underground Laboratories (LNGS) during '95. The main objective of the first period of data taking ('95-'97) was to show that ultra-low levels of radio contaminants as ${}^{238}\text{U}$, ${}^{232}\text{Th}$, ${}^{14}\text{C}$ etc. were achievable. After detection of ${}^{238}\text{U}$, ${}^{232}\text{Th}$ at levels of 10^{-16} g/g and ${}^{14}\text{C}/{}^{12}\text{C}$ at 10^{-18} Borexino was approved and the installation in underground started. Now, the main goal of CTF is to perform tests of the auxiliary systems of Borexino (purification processes, liquid handling etc.) and to be used for quality control of the liquid scintillator prior to the filling of Borexino. In particular, the intrinsic contamination of ${}^{14}\text{C}$ represents an unpredictable source of background that will determine the low energy threshold in Borexino.

Liquid scintillators studied for Borexino are derived from petroleum. Due to the long period that petroleum sits in its reservoir the ${}^{14}\text{C}$ originally present had time to decay away. The abundances of ${}^{14}\text{C}$ expected in CTF are orders of magnitude lower than the levels measured. In collaboration with Dr. S. Schönert I studied the underground production of ${}^{14}\text{C}$ in petroleum. Neutrons which are produced in the petroleum reservoir from natural radioactivity interact with ${}^{14}\text{N}$, ${}^{17}\text{O}$, ${}^{13}\text{C}$ and

^{11}B producing ^{14}C . The average natural radioactivity levels in petroleum sites, the nitrogen percentage and the typical rock composition were the input of the model. We evaluated that levels of $^{14}\text{C}/^{12}\text{C}$ down to 10^{-17} can be explained with *in-situ* underground production. In this dissertation I describe the basic production reactions, the underground neutron flux induced by natural radioactivity and some basic concepts of petroleum.

During the year '98, at the beginning of this doctorate project, the Borexino collaboration decided to restart data taking with CTF. Different upgrades were needed. I coordinated the various phases of the installation and start-up of the CTF-2. In collaboration with the PMT working group a new waterproof sealing design for the PMTs was developed. Accelerating aging and water pressure tests were applied in order to qualify the underwater performance of the PMTs. I contributed to the qualification tests, sealing and installation of the 100 PMTs and collaborated during the installation of the 100 new signal and HV cables. I also helped the Inner Vessel working group during the installation of the new scintillator containment vessel and radon barrier. All the installation was realized in clean room atmosphere. I was one of the shifter during the water filling of the detector. In this thesis details of this operations are reported.

After few *water* runs devoted to Čerenkov event discrimination a PXE scintillator test started. I followed all the data taking and realized part of the data analysis. The main characteristics of this liquid scintillator are summarized.

Contents

Introduction	i
1 Neutrino Physics	1
1.1 Neutrino Mixing	1
1.2 Neutrino Oscillation in Vacuum and in Matter	2
1.3 Solar Neutrinos	5
2 Borexino: Physics Goals and Detector Design	16
2.1 Physics Goals	16
2.1.1 Neutrino Signal	17
2.1.2 Internal Background	19
2.1.3 External Background	25
2.1.4 Surface Background	25
2.2 Borexino Detector	26
2.2.1 Internal Structure	27
2.2.2 Auxiliary Systems	31
3 Underground Production of ^{14}C in Petroleum	34
3.1 Petroleum and Petroleum Sites: Basic Concepts	34
3.2 The Role of Nitrogen	36
3.3 Radioactivity of the Petroleum Reservoir	38
3.4 Underground Neutron Flux	42
3.5 Underground ^{14}C Production	44
3.6 Conclusion	46
4 The Counting Test Facility (CTF) of Borexino	54
4.1 Feasibility of Borexino: CTF-1	55
4.1.1 Structure of the Detector	55

4.1.2	Results Achieved	57
4.2	Quality Control of Borexino: CTF-2	59
4.2.1	PMT: Characteristics, Sealing and Test.	59
4.2.2	Cables and Connectors	67
4.2.3	Electronic and DAQ System	70
4.2.4	Inner Vessel (IV) and Outer Vessel(OV)	71
4.2.5	Water System and Nitrogen System	71
4.2.6	CTF-2 Fluid Handling and Purification Systems	71
4.3	Cleaning and Assembling: the Installation of CTF-2	73
4.3.1	Cleaning Procedures Applied	74
4.3.2	Installation Inside CTF Tank	75
4.4	Water Filling and Water Data Taking	76
4.4.1	Start Data Taking: Čerenkov Event Identification	79
5	PXE Characterisation in CTF-2	87
5.1	First and Second Partial Fillings	88
5.1.1	Radon Level Inserted During Fillings	92
5.1.2	Energy Calibration	92
5.1.3	Čerenkov Events Identification	94
5.1.4	Abundance of ^{14}C	95
5.2	Completion of the Filling	99
5.2.1	Radon Inserted During Filling	99
5.2.2	α/β Discrimination Efficiency of PXE	100
5.2.3	^{40}K Contamination	105
5.2.4	Limit of ^{238}U Contents in PXE	108
5.3	Final Results: Single Counts	114
A	Description of the Data Taking	121
	Acknowledgments	124

Neutrino Physics

There is now rather convincing evidence that neutrinos have nonzero masses. This evidence comes from the apparent observation of neutrino oscillation. I recall here few basic concepts of the physics of this phenomenon, and its relation to neutrino mass.

1.1 Neutrino Mixing

The Lagrangian of interaction of neutrino with other particles in the Standard Model of electroweak interaction is:

$$L_{CC} = -\frac{g}{2\sqrt{2}}j_{\alpha}^{CC}W^{\alpha} + h.c. \quad (1.1)$$

$$L_{NC} = -\frac{g}{2}\cos\theta_W j_{\alpha}^{NC}Z^{\alpha} + h.c. \quad (1.2)$$

where g is the electroweak interaction constant, θ_W is the Weinberg angle and W^{α} and Z^{α} are the fields of the W^{\pm} and Z^0 vector bosons. A complete discussion about neutrino mixing and oscillation can be found in [1, 2]. I report here only highlights which are useful for the following discussion.

If neutrino masses are equal to zero, as within like the Standard Model of electroweak interaction, charge current (CC) and neutral current (NC) interactions conserve electron, muon and tauon lepton numbers. Introducing the hypothesis that neutrino has mass, the neutrinos are mixed, and neutrino mass term does not conserve lepton numbers. In general, neutrino mass term can be of two different types:

- *Dirac neutrino*: if neutrino mass term is generated by the same standard Higgs mechanism that produce quark and charged lepton masses, the neutrino mass

term does not destroy the global gauge invariance of the total Lagrangian. The consequence is that the total lepton number $L = L_e + L_\mu + L_\tau$ is conserved. Neutrino with definite masses are four-component Dirac particles and neutrino and antineutrino have different sign of L .

- *Majorana neutrino*: in the framework of theories beyond the Standard Model like the Grand Unified SO(10) Model the total lepton number is not conserved. Neutrino mass term is in this case a linear combination of the products of left and right handed components of neutrino fields. Neutrino with definite mass are two-component Majorana particles. In this case, neutrino and antineutrino can be distinguished.

1.2 Neutrino Oscillation in Vacuum and in Matter

A direct consequence of neutrino mixing is flavour conversion. B. Pontecorvo [3] proposed for the first time the idea of neutrino - antineutrino oscillation. Flavour oscillations were later introduced. In case of neutrino mixing hypothesis

$$\nu_{\alpha L} = \sum_i U_{\alpha i} \nu_{i L}. \quad (1.3)$$

where U is the mixing matrix called "Maki-Nakagawa-Sakata matrix" [4] and ν_i is the field of neutrino (Dirac or Majorana) with mass m_i . The fields $\nu_{\alpha L}$ are flavor fields ($\alpha = e, \mu, \tau$): if $|\nu_i\rangle$ is the vector of state of neutrino with momentum p and energy E_i we can write:

$$|\nu_\alpha\rangle = \sum_i U_{\alpha i}^* |\nu_i\rangle. \quad (1.4)$$

If at the initial time $t = 0$ the state of neutrino is $|\nu_\alpha\rangle$ the neutrino at the time t can be written as:

$$|\nu_\alpha\rangle_t = \sum_i U_{\alpha i}^* e^{-iE_i t} |\nu_i\rangle. \quad (1.5)$$

The vector $|\nu_\alpha\rangle$ is the superposition of all types of neutrino states. Using the unitarity condition of the mixing matrix we can write

$$|\nu_i\rangle = \sum_{\alpha'} U_{\alpha' i} |\nu_{\alpha'}\rangle. \quad (1.6)$$

The evolution in time of the neutrino state is then

$$|\nu_\alpha\rangle_t = \sum_{\alpha'} |\nu_{\alpha'}\rangle A_{\nu'_{\alpha};\nu_\alpha}(t). \quad (1.7)$$

where A is the amplitude of the transition $\nu_\alpha \rightarrow \nu_{\alpha'}$

$$A_{\nu'_{\alpha};\nu_\alpha}(t) = \sum_i U_{\alpha'i} e^{-iE_i t} U_{\alpha i}^*. \quad (1.8)$$

We now concentrate on the case of oscillations between two neutrinos. The amplitude of the transition is:

$$A_{\alpha';\alpha} = 4|U_{\alpha'2}|^2|U_{\alpha 2}|^2. \quad (1.9)$$

Due to unitarity of the mixing matrix

$$|U_{\alpha'2}|^2 + |U_{\alpha 2}|^2 = 1. \quad (1.10)$$

If θ is the mixing angle we have $|U_{\alpha 2}|^2 = \sin^2 \theta$ and $|U_{\alpha'2}|^2 = \cos^2 \theta$ thus the oscillation amplitude is

$$A_{\alpha';\alpha} = \sin^2 2\theta. \quad (1.11)$$

The transition probability can be evaluated from the oscillation amplitude and in case of two neutrinos has the form:

$$P(\nu_\alpha \rightarrow \nu_{\alpha'}) = \frac{1}{2} \sin^2 2\theta \left(1 - \cos 2\pi \frac{L}{L_0}\right) \quad (1.12)$$

where L_0 is the oscillation length

$$L_0 = 4\pi \frac{E}{\Delta m^2} \quad (1.13)$$

The transition probability can be written in the common used formula

$$P(\nu_\alpha \rightarrow \nu_{\alpha'}) = \frac{1}{2} \sin^2 2\theta \left(1 - \cos 2.54 \Delta m^2 \frac{L}{E}\right) \quad (1.14)$$

where Δm^2 is neutrino mass square difference ($m_1^2 - m_2^2$) in eV^2 , L is the distance in m (km) and E is the neutrino energy in MeV (GeV). The transition probability depends periodically on L/E. In order to see neutrino oscillation it is necessary that the condition $\Delta m^2(\frac{L}{E}) \geq 1$ is satisfied. From this condition we can estimate the minimal value of the parameter Δm^2 that can be revealed in an experiment on the

search of neutrino oscillation. These values are summarized in Tab. 1.1.

Neutrino Source	L/E (m/MeV)	$\Delta m^2 (eV^2)$
Reactor	$1 - 10^2$	$10^{-3} - 10^{-1}$
Accelerator	$10^{-2} - 10$	$10^{-2} - 10$
Atmospheric	$10^2 - 10^4$	$10^{-5} - 10^{-3}$
Solar	$10^{10} - 10^{11}$	$10^{-12} - 10^{-11}$
Supernova	$10^{19} - 10^{20}$	$10^{-20} - 10^{-21}$

Table 1.1: Sensitivity of neutrino oscillation experiments [5] using different neutrino sources.

If the neutrinos pass through a significant amount of matter the transition between different types of neutrinos can in some cases be enhanced [7, 8]. This is called MSW effect from the name of the physicists Mikheyev, Smirnov and Wolfenstein. The interaction of neutrinos with matter is accounted in the propagated wave function by the refraction index n

$$\Psi(x, t) = \sum_{i=1,3} U_{\alpha i} \nu_i e^{-i(E_i t - p x)}. \quad (1.15)$$

The refraction index of neutrino depends on the amplitude of elastic neutrino scattering in forward direction $f(0)$ and on the density of matter $\rho(x)$

$$n(x) = 1 + \frac{2\pi}{p^2} f(0) \rho(x). \quad (1.16)$$

When neutrinos pass through matter, they can interact via neutral current interaction (NC) or charge current interaction (CC). NC scattering of neutrinos on electrons and nucleons does not change the flavour state of neutrinos. CC interaction gives contribution only to the amplitude of the elastic $\nu_e - e^-$ scattering

$$\nu_e + e^- \rightarrow \nu_e + e^- \quad (1.17)$$

In other words, the contribution to the amplitude of neutrino scattering mediated by W^\pm is present only for electron neutrinos, whereas the contribution corresponding to the interaction mediated by Z_0 is flavour independent. The electron neutrino wave

function phase varies in space with respect to the other neutrinos. The electron-neutrino interaction length $L_{e\nu}$ is the length at which the phase difference equals 2π (resonant condition)

$$L_{e\nu} = \frac{2\pi}{\sqrt{2}G_F\rho_e} \quad (1.18)$$

$$L_{e\nu}(m) = \frac{1.7 \cdot 10^7}{\rho(g/cm^3)(Z/A)} \quad (1.19)$$

and it amounts to ~ 200 km in the sun's core and to $\sim 10^4$ km in the Earth. In a variable density medium like the sun, the minimal mass that can be explored is fixed by three scales of the nuclear energies and by the electron density in the sun's core

$$\Delta m^2 \sim 10^{-5} eV^2. \quad (1.20)$$

1.3 Solar Neutrinos

Convincing evidences of neutrino oscillation come from the observation of atmospheric neutrinos [6] and strong indication of neutrino mixing comes from all the experiments that observe solar neutrinos. I will summarize here the experimental status on the search for solar neutrino oscillations. For details about solar neutrino experiments I will refer to [17].

The sun is a powerful source of neutrinos with unique potentialities for the study of neutrino oscillation due to its far distant location. Via solar neutrino study it is possible to test vacuum oscillation hypothesis in a range of Δm^2 much lower than with a terrestrial source. Solar neutrinos allow also the study of resonant oscillation in matter (MSW effect).

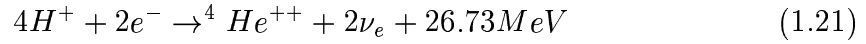
The stellar model for the sun, called Standard Solar Model (SSM) [9, 15] corresponds to a solution of the evolution equation of the star. It is based on the fundamental assumption that the sun is a Main Sequence star, spherical and in hydrostatic equilibrium between gravity and the radiative pressure produced by the thermonuclear reactions in its core. It gives a quantitative description of the sun and traces the evolution of the star over the past 4.7 billion years. It is based upon results of solar observations, laboratory measurements of nuclear reaction cross sections and

theoretical predictions. The main assumptions are:

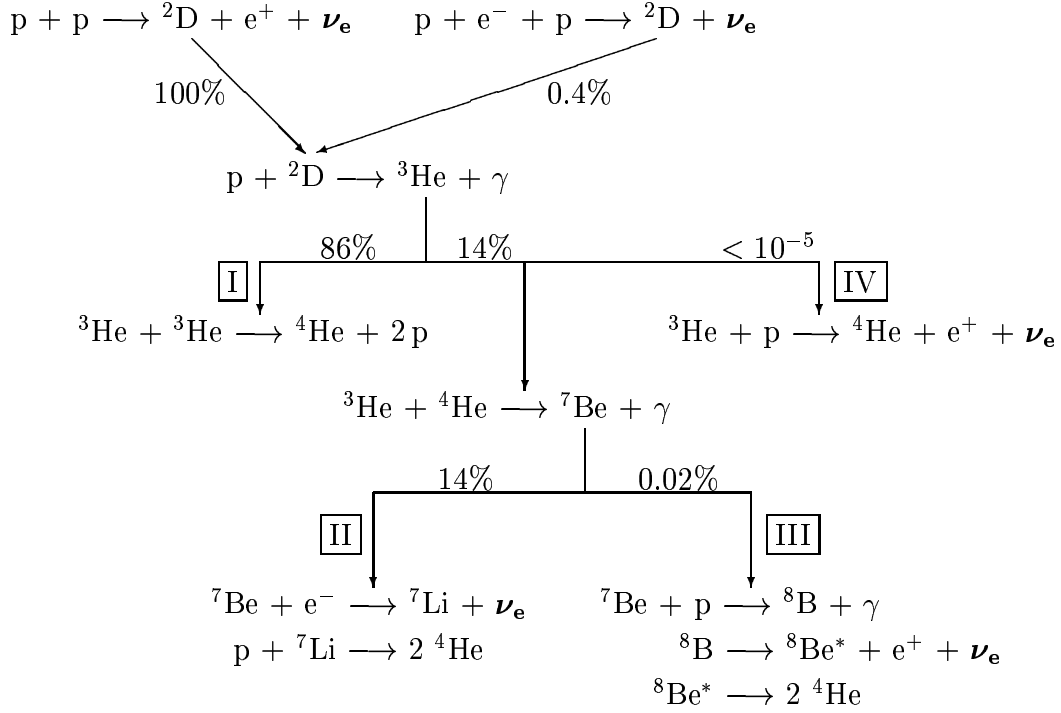
- the sun evolves in hydrostatic equilibrium. Gravitational force and pressure gradient are balanced. The equation of state is a function of temperature, density, and composition;
- energy is transported by radiation and convection. In the solar envelope the energy is transported in a convective way while radiative transport dominates in the core region where thermonuclear reactions take place;
- thermonuclear reaction chains generate solar energy;
- the model is constrained to produce today's solar radius, mass, and luminosity.

The distribution of temperature, density, energy production and elemental abundances of light elements in the sun's core are some of the predictions that the model produce. The accuracy of the model predictions has been checked on experimental data. From the observation of helioseismic activity one can extract the distribution of the sound speed in the sun's interior. The BBP'98 solar standard model prediction of this distribution agrees with the experimental observation [9].

The energy of the sun is generated in the reactions of the thermonuclear pp and CNO cycles. The SSM predicts that over 98% of the energy is produced from the pp chain, i.e. the fusion of Hydrogen atoms into α particles, with the associated production of positrons and neutrinos:



The remaining 2% come from the burning through the CNO cycle. While most of the released energy is carried by photons, 3% of it is emanated in the form of low energy neutrinos. The pp-cycle is illustrated in the graph below and the energy spectra of the generated neutrino in Fig. 1.1. The principal sources of solar neutrinos are described in Tab. 1.2.



Reaction	Maximal Energy (MeV)	SSM flux ($cm^{-2}s^{-1}$)
$pp \rightarrow de^+\nu_e$	≤ 0.42	$5.94(1.00 \pm 0.01) \cdot 10^{10}$
${}^7\text{Be}e^- \rightarrow {}^7\text{Li}\nu_e + (\gamma)$	0.86 (90%)	$4.80(1.00 \pm 0.09) \cdot 10^9$
${}^8\text{B} \rightarrow {}^8\text{Be}^*e^+\nu_e$	≤ 14	$5.15(1.00^{+0.19}_{-0.14}) \cdot 10^6$

Table 1.2: Main investigated sources of solar ν_e [9]. The predicted flux uncertainty reflects primarily the different degrees of model dependence for the different neutrino branches.

Up to now, five different experiments have measured solar neutrinos. The results achieved from the solar neutrino experiments are reported in Tab. 1.3.

The Sudbury Neutrino Observatory (SNO) [16], a new realtime solar neutrino experiment which aims to discriminate between charged current and neutral current reactions, started data taking during May 1999. Up to now no results have been published but evidence of the solar neutrino detection has been presented at Neutrino 2000 Conference.

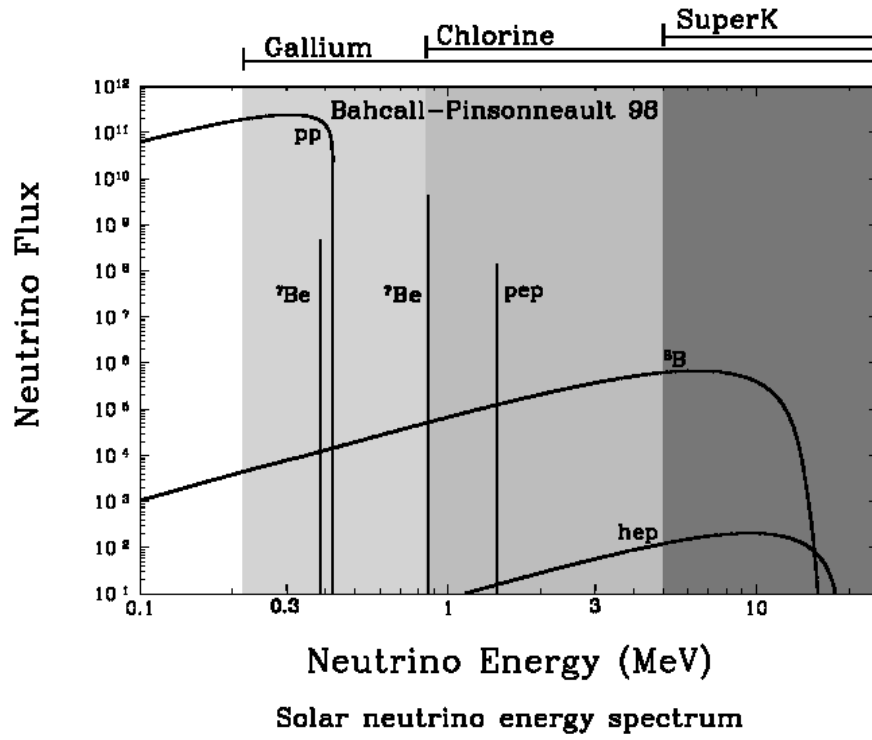


Figure 1.1: Solar neutrinos energy spectra predicted from the Solar Standard Model. The neutrino flux is in $cm^{-2}s^{-1}$.

Table 1.3: Results of solar neutrino experiments (1 SNU (Solar Neutrino Unit)= 10^{-36} captures per atom per second). Homestake, Gallex and Sage are radiochemical experiments and Kamiokande as SuperKamiokande are real time Čerenkov detectors.

Experiment	Observed Rate	Expected Rate
Homestake $^{37}\text{Cl}(\nu_e, e^-)^{37}\text{Ar}$ $E_{th} = 0.81\text{MeV}$	$2.56 \pm 0.16 \pm 0.16$ SNU [10]	7.7 ± 1.2 SNU
Gallex $^{71}\text{Ga}(\nu_e, e^-)^{71}\text{Ge}$ $E_{th} = 0.23\text{MeV}$	$77.5 \pm 6.2^{+4.3}_{-4.7}$ SNU [11]	129 ± 8 SNU
Sage $^{71}\text{Ga}(\nu_e, e^-)^{71}\text{Ge}$ $E_{th} = 0.23\text{MeV}$	$67.2^{+7.2+3.5}_{-7.0-3.0}$ SNU [12]	129 ± 8 SNU
Kamiokande $e^-(\nu_x, \nu_x)e^-$ $E_{th} = 7.0\text{MeV}$	$(2.80 \pm 0.19 \pm 0.33) \cdot 10^6 \text{cm}^{-2} \text{s}^{-1}$ [13]	$(5.15 \pm 1) \cdot 10^6 \text{cm}^{-2} \text{s}^{-1}$
SuperKamiokande $e^-(\nu_x, \nu_x)e^-$ $E_{th} = 5.5\text{MeV}$	$(2.436^{+0.053+0.085}_{-0.047-0.071}) \cdot 10^6 \text{cm}^{-2} \text{s}^{-1}$ [14]	$(5.15 \pm 1) \cdot 10^6 \text{cm}^{-2} \text{s}^{-1}$

In Fig. 1.2 are reported the comparisons between solar neutrino experiments results and SSM predictions. All measured solar neutrino fluxes are lower than the predictions of the SSM. The discrepancy between the predicted and the measured rates is beyond the uncertainties. This difference is known as *First Solar Neutrino Problem*. It is possible to show in a model independent way that the results of different solar neutrino experiments are not compatible if we assume no neutrino mixing.

The so called *Second Neutrino Problem* corresponds to the fact that the ^8B rate observed by the Čerenkov detectors exceeds the total measured rate in the Chlorine experiment leaving no space for any ^7Be neutrino contribution. A *Third Neutrino Problem* emerges from the Gallium detector results: the measured rate is all accounted for by the pp neutrinos and, again, there is no room for ^7Be neutrinos. This is also known as '*the problem of the missing ^7Be neutrino*'. The large suppression of

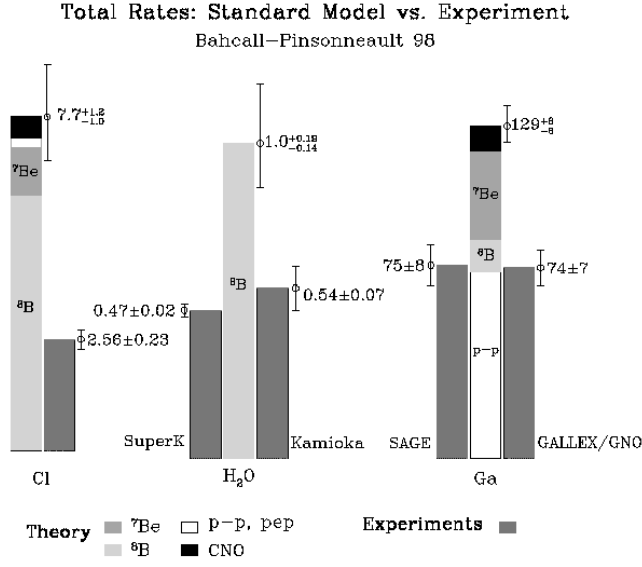


Figure 1.2: Comparison from solar neutrino results and theoretical prediction. The discrepancy observed is beyond the uncertainties [18].

the ^7Be neutrinos together with the observation of ^8B neutrinos is the problem for any solar model. The ^8B nuclei are produced in the reaction $p + ^7\text{Be} \rightarrow ^8\text{B} + \gamma$ and in order to observe neutrinos from ^8B decay enough ^7Be nuclei must exist in the sun's core.

Neutrino oscillation can explain the solar neutrino puzzle. Different solutions are possible. The best-fit global oscillation parameters are reported in Tab. 1.4. No significant deformation of the spectral shape of the ^8B spectrum was observed from the high statistic Super-Kamiokande data. For the day/night asymmetry the following value was obtained again from Super-Kamiokande [19]:

$$2 \left(\frac{N - D}{N + D} \right) = 0.034 \pm 0.022_{stat} \pm 0.013_{sys} \quad (1.22)$$

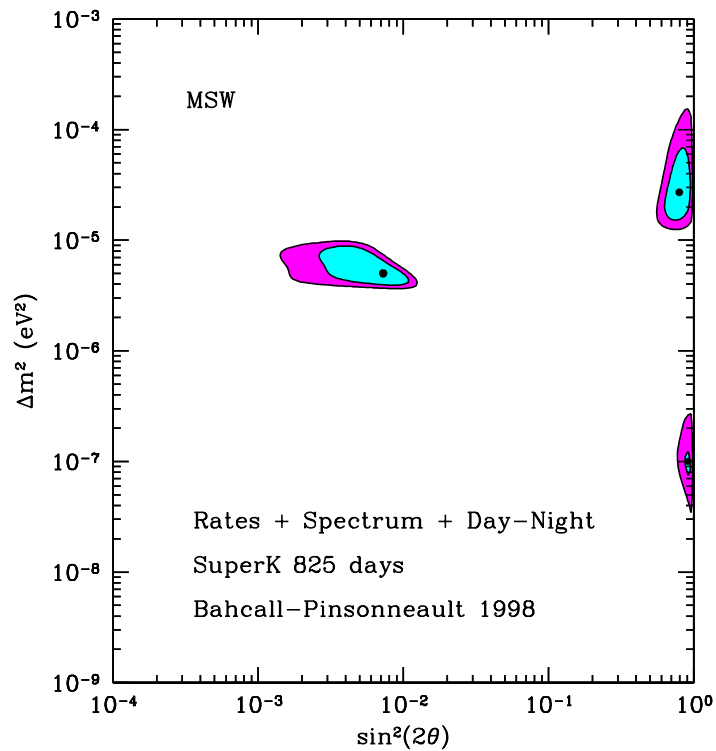


Figure 1.3: Global solution for the allowed MSW oscillation regions [18]. The input data include the total rates in the Homestake, Sage, Gallex and SuperKamiokande experiments, as well as the electron recoil energy spectrum and the day-night effect measured by SuperKamiokande in 825 days of data taking. The contours correspond to the 90% and 99% C.L. relative to each of the best-fit solutions.

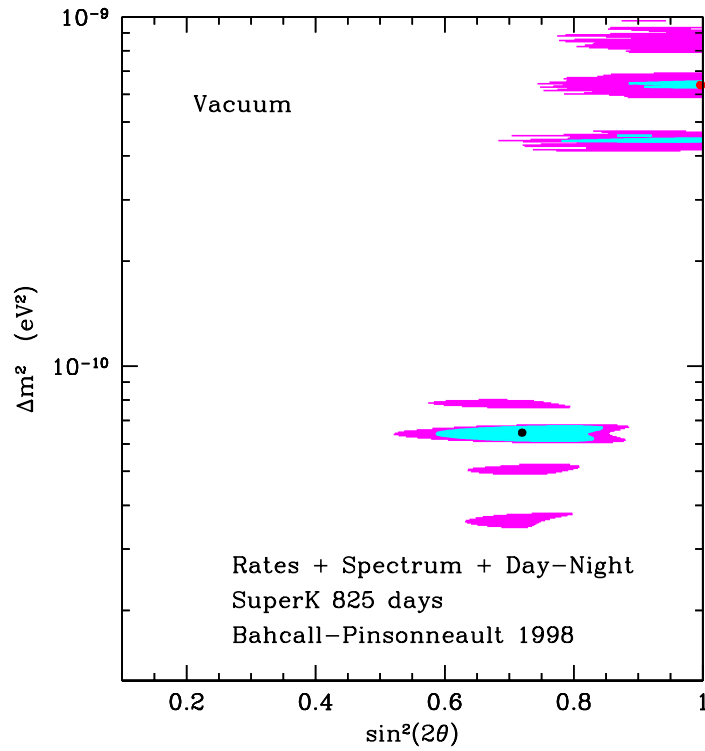


Figure 1.4: Global solution for the allowed vacuum oscillation regions [18]. The input data include the total rates in the Homestake, Sage, Gallex and SuperKamiokande experiments, as well as the electron recoil energy spectrum and the day-night effect measured by SuperKamiokande in 825 days of data taking. The contours correspond to the 90% and 99% C.L. relative to each of the best-fit solutions.

Scenario	$\Delta m^2 (eV^2)$	$\sin^2 2\theta$	C.L.
LMA	$2.7 \cdot 10^{-5}$	$7.9 \cdot 10^{-1}$	68%
SMA	$5.0 \cdot 10^{-6}$	$7.2 \cdot 10^{-3}$	64%
LOW	$1.0 \cdot 10^{-7}$	$9.1 \cdot 10^{-1}$	83%
VAC_S	$6.5 \cdot 10^{-11}$	$7.2 \cdot 10^{-1}$	90%
VAC_L	$4.4 \cdot 10^{-10}$	$9.0 \cdot 10^{-1}$	95%
Sterile	$4.0 \cdot 10^{-6}$	$6.6 \cdot 10^{-3}$	73%

Table 1.4: Best-fit global oscillation parameters for the currently allowed neutrino oscillation solutions [18].

Bibliography

- [1] S.M. Bilenky and B. Pontecorvo, Phys. Rep. 41, 4 (1978) 225-261.
- [2] S.M. Bilenky, hep-ph/0001311.
- [3] B. Pontecorvo, Sov. Phys. JETP 26, 984 (1968).
- [4] Z. Maki, M. Nakagawa, and S. Sakata, Prog. Theor. Phys. 28, 870 (1962).
- [5] J.N. Bahcall, *Neutrino Astrophysics*, Cambridge University Press, 1989.
- [6] Super-Kamiokande Coll., Phys. Rev. Lett. 81 (1998) 1562.
- [7] L. Wolfenstein, Phys. Rev. D 17, 2369 (1978).
- [8] S. Mikeyev and A. Smirnov, Yad. Fiz. 42, 1441 (1985).
- [9] J. N. Bahcall, S. Basu, M.H. Pinsonneault, Phys. Lett. B433, 1-8 (1998).
- [10] B.T. Cleveland et al., Ap. J. 496, 505 (1998).
- [11] W. Hampel et al., Phys. Lett. B447, 127 (1999).
- [12] J.N. Abdurashitov et al., Phys. Rev. C60, 0055801 (1999).
- [13] Y. Fukuda et al., Phys. Rev. Lett. 77, 1683 (1996).
- [14] Y. Fukuda et al., Phys. Rev. Lett. 82, 1810 (1999).
- [15] A. S. Brun, S. Turck-Chiese, P. Morel, AP, J, 506, 913 (1998).
- [16] The SNO Coll., NIM A, 449, 172-207 (2000).
- [17] T. A. Kirsten, Rev. Mod. Phys, Vol. 71, No. 4 (1999).
- [18] J.N. Bahcall, P.I. Krastev, A. Y. Smirnov, Phys. Rev. D, 58, 58-96 (1998).

- [19] Y. Suzuki, for the Super-Kamiokande Coll., in *Neutrino 2000*.

Borexino: Physics Goals and Detector Design

Borexino experiment is devoted to the real time detection of low energy ($\leq 1\text{MeV}$) solar neutrinos. This energy region is more sensitive to neutrino oscillations and in particular, the monochromatic ${}^7\text{Be}$ line (0.862MeV , 90%) is an excellent probe in order to test the various oscillation parameter regions. No direct measurement of ${}^7\text{Be}$ neutrinos has been performed yet.

An international team composed by Italian, German, American, Russian, Hungarian and French physicists is collaborating for the realization of this challenging project. Technical developments were realized in order to reach and detect unique low levels of radioactive contaminations. Cosmic ray induced radioactivity is reduced locating the experiment underground and via hardware veto. Natural radioactive elements like uranium, thorium and their daughter nuclei, radon and krypton gases, ${}^{14}\text{C}$ and potassium, etc. decay with an energy release in the region of interest. Only via a strict selection and purification of materials used, the solar neutrino signal can be disentangled from the background.

The detector is now close to completion of construction in the underground laboratories of Gran Sasso (LNGS), Italy.

2.1 Physics Goals

Solar neutrino detection in Borexino is based on the well known technique of liquid scintillator spectroscopy. The non standard aspect consist in the use of an unsegmented volume composed by 300 tons of ultra-pure liquid scintillator surrounded by 1000 tons of passive buffer. About 2200 photomultipliers detect the scintillation

light.

The detection reaction is neutrino elastic scattering off the electrons contained in the scintillator ($\nu + e^- \rightarrow \nu + e^-$). The reaction cross section is well defined in the frame of electroweak theory [7].

I discuss here the basic considerations about the neutrino signal expected in Borexino in standard and non standard scenarios and the main sources of background.

2.1.1 Neutrino Signal

Borexino main goal is to detect ${}^7\text{Be}$ mono-energetic solar neutrinos (0.862 MeV, 90%) via elastic scattering off electrons. The electron Compton edge will be at 0.66 MeV and represent the basic signature for the reaction (photon emission in the scintillator is isotropic so the directionality of the reaction is lost). The scattering reaction is neutrino flavour insensitive so charged and neutral currents contribute to the amplitude of the basic reaction. The cross section is $\sim 10^{-44}\text{cm}^2$ for 0.5 MeV electron neutrinos and it is 4.5 times lower for the other neutrino flavours.

The signal of recoil electrons scattered by ${}^7\text{Be}$ solar neutrinos occurs in the energy window 0-0.66 MeV at a rate of $\sim 0.5/\text{day}/\text{ton}$ of target material in a standard scenarios where neutrino does not oscillate. A $\pm 3.5\%$ time variation of the signal during the year is expected from the variation of solid angle in the Earth orbit. Even if the effect is very little it can be used in principle as a further solar neutrino signature.

The solutions to the Solar Neutrino Problem in terms of neutrino oscillation would provide a substantial reduction of the flux measured by Borexino due to flavour conversion. As described in Chap.1 the possible solutions are:

- *MSW Effect*: in the case of small mixing angle MSW solution (SMA) ${}^7\text{Be}$ electron neutrinos are almost completely converted. The interaction rate is dominated by $\nu_{\mu,\tau}$. It correspond to 0.2·SSM. For the large mixing angle MSW solution (LMA) solution the conversion is incomplete, hence resulting in a signal of 0.5·SSM. Moreover, Borexino can be considered unique in the possible observation of the so called LOW solution because the difference from the flux observed during day and during night is maximized in the energy region of ${}^7\text{Be}$. The survival probability for solar neutrinos in the different scenarios is reported in Fig. 2.1. The energy spectra predicted for the no oscillation scenario and for MSW effect is in Fig. 2.2.

- *Vacuum Oscillation*: in this scenario the annual variation of the signal is enhanced

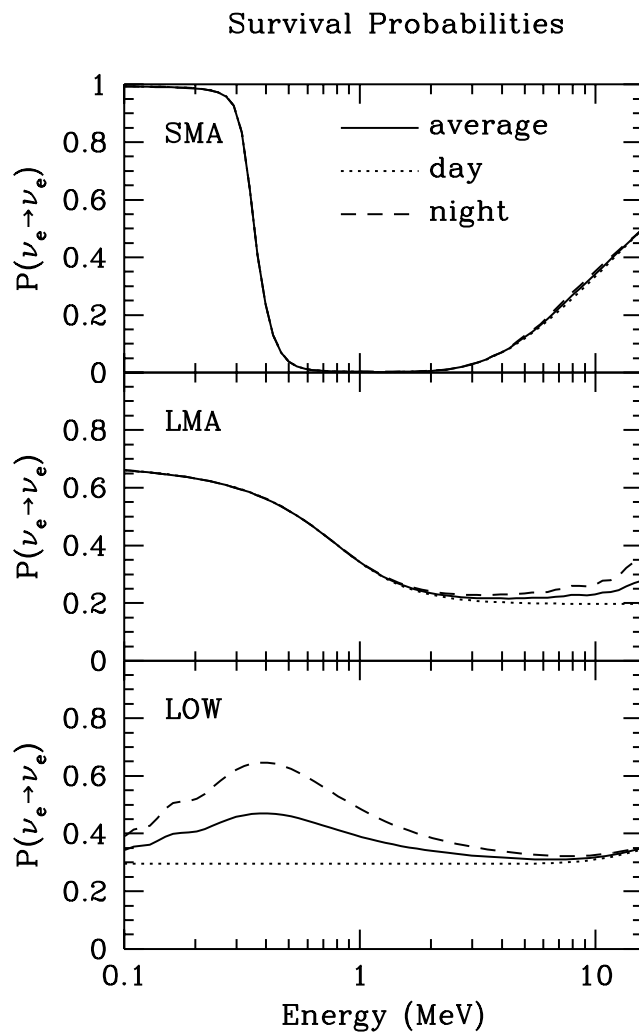


Figure 2.1: Survival probabilities of solar neutrino arriving on the earth. The full line is the average probability over one year, the dotted line is the one year day-time average and the dashed line the night-time average. Regeneration in the earth is included [8]. In the energy region 0.1-1 MeV the three effects are present.

Neutrino Source	SSM	LMA	SMA	LOW
pp	1.3	1.0	0.6	0.6
${}^7\text{Be}$	45.7	26.0	9.7	25.1
pep	2.0	1.0	0.4	1.0
${}^{13}\text{N}$	4.2	2.3	0.9	2.3
${}^{15}\text{O}$	5.5	2.8	1.1	2.8
${}^{17}\text{F}$	0.07	0.03	0.01	0.03
${}^8\text{B}$	0.01	0.04	0.05	0.05

Table 2.1: Neutrino signal expected in Borexino in counts per day in the energy window $0.25 - 0.8$ MeV for the scattered electron. The BP98 Solar Standard Model (SSM) is considered and the oscillation scenarios large mixing angle MSW solution (LMA), small mixing angle MSW solution (SMA) and LOW are analyzed.

in the region of ${}^7\text{Be}$ ($\sim 25\%$). The comparison among the energy spectra predicted for the no oscillation scenario, for MSW effect and vacuum oscillation solution is shown in Fig. 2.2.

Without an event by event signature for neutrino events, it is mandatory to have a low background counting rate which is lower than the neutrino signal. The foundation of a “new technology” was requested in order to detect these rare low energy events in real time [10].

The background sources have been classified into three different classes: internal, external and surface background.

2.1.2 Internal Background

Intrinsic background contained in the liquid scintillator is classified as *Internal Background (IB)*. The most important internal sources of background for Borexino which were studied in CTF-1 and CTF-2 are:

- ${}^{14}\text{C}$: the β particles ($Q=156$ keV) emitted by ${}^{14}\text{C}$ decay set the low energy threshold of the experiment at ~ 250 keV. The origin in liquid scintillators of this radioactive nuclei is discussed in Chap. 3 and in [1].

I summarize here some considerations about the ${}^{14}\text{C}$ level tolerable in Borexino. The goal is to set an upper level for the ${}^{14}\text{C}/{}^{12}\text{C}$ ratio which would be acceptable for Borexino internal liquid scintillator. The CTF-2 will be used

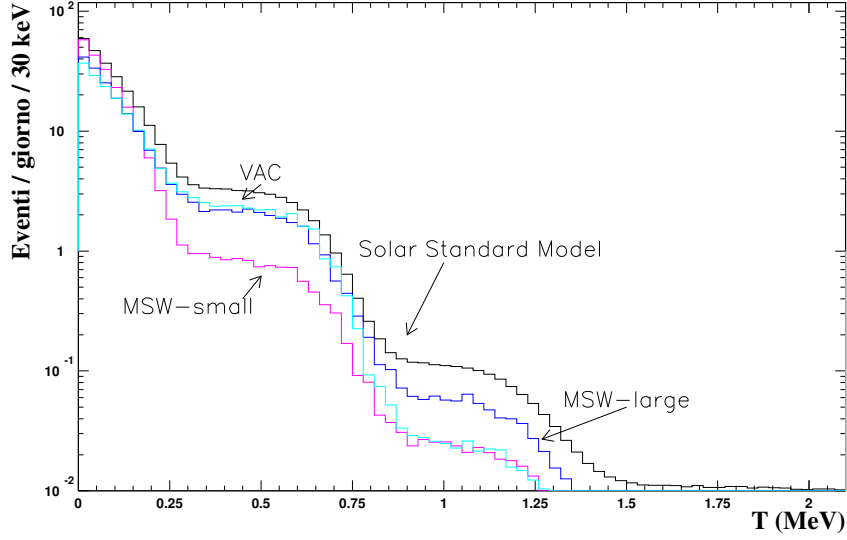


Figure 2.2: Energy spectrum of neutrino signal predicted in Borexino in different standard and non standard scenarios.

during the scintillator procurement to measure ^{14}C level. In the case that the ^{14}C contamination exceeds the derived upper limit, the scintillator solvent will be rejected. The Geneb, Traking and Spatial Reconstruction Codes from Milan [11] have been used to simulate ^{14}C events in Borexino.

I will consider as "tolerable" a level of ^{14}C that is going to produce less than 1 ± 1 event/day in 300 tons of liquid scintillator in the Neutrino Window (250-800 keV). In order to evaluate the small fraction of events which fall into this window we need a high statistic simulation. A ratio of $^{14}\text{C}/^{12}\text{C} = 10^{-18}$ in 300 tons of PC (C_9H_{12}) corresponds to $52\text{Bq} \sim 4.5 \cdot 10^6/\text{day}$. The number of events to be simulated in order not to be limited by simulation should be a factor of 10 greater than the number of counts per day expected. On the other hand if we set an energy threshold on the ^{14}C spectra at 100 keV, we need only ~ 0.1 of the entire statistics. The evaluation presented here is based on $4 \cdot 10^6$ events of ^{14}C with energy greater than 100 keV.

If we consider a photo-electron yield of ~ 380 pe/MeV, the Neutrino Window (NW) lower energy threshold corresponds to 95 pe. The number of events per day in 300 tons of PC for a level of $^{14}\text{C}/^{12}\text{C} = 10^{-18}$ is 0.2.

With a contamination of $^{14}\text{C}/^{12}\text{C} = 10^{-18}$ the number of events mimicking the neutrino signal is still tolerable.

Now I study the probability to find in the NW events produced by a pile-up of two ^{14}C events. I define a "*pile-up event*" a coincidence event composed by two ^{14}C decays reconstructed in the fiducial volume (FV). The two events must appear in a coincidence time window (τ) where it is going to be very difficult to separate in an off-line discrimination. I consider $\tau = 100$ nsec as a possible time window where two ^{14}C events might not be disentangled.

From the energy spectra simulated via MonteCarlo I extrapolated the percentage of events that can be found in the NW. The time distribution can be a possible tool to be used in order to disentangle these events from the neutrino one. The probability of a pile-up event is:

$$P = r^2 \cdot \tau \quad (2.1)$$

where r is the ^{14}C count rate and the coincidence time is $\tau = 100$ nsec. The results are summarized in Tab. 2.2. The pile-up energy spectrum is shown in Fig. 2.4. A fraction of $\sim 0.4\%$ of the pile-up events enter the NW. On the base of these results we can set a safety limit at $^{14}\text{C}/^{12}\text{C} = 3 \cdot 10^{-18}$.

$^{14}\text{C}/^{12}\text{C}$	r (ev/s)	τ (nsec)	P_p (ev/d)	P_p (N.W.) (ev/d)
10^{-18}	52	100	23.36	0.09
$2 \cdot 10^{-18}$	104	100	93.45	0.37
$4 \cdot 10^{-18}$	208	100	373.80	1.50
$6 \cdot 10^{-18}$	312	100	841.05	3.36
$8 \cdot 10^{-18}$	416	100	1495.20	5.98
10^{-17}	520	100	2336.26	9.35

Table 2.2: Pile-up event rate with different ^{14}C abundances.

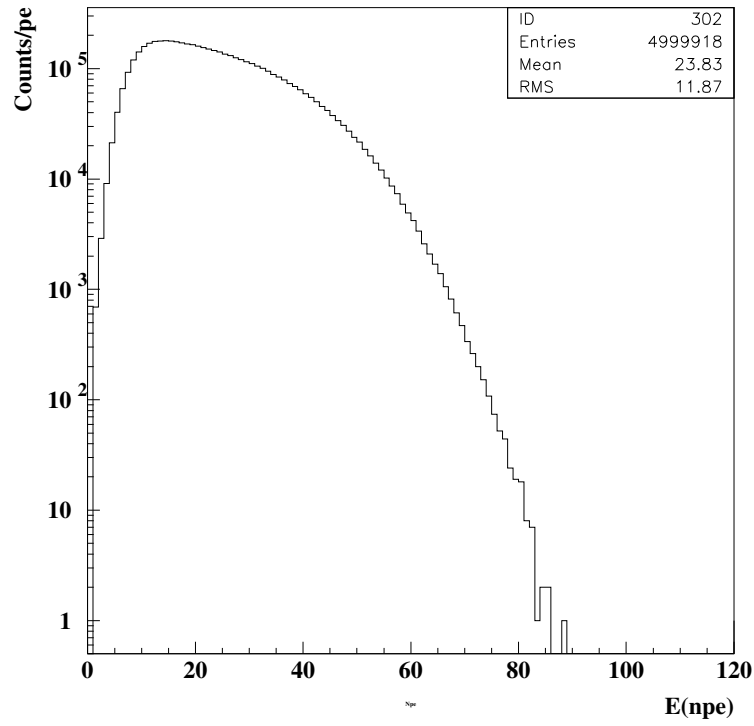


Figure 2.3: ^{14}C beta spectrum without pile-up. 5 million events have been simulated. The energy scale is number of photoelectron (npe). 380 pe/Mev is the photon yield taken into account.

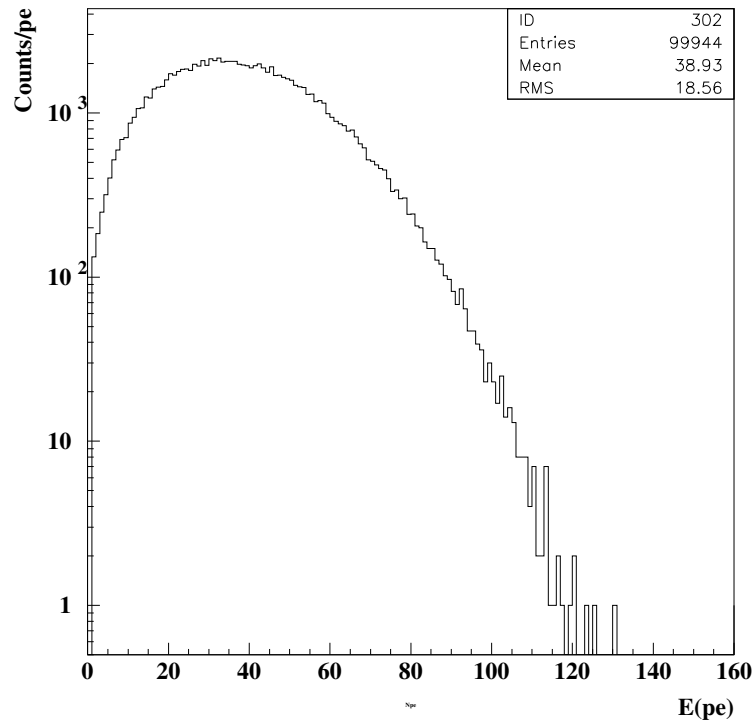


Figure 2.4: Energy spectrum of ^{14}C pile-up events. The energy scale is in number of photoelectrons (pe). The lower energy threshold of the NW is at 96 pe.

- ^{238}U , ^{232}Th and ^{40}K : Borexino can tolerate level of U and Th not greater than 10^{-16} g/g . This level was detected in PC for the first time in CTF-1 demonstrating the conceptual feasibility of the experiment. Secular equilibrium for the U and Th chains is assumed. If we consider a level of 10^{-16} g/g for U and Th and 10^{-14} g/g for K_{nat} , we found in the NW $\sim 26\ \beta + \gamma$ events/day in the 100-ton fiducial volume (FV) and $\sim 122\ \alpha$ events/day in the FV. Off-line it is possible to identify some of these events. The discrimination methods used are more deeply described in Chap. 4 in the context of CTF-2. One technique applied is based on delay coincidences identification (DC). An identification efficiency of 95% will reduce these numbers to $\sim 25\ \beta + \gamma$ events/day in the FV and $\sim 118\ \alpha$ events/day in the FV. A second method used to reject part of the background is based on pulse shape discrimination analyze (PSD) because the pulse shape produced by an α event in liquid scintillator is different from the one due to a β event. Assuming an identification efficiency of 90% the background becomes $\sim 25\ \beta + \gamma$ events/day in the FV and $\sim 34\ \alpha$ events/day in the FV. After tagging of delayed coincidence events one knows also the activity of the parent isotopes. It is possible to apply a statistical subtraction (SS) of these isotopes. If we assume a 95% efficiency we have $\sim 13\ \beta + \gamma$ events/day and $\sim 19\ \alpha$ events/day in the FV.
- ^{222}Rn , ^{85}Kr : radon is a noble gas produced in the ^{238}U chain. It is chemically inert and has a great capacity of diffusion in air and through matter (diffusion coefficient in air = $0.1\text{ cm}^2/\text{s}$). Radon contamination can come from a direct contact with air or through emanation of environmental materials. In order to reduce possible contaminations a strict selection of materials involved was realized via a new radon emanation measurement technique developed by the Heidelberg group [14].
A significant contact with air can introduce also ^{85}Kr as observed in CTF-1.
- ^7Be : Various muon reactions can induce radioactive elements [15]. The absence of isotopes heavier than $^{12,13}\text{C}$ in the liquid scintillator limits the cosmogenic radioactivity problem. The possible long lived radioactivities from a carbon target that cannot be vetoed by the muon signal are: ^{11}B , ^{11}C , ^{10}C and ^7Be . The only dangerous element for Borexino is ^7Be . The effective rate of *in-situ* production is $\sim 0.4/\text{day}/100\text{ton}$ in equilibrium [5].

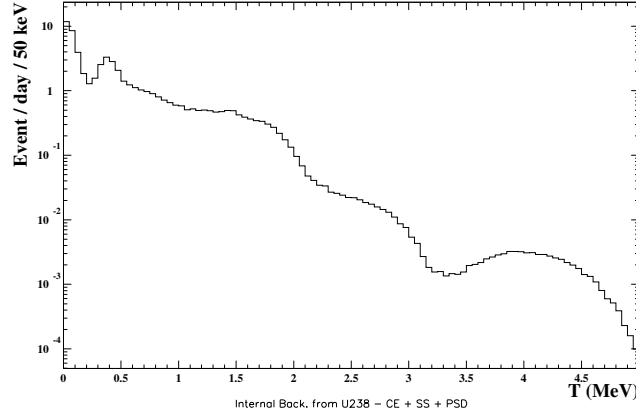


Figure 2.5: Energy spectra in logarithmic scale of internal background predicted in Borexino with DC, PSD and statistical cut applied.

2.1.3 External Background

γ -rays emitted outside the IV create what we call *External Background (EB)*. The suppression of this flux plays a major role in the practical construction of the detector. Principal sources are: photomultipliers, rock walls of the experimental hall, environmental materials that compose the detector. A systematic measurement and selection of the materials were realized in order to reduce this contamination. Some of the fundamental contributions to the EB and the number of γ events entering the NW are reported in Tab. 2.3.

The radial distribution of these events can allow an off-line identification and an efficient subtraction. The fiducial volume will be optimized depending on the external activity observed. The energy spectrum of external background predicted is in Fig. 2.6.

2.1.4 Surface Background

Possible contaminants coming from the IV materials are classified as *Surface Background (SB)*. The nylon material that composes the IV should meet the most stringent requirements of cleanliness since it is the only material in direct contact with the liquid scintillator. Radon exposure during production and installation should be kept under a strict control in order to avoid build-up of Radon daughters. Different

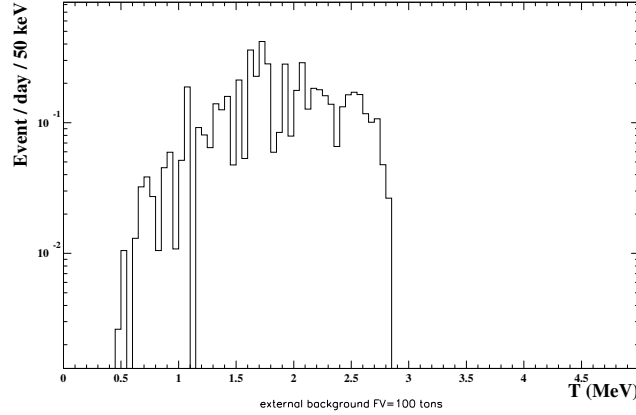


Figure 2.6: Energy spectrum in logarithmic scale of external background predicted in Borexino.

materials are under measurements [9].

A ^{40}K contamination was detected in CTF-2 coming from a part of the IV system (strings). A section in Chap. 5 summarizes the results.

The comparison between the external and internal background and the neutrino signal is reported in Fig. 2.7.

2.2 Borexino Detector

Borexino is being constructed in hall C of the Gran Sasso Laboratories (LNGS). The Laboratories are located beside the Gran Sasso tunnel (10.4 km long) on the highway connecting Teramo to Rome, at about 6 km from the west entrance. They consist of three experimental halls, named hall A, B and C, and a series of connecting tunnels and service areas. The three experimental halls are ~ 70 m long and about 18 m high and large. The laboratory is located at 963 m over the sea level and the maximum thickness of the rock overburden is 1400 m, corresponding to 3800 m.w.e. The residual muon flux underground is $\sim 25/d/m^2$. The radioactive elements in the rock of the hall produce a γ - ray flux of $\sim 10^8/d/m^2$.

Component	^{238}U (g/g)	^{232}Th (g/g)	^{nat}K (g/g)	Total Mass (g)	Rate in NW (ev/day/100ton)
2000 PMTs	$3 \cdot 10^{-8}$	$1 \cdot 10^{-8}$	$2 \cdot 10^{-5}$	$38 \cdot 10^6$	0.06
PC Buffer	$1 \cdot 10^{-15}$	$1 \cdot 10^{-15}$	$5 \cdot 10^{-12}$	$8.7 \cdot 10^8$	≤ 0.004
Nylon Bag	$2 \cdot 10^{-11}$	$2 \cdot 10^{-11}$	$1 \cdot 10^{-8}$	$5 \cdot 10^4$	≤ 0.04
Light guides	$2 \cdot 10^{-10}$	$1 \cdot 10^{-9}$	$3 \cdot 10^{-7}$	$6 \cdot 10^6$	0.01
SSS	$2 \cdot 10^{-10}$	$1 \cdot 10^{-9}$	$3 \cdot 10^{-7}$	$3.7 \cdot 10^7$	≤ 0.007
Cables	$2.1 \cdot 10^{-8}$	$2.4 \cdot 10^{-8}$	$7 \cdot 10^{-6}$	$2 \cdot 10^5$	≤ 0.003
Rock					≤ 0.005
^{222}Rn in the PC					0.03
Buffer (1mBq/m^3)					
Total					0.11 ± 0.05

Table 2.3: Expeted external background in the fiducial volume coming from the different sources (SSS is Stainless Steel Sphere).

2.2.1 Internal Structure

The detector is designed in order to reduce γ – ray background in the core via a graded shielding. This approach is realized through different layers of increasingly radio-pure materials. Starting from inside we find the following parts:

- *Liquid scintillator*: The mixture selected is composed by pseudocumene (PC, 1,2,4-trimethylbenzene, $\text{C}_6\text{H}_3(\text{CH}_3)_3$) as a solvent and by the fluor PPO (2,5-diphenyloxazole, $\text{C}_{15}\text{H}_{11}\text{NO}$) as a solute, at a concentration of 1.5g/l . The studies realized by the collaboration about this scintillator are reported in [2] and the main characteristics are summarized in Tab. 2.4.

- *Inner Vessel and Radon Barrier*: The design is sketched in Fig. 2.8. It is made by $125\ \mu\text{m}$ thick transparent nylon. It is tethered by a system of strings whose tension can be monitored to control the buoyancy and mechanical stability. A second nylon vessel is installed in order to reduce radon and other impurities diffusing into the vicinity of the IV.

- *Buffer Liquid*: In order to reduce practically the buoyancy force on the IV to zero a buffer liquid composed by pure PC was selected. The total mass needed is ~ 1040 tons. A light quenching compound DMP (dimethylphthalate) [3] is added with a concentration of 5g/l in order to reduce the light produced from γ – rays coming

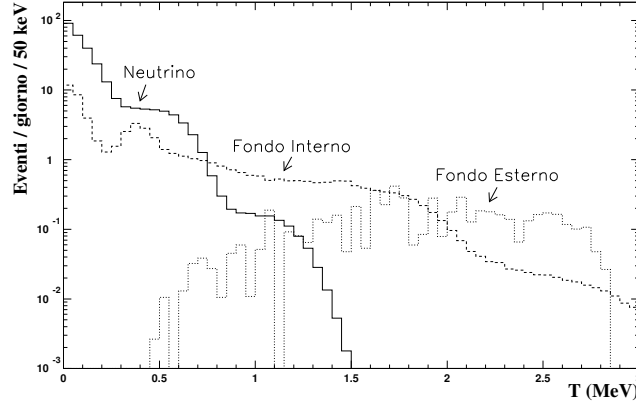


Figure 2.7: Comparison from the two main sources of background and neutrino signal expected in Borexino.

from the external background in the buffer. The light mean free path lengths and Čerenkov light emission yield, important for the muon veto, are not affected by the presence of DMP.

- *Stainless Steel Sphere (SSS)*: A 13.7 m diameter, 8-10 mm thick stainless steel sphere (SSS) contains the scintillator and it is used as support structure of the PMTs. It is sustained by 20 legs which are welded on the base plate of the water tank. The sphere divide hermetically the 2m external shield layer of ultrapure water from the inner scintillator.

- *PMTs and Light Concentrators*: ETL 20 cm are the PMTs selected for Borexino and CTF. In the frame of CTF-2 discussion I illustrate the main characteristics of them. They are installed inside the sphere and connected by feed-through across the sphere wall to a single cable outside the sphere. The back-end sealing has been designed to be compatible for operation in PC and in water. 1800 PMTs are equipped with light concentrators to enhance the geometrical coverage ($\sim 30\%$). The other 400 are dedicated to the internal muon veto system.

The outer part of the detector concern the following items:

- *Outer Muon Veto*: Other 210 PMTs are going to be mounted outside the sphere and work as outer muon veto detector. A complete encapsulated sealing design was developed for the outer muon veto PMTs. The overall muon veto system has

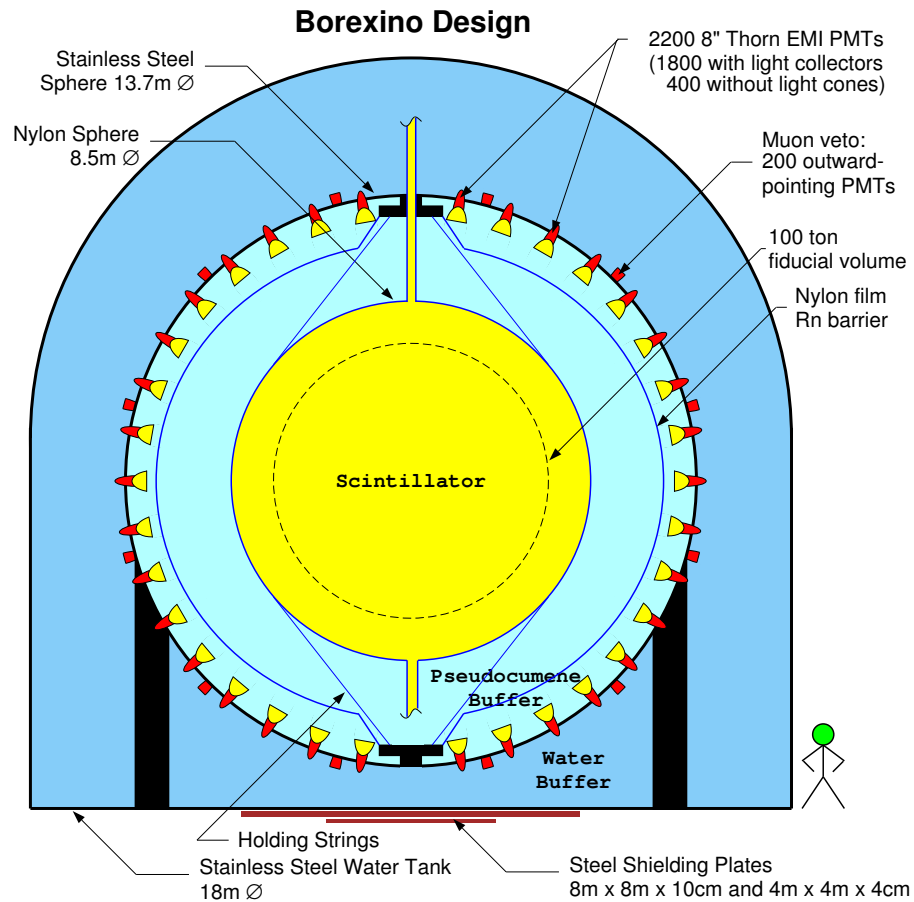


Figure 2.8: Sketch of the Borexino detector.

General Characteristics	
Total Mass	~ 290 tons (8.5 m diameter IV)
FV Total Mass	100 tons (6 m diameter software cut)
Density	0.88 g/cm^3
Optical Characteristics	
Primary Light Yield	$\sim 10^4$ photons/MeV (@380 nm)
Peak Emission wavelength	365 nm
Attenuation length	$\geq 5m$ (@430 nm)
Decay lifetime without abs/reem	~ 3.5 nsec (β particles)
Decay lifetime with abs/reem	~ 5 nsec (β particles)
α/β discrim. capability.	99.7 % α identif. with 98% β identif. (measured on ≤ 1 l samples)
α/β discrim. capability	90 % (measured in CTF = 5 m^3 samples)
Physical Characteristics	
α -quenching (E)	$Q(E) = 20.3 - 1.3E(\text{MeV})$
Radioactive Characteristics	
^{238}U	$(3.5 \pm 1.3) \cdot 10^{-16} \text{ g/g}$
^{232}Th	$(4.4 \pm 1.5) \cdot 10^{-16} \text{ g/g}$
$^{14}\text{C}/^{12}\text{C}$	$(1.94 \pm 0.09) \cdot 10^{-18}$

Table 2.4: Borexino liquid scintillator (Pseudocumene) principal characteristics as measured.

been designed in order to establish a muon veto identification which suppresses this background by a factor 10^4 .

- *Water Buffer and Water Tank:* Overall containment of the detector is provided by a domed cylinder external tank 18 m in diameter and 17 m high. Deionized water provides at least a 2 m shielding against external gamma and neutron radiation. Čerenkov light produced in the water provides then the possibility to veto muon events. In order to increase the cosmic ray detection efficiency, the water tank internal wall is covered by *Tyvek* sheets which reflect the Čerenkov light irradiated by cosmic rays crossing water.

2.2.2 Auxiliary Systems

Auxiliary systems maintain the detector operative and allow manipulation of the different liquids.

- *Water Purification Plant:* ~ 2000 tons of ultrapure water are used as a shield against external background and as a highly transparent Čerenkov medium; ~ 1000 tons for CTF shield, different tons for cleaning the detector and the auxiliary system are used. The production system ($2 \text{ m}^3/\text{h}$) is mainly composed by the CTF water plan. The reader is referred to Chap. 4 for a comprehensive description of the water system.

- *Scintillator Storage, Purification and Handling:* A plan is under construction in hall C in order to store 300 tons of liquid scintillator in 4 storage tanks and handles and purifies all the amount of scintillator needed for Borexino. The system consists of electropolished stainless steel plumbing and radon tight valves and fittings. On-line purification is based on four systems: gas removal, water extraction, distillation and solid column chromatography. All these systems are going to be tested and improved using CTF-2 as the interconnection system.

- *Nitrogen Distribution System:* Pure and ultra-pure nitrogen is used for various purposes in Borexino and CTF like stripping column, blanket of the tanks etc. The plan consists of three 6 m^3 storage tanks, two atmospheric evaporators and a water bath electric heater to produce regular nitrogen of up to $250 \text{ m}^3/\text{h}$. High purity nitrogen is produced by charcoal column purification of the liquid nitrogen prior to evaporation. It can supply up to $100 \text{ m}^3/\text{h}$ of nitrogen [13, 14].

- *Signal Processing and Data Acquisition:* The fundamental requirements for the read-out Borexino system are: single photoelectron detection, good time resolution and a wide dynamic range. All these constraints are fulfilled with the following chain [6]: the signal coming from PMTs is AC coupled with a Front-End card which performs noise filtering, pre-amplification, shaping and integration of the input signal. Each Front-End board provides also an analog sum of the 12 linear output signals that are used to extend the whole dynamic range of the system up to 30 MeV by means of Flash ADCs. The output of Front-End cards are sent to VME slave custom card. This board performs the analog to digital conversion of the charge signal, measures the time of the linear signal with 0.4 nsec resolution, computes the sum of recorded hits in a time window of 60 nsec and stores the whole information in a Dual Port RAM that can be read from VME.

The outer muon-veto system is read with a different Front End system that performs

a charge to time conversion of each signal after a linear pre-amplification.

The DAQ system is based on LINUX operating system and the software is custom made.

Bibliography

- [1] E. Resconi, S. Schönert, ^{14}C *Production in Petroleum Reservoirs*, in preparation for publication.
- [2] Borexino Coll., NIM A440 (2000) 360.
- [3] M. Chen et al., NIM A420 (1999) 189.
- [4] M. Deutsch et al., Borexino Coll., “Proposal to NSF” (1996); L. Oberauer and S. Schönert, Proc. of the IVth SFB-375 Ringberg Workshop, “Neutrino Astrophysics” (1997) 33-36; M. Chen et al., Borexino Coll., “Proposal to NSF” (1998).
- [5] T. Hagner et al., Astropart. Phys. (2000), accepted for publication.
- [6] V. Lagomarsino and G. Testera, NIM A 430 (1999) 435.
- [7] G. t’Hooft, Phys. Lett. B37 (1971) 195.
- [8] <http://www.sns.ias.edu/jnb/>.
- [9] Borexino Coll., Phys. Lett. B 422 (1998) 349-358.
- [10] Borexino Coll., The Science and technology of Borexino: a realtime detector for low energy solar neutrinos, to be published.
- [11] B. Caccianiga, S. Bonetti, M. Giammarchi, J. Maneira, *GENEB: Generation of Neutrino and Background*, Borex Report (1997).
- [12] L. Cadonati, *The Borexino Solar Neutrino Experiment and its Scintillator Containment Vessel*, Ph. D. Thesis, Princeton University (January 2001).
- [13] W. Rau, Ph. D. Thesis, Heidelberg University (1999).
- [14] G. Heusser et al., Appl. Rad. Isot. 52 (2000) 691.

Underground Production of ^{14}C in Petroleum

An underground production of ^{14}C in oil wells by neutron induced reactions has been estimated. A general model of petroleum site has been taken into account and the presence of nitrogen in natural gas has been considered the most significant target for the neutrons. The order of magnitude of the reenrichment estimated can explain the anomalous level of ^{14}C found in the liquid scintillators measured by CTF-1 and CTF-2. In living material this ratio is 10^{-12} kept in equilibrium by a continuous production due to the reaction $^{14}\text{N}(n, p)^{14}\text{C}$ produced by cosmic rays in the atmosphere. The hydrocarbon measured has an apparent age of 20 half lives that mean 114600 years. The liquid scintillator measured is synthesised from petroleum and oil wells are mostly found deep underground so shielded from the cosmic ray flux. The typical life time of an oil well is hundreds of million year so a reenrichment of ^{14}C had happen in the liquid scintillator detected.

3.1 Petroleum and Petroleum Sites: Basic Concepts

In order to evaluate the production of ^{14}C in oil wells we need to summarize here some basic concepts about petroleum and petroleum fields.

Petroleum is a complex mixture of hydrocarbons that occurs in the earth in liquid, gaseous, or solid forms. Liquid and gaseous hydrocarbons are so intimately associated in nature that it has become customary to shorten the expression "petroleum

and natural gas” to ”petroleum” when referring to both.

The exact process by which oil and natural gas are produced is not precisely known. Crude oil is thought to form from decomposed organic substance that settles on the bottom of marine basins and is rapidly buried within sequences of mudrock and limestone. Natural gas and oil are generated from such *source rocks* only after heating and compaction. After their formation, oil and natural gas migrate from source rocks to *reservoir rocks* composed of sedimentary rocks largely as a consequence of the lower density of the hydrocarbon fluids and gases. Good reservoir rocks, by implication, must possess high porosity and permeability. A high proportion of open pore spaces enhances the capacity of a reservoir to store the migrating petroleum. The third condition in order to have an oil pool is that a non-permeable seal above the reservoir rock prevents petroleum from escaping (*structural trap*). The fundamental characteristic of a trap is an upward convex form of porous and permeable reservoir rock that is sealed above by a denser, relatively impermeable cap rock (e.g., shale or evaporates). The trap may be of any shapes, sizes, origins and rock compositions. Any rock that is porous and permeable may become a reservoir, but those properties are most commonly found in sedimentary rocks, especially sandstone, limestone and dolomites.

Depending on the amount and type of organic matter, oil generation occurs at depths of about 700 to 5,000 metres. Rocks of Tertiary age (1-60 My) dominate the total production of oil.

Although oil consists basically of compounds of only two elements, carbon and hydrogen, these elements form a large variety of complex molecular structures. Almost all crude oil ranges from 82 to 87 percent carbon by weight and 12 to 15 percent hydrogen.

Our model predicts the *in situ* production of ^{14}C within the rock matrix itself. For our evaluation we need to know the following properties of the matrix rock [2]:

- *porosity* (ϵ): fraction of volume of sediment that contains petroleum expressed in percentage. Porosity varies from 5 to 30%. It will be shown that the porosity influences the ratio $^{14}\text{C}/^{12}\text{C}$ only as the second order effect.
- *grain density, rock matrix density* (ρ_r): $2.0 - 2.6 \text{ g/cm}^3$;
- *oil density* (ρ_{oil}): $0.75 - 0.95 \text{ g/cm}^3$;

- diameter of grain: 10^{-6} - few mm.

3.2 The Role of Nitrogen

The natural gas (n.g.) of a petroleum reservoir consists of the low-boiling-point hydrocarbon gases and may range from minute quantities dissolved in the oil to 100 percent of the petroleum content [2]. In addition to the hydrocarbon gases there are gaseous impurities in varying amounts consisting of hydrogen sulfide, nitrogen, and carbon dioxide; they are called the *inerts*. Natural gas under high pressure contains so much CO_2 and N_2 that are non inflammable. The amount of gas in solution depends on the physical characteristics of both the gas and the oil, and on the pressure and temperature in the reservoir; the possible scenarios are very variable. The volume of the solution depends upon the *formation gas-oil ratio* that corresponds to the number of cubic feet of gas per barrel of oil as found in reservoir. The volume of surface-equivalent gas that will dissolve in a unit volume of reservoir oil increases as the reservoir pressure increases, until the oil is finally saturated with gas and no more gas will dissolve in the oil. The changes between one barrel of petroleum in the reservoir and the same petroleum at the surface are graphically shown in Fig. 3.1, [2].

It is known that the Nitrogen found in n.g. can amount up to 99% by volume. There are two possible sources of this contamination: the high percent of N_2 in air suggests that the N_2 in n.g. represents the N_2 contents of air that have been trapped in the sediments, or a second possible source is suggested by the high N_2 contents in gases rich in helium.

The natural gas in a petroleum reservoir may occur as a free gas (when it occupies the upper part of the reservoir, with oil or water below), or as gas dissolved in oil (when oil and gas are in intimate contact). Pools in which all the gas is dissolved in the oil are called *undersaturated pools* to distinguish them from *saturated pools* in which an excess of gas forms a free-gas cap.

As a reference point we will consider the average composition of n.g. calculated on different samples of oil wells from European, African and American origin. The average composition is: CH_4 81,5%, C_2H_6 3.6 %, N_2 5.2 %, CO_2 4.6%, H_2S 1.4 % [2].

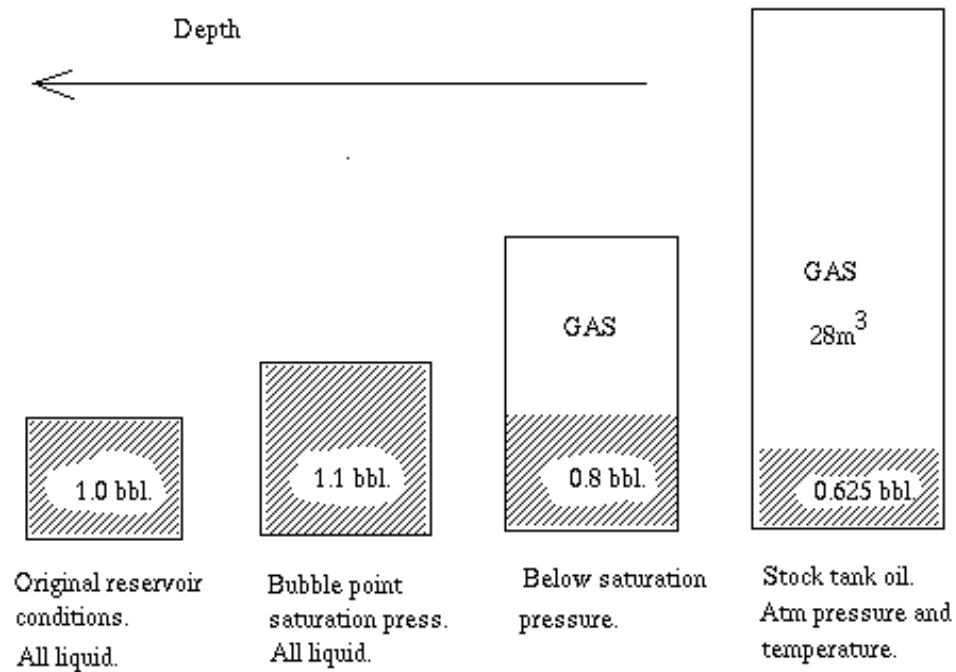


Figure 3.1: Example of volume of one barrel of reservoir oil in which 28 m^3 of gas are dissolved as they pass from the reservoir, where all the gas is in solution, until they reach the stock tank at the surface of the ground.

3.3 Radioactivity of the Petroleum Reservoir

A knowledge of the radioactivity of petroleum has become of some practical importance since the advent of radioactivity well logging. When a potential productive zone is found the first evaluation is usually made using well-logging methods. The logging tool is lowered into the well by a steel cable and is pulled past the formations while response signals are relayed to the surface for observation and recording. These tools often make use of the difference in electrical conductivities of rock, water, and petroleum to detect possible oil or gas accumulations. Other logging tools use differences in radioactivity, neutron absorption, and acoustic wave absorption. We are interested in the radioactive logs analyzes that are based on measurements of gamma rays produced by potassium (^{40}K), by members of Th series and U series usually detected in most cases with a sodium iodide scintillator coupled with a photomultiplier.

From these measurements we have the real values of U and Th abundances in the petroleum reservoir [6].

For our evaluation we consider first the range of U and Th contents in pure Limestone and Sandstone reported in [6]. Presence of highly radioactive minerals (monazite, zircon etc.) may cause substantial increases in Th or U concentrations so it is more significant to consider more realistic cases. We select three examples that we label as Well-1, Well-2 and Well-3 [6]. Well-1 reported in Fig. 3.6 concerns a field of chalk reported in [6] for the difficulties of evaluations of oil zones. Well-2 reported in Fig. 3.7 concerns a shale field with many intervals of the formation. Well-3 reported in Fig. 3.8 is granite wash. In the figure there is more information than in the other examples. In the fourth column we find in black the hydrocarbon contents and we compare it with the second column that reports the U and Th abundance. In order to emphasise the variability of the radioactive contents we report also the value of the oil shales from Colorado and we label it as “extreme case”. In Tab. 3.1 are summarized the values taken into account in our evaluation.

The U and Th content in the oil itself is in most cases negligible. We report here some values of the Uranium content in different oil coming from different pools. Some of the value reported are:

- Oklahoma crude oils: $\text{U} = 2\text{-}10 \text{ ppm}$
- Libyan crude oils: $\text{U} = 1.5 \cdot 10^{-2} \text{ ppm}$
- Arkansas: $\text{U} = 0.5 - 2.5 \cdot 10^{-3} \text{ ppm}$
- Colorado: $\text{U} = 0.17 - 0.7 \cdot 10^{-3} \text{ ppm}$

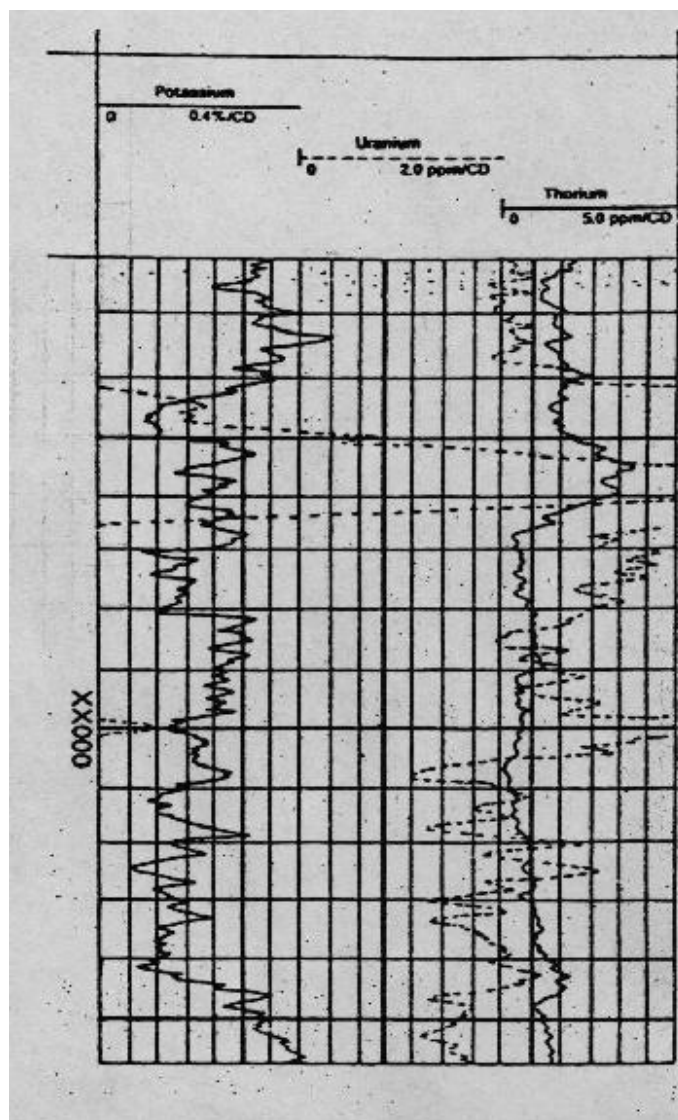


Figure 3.2: Well-1, chalk field [6]. Potassium, uranium and thorium concentrations are reported on the x axis. Each division corresponds to 2.0 ppm for uranium and 5 ppm for thorium. The y axis corresponds to the depth in the earth. It is reported in the figure 20.000 feet depth. Only a small part of the entire well log is reported in the picture. Uranium contents run from 14 ppm to 66 ppm (dashed line), thorium contents from 10 ppm to 30 ppm.

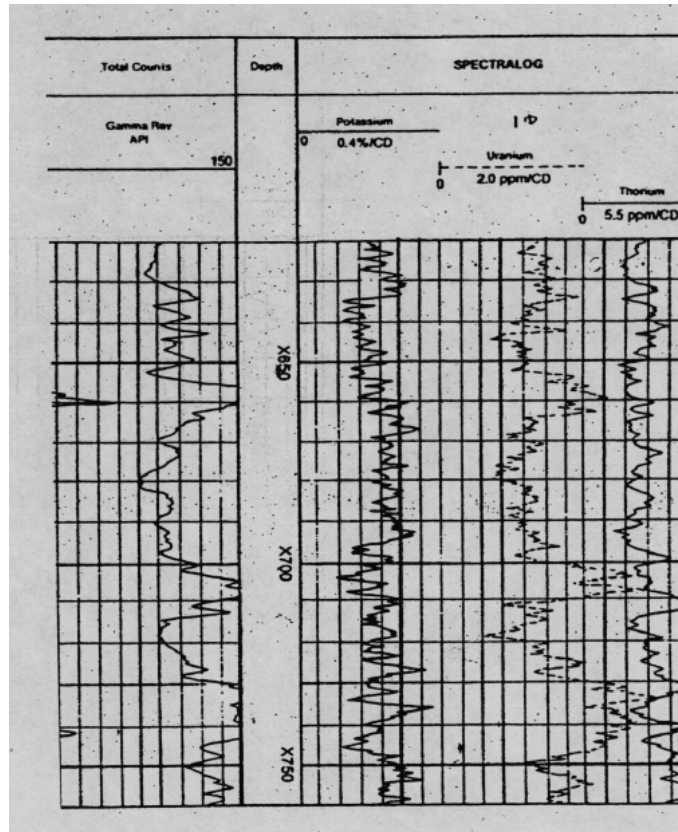


Figure 3.3: Well-2, shale field [6]. Uranium contents run from 6 ppm to 20 ppm (dashed line), thorium contents from 10 ppm to 33 ppm.

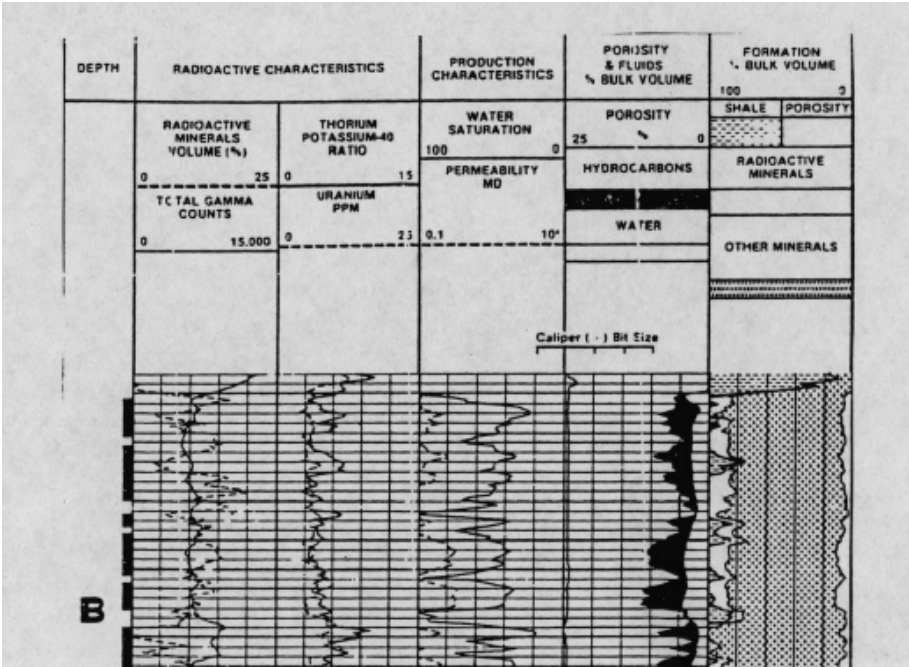


Figure 3.4: Well-3, granite wash well [6]. The hydrocarbon contents are visible in black in the fourth column and the relative U (5-25ppm) and Th (2-15ppm) contents in the rock are in the second column.

- Kansas: $U=0.28 - 2.6 \cdot 10^{-3}$ ppm
- Montana: $U=0.12 \cdot 10^{-3}$ ppm
- New Mexico: $U=0.54 \cdot 10^{-3}$ ppm
- Oklahoma: $U=0.32 - 1.98 \cdot 10^{-3}$ ppm
- Wyoming: $U=0.24 - 13.5 \cdot 10^{-3}$ ppm

3.4 Underground Neutron Flux

The neutron flux encountered in the rock formation can come from different sources: the one originated in the atmosphere by cosmic-ray reactions and penetrating the surface layer down to few meters, those produced underground by cosmic muons down to few hundred meters and those produced through neutron induced and spontaneous fission of uranium and thorium present in the rock and in the oil. Furthermore, neutrons produced by (α, n) reactions on light nuclei are of relevance. Latter production mechanism and neutrons produced by spontaneous fission dominate the flux at typical depths of oil wells.

Alpha particles originated from uranium, thorium and their products are present in the rock. The yield of neutrons per α -particle depends on the (α, n) reaction cross-section. The minimum kinetic energy that α particle must have (lab. system) in order to make the reaction energetically possible is the threshold energy (E_{th}). Neutrons are mainly produced by α particles interacting with light nuclei like ^{27}Al , ^{23}Na , ^{29}Si , ^{30}Si , ^{18}O , ^{17}O , ^{19}F but not on ^{16}O , ^{28}Si , ^{40}Ca (which constitute about 75% of the earth's crust) because of their high E_{th} [5]. Neutrons are produced with an initial energy of several MeV and then slowed down to thermal energies by collisions (thermal neutrons dominate the production for ^{14}C). MonteCarlo simulation shows that $\sim 90\%$ of the original neutron flux is thermalized without absorption.

Heavy elements (U and Th) present in the rock also undergo spontaneous fission. The half-lives for Spontaneous Fission (SF) for the three isotopes are: $t_{1/2}(^{238}\text{U})(SF) = 8.19 \cdot 10^{15}$ y, $t_{1/2}(^{235}\text{U})(SF) = 3.5 \cdot 10^{17}$ y, $t_{1/2}(^{232}\text{Th})(SF) > 1.0 \cdot 10^{21}$ y [10]. Neutrons originating from the spontaneous fission of ^{235}U and ^{232}Th are ignored by us on the basis of their very long fission half-life compared with that of ^{238}U .

The number of neutrons per second (n/s) emitted from 1 kg of natural uranium

Type of rock	U [6] (ppm)	Th [6] (ppm)	n from U [7] (α, n) (n/g/y)	n from Th [7] (α, n) (n/g/y)	n sp. fis. [7] ^{238}U (n/y/g)
Sandstone (pure sandstone)	0.2-0.6	0.7-2.0	0.837	0.38	0.467
Limestone (pure sandstone)	0.1-9.0	0.1-7.0	0.64	0.285	0.467
Shale(av.) (200 samp.)	6	12			0.467
Well-1 (Clay)	14-22	10-30			
Well-2 (Shale)	10-20	16.5-33			
Well-3 (Granite Wash)	2-25	2-15			
Oil Shales from Colorado (Extreme case)	500	1-30			

Table 3.1: U and Th typically found in Sandstone, Limestone and in well samples and the relative neutron production [7].

during spontaneous fission has been estimated by various authors to be in the range from 14.7 to 17.9 n/s/kg [7]. For an uranium concentration in rock of 1 ppm this corresponds to a range between 0.40 and 0.56 n/y/g. In Tab. 3.1 are summarized the ranges of U and Th typically found in Sandstone, Limestone and in a sample of 200 Shales [6] with the relative neutron production [7].

The composition of the reservoir rock and of the oil influences the production of ^{14}C . A fraction of thermal neutrons will be absorbed by elements in the rock or in the oil without producing ^{14}C . The macroscopic cross sections Σ_{rock} and Σ_{oil} quantify these processes. Only a certain percentage of the neutrons produced will interact in the oil producing ^{14}C . The cross section is $\Sigma_{^{14}\text{C}}$.

The total absorption cross section in the rock depends mainly on two groups of elements: Si, O, Al, Fe, Mg, Ca, Na and K which have low absorption cross sections but they are abundant in the rock, and some rare components such as Gd, Sm, Li and B which have very high absorption cross sections but usually are found with low abundance. Concentration of these elements (Li, B, Gd, Sm and others) is, in general, not known. The total macroscopic neutron absorption cross-section can be

measured using neutron sources [9]. We can take a typical rock matrix composition for the Sandstone and evaluate the macroscopic thermal neutron absorption cross section as in [1].

We consider heterogeneous element distributions such as occur in fracture minerals of the rock matrix and thermal neutrons. The composition of Sandstone is reported in Tab. 3.3.

The composition of the oil is summarized in Tab. 3.4 and the elements that produce ^{14}C in Tab. 3.5.

3.5 Underground ^{14}C Production

The ^{14}C in the biosphere is formed by the bombardment of atmospheric nitrogen with neutrons produced by cosmic radiation $^{14}\text{N}(n, p)^{14}\text{C}$ and enters the biosphere as CO_2 . The weight percentage of carbon in the biosphere is $^{14}\text{C}/^{12}\text{C} = 1.175 \cdot 10^{-12}$. We are interested in the evaluation of the ^{14}C production in a petroleum underground site. The principal ^{14}C production modes that can enter and that we consider are the exothermic reactions summarized in Tab. 3.2 with their thermal cross section [8]. As in [1] in our neutron calculation, we have used *thermal* neutron cross section only, as it dominates the production yield. This corresponds to an energy of 0.0253 eV and is the kinetic energy that a neutron would have at 20°C . Subsurface temperature can vary from this by a factor 2, hence, we can consider the possible error introduced negligible.

Element	Reaction	σ (barn) [11]
^{14}N	$^{14}\text{N} + n \rightarrow ^{14}\text{C} + p$	1.83 ± 0.03
^{17}O	$^{17}\text{O} + n \rightarrow ^{14}\text{C} + \alpha$	0.235 ± 0.01
^{13}C	$^{13}\text{C} + n \rightarrow ^{14}\text{C} + \gamma$	$(1.37 \pm 0.04) \cdot 10^{-3}$
^{11}B	$^{11}\text{B} + \alpha \rightarrow ^{14}\text{C} + p$	0.02

Table 3.2: ^{14}C production reactions.

The $^{14}\text{C}/^{12}\text{C}$ evaluation follows some fundamental steps that are here summarized:

- The first item to evaluate is the *in-situ* neutron flux per volume unit (cm^3) and time (year). For this purpose we need to know the ^{238}U and ^{232}Th contents

(ppm) in the reservoir rock of interest. We will indicate these concentrations as c_U , c_{Th} . The neutrons emitted from 1 ppm of U and 1 ppm of Th by spontaneous fission or by (α, n) reaction in neutrons per gramme per year ($n/g/y$) has been estimated by various authors like in [7] and we will call the different quantities n_{Usp} , $n_{U\alpha}$ and $n_{Th\alpha}$.

As said before the spontaneous fission of ^{232}Th is negligible. The total number of n/g/y in a certain type of rock is:

$$n_{tot}(n/g/y) = c_U \cdot (n_{Usp} + n_{U\alpha}) + c_{Th} \cdot n_{Th\alpha} \quad (3.1)$$

We evaluate the range of n_{tot} for all the cases mentioned in Tab. 3.1. If we insert now the density of the matrix rock we can obtain the number of neutrons per unity volume of rock per year ($n/cm^3/y$):

$$n_{tot}(n/cm^3/y) = n_{tot}(n/g/y) \cdot \rho_r(g/cm^3) \quad (3.2)$$

where (ρ_r) is the matrix density.

- The neutrons produced in the rock will only partially interact in a ^{14}C productive way. They can interact with elements in the rock (Σ_{rock}) or in the oil without producing ^{14}C atoms (Σ_{oil}). Let us denote the fraction of productively absorbed neutrons by P . $\Sigma_{^{14}\text{C}}$ is the total absorption cross section in the oil that produces ^{14}C and ϵ is the porosity of the reservoir rock containing the hydrocarbon and nitrogen. P can be written as

$$P = \frac{\Sigma_{^{14}\text{C}} \cdot \epsilon}{\Sigma_{rock} \cdot (1 - \epsilon) + (\Sigma_{oil} + \Sigma_{^{14}\text{C}}) \cdot \epsilon} \quad (3.3)$$

- We need also the number of ^{12}C atoms per cm^3 . This is equal to the product of the porosity, the oil density ($\rho_{oil} = 0.75 - 0.95g/cm^3$) divided by the mole weight $M = 13.8g$ ($\text{CH}_{1.8}$).

$$n_{^{12}\text{C}}/cm^3 = \epsilon \cdot \rho_{oil} \cdot M \cdot N_A \quad (3.4)$$

The resulting equilibrium level of *in situ* ^{14}C production is:

$$\frac{^{14}\text{C}}{^{12}\text{C}} = \frac{n_n}{n_{^{12}\text{C}}} \cdot P \cdot 5730(y)/\ln 2 \quad (3.5)$$

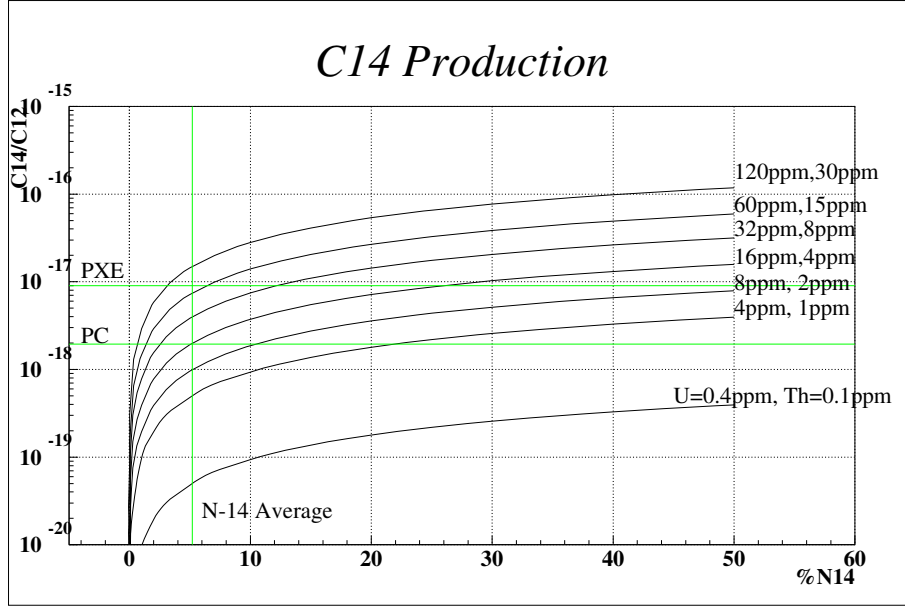


Figure 3.5: $^{14}\text{C}/^{12}\text{C}$ production in underground versus ^{14}N % present.

where $5730/\ln 2$ years is the half life of ^{14}C nuclei.

We evaluate the ratio for different ^{14}N concentration for Sanstone, Limestone and the most realistic cases (Well-1, Well-2, Well-3); the results are in Tab. 3.6 and in Fig. 3.5, Fig. 3.6, Fig. 3.7, Fig. 3.8.

3.6 Conclusion

Our model based on petro-geological data predicts $^{14}\text{C}/^{12}\text{C}$ ratios between $10^{-16} - 10^{-20}$. Large variations are expected depending on the particular amount of nitrogen and on uranium and thorium encountered in the petroleum reservoir. Careful selection of the petroleum reservoir should allow to produce a scintillator low in ^{14}C . Interesting applications as $\nu - e^-$ scattering with pp- ν might be possible.

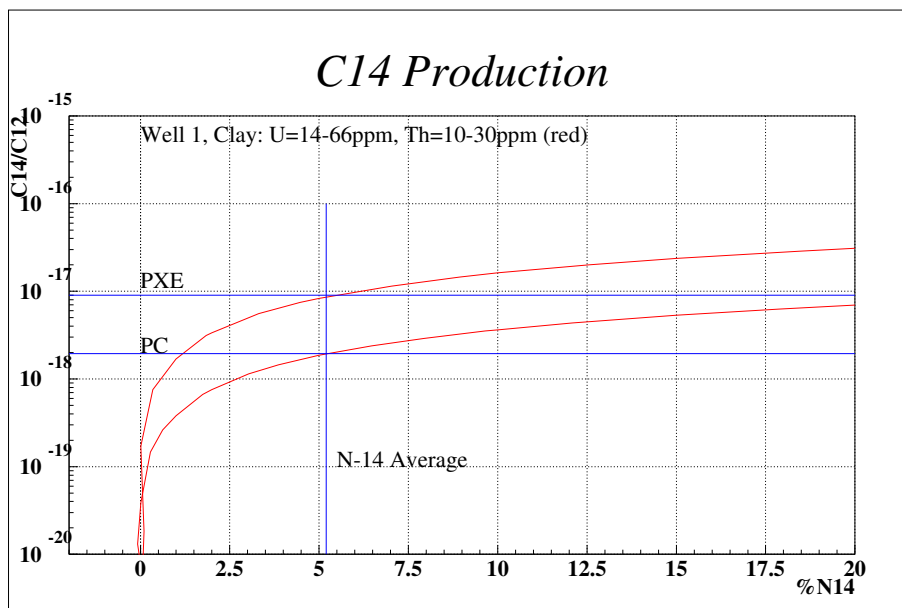


Figure 3.6: Evaluation of $^{14}\text{C}/^{12}\text{C}$ underground production for the well number 1. The values of the ratio measured in PC and in PXE are reported. The area in between the lines corresponds to the expected $^{14}\text{C}/^{12}\text{C}$ ratio.

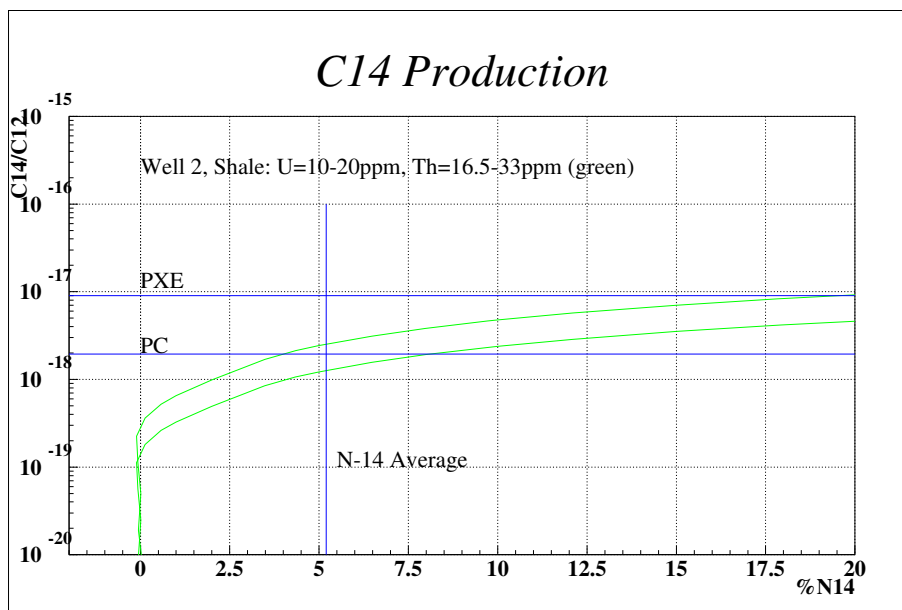


Figure 3.7: Evaluation of $^{14}\text{C}/^{12}\text{C}$ underground production for the well number 2. The values of the ratio measured in PC and in PXE are reported.

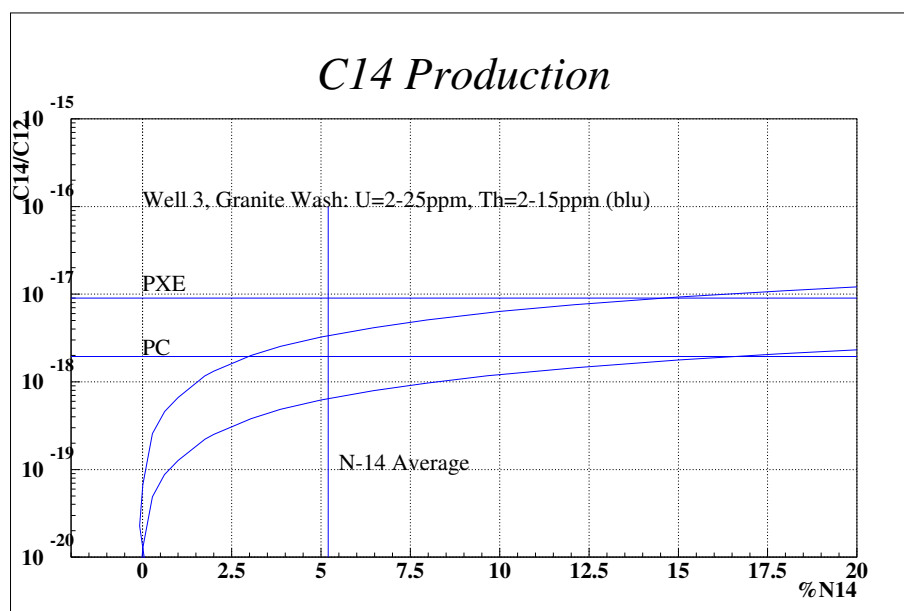


Figure 3.8: Evaluation of $^{14}\text{C}/^{12}\text{C}$ underground production for the well number 3. The values of the ratio measured in PC and in PXE are reported.

Z	A	Elem.	Rel. ab.	σ (therm) (barn)	R. m. c. (ppm)	N. of Atoms (N) $10^{-2}(\text{mole}/\text{cm}^3)$	$N \cdot \sigma 10^{-2}$ (barn mole / cm^3)
1	1	H	1.000	0.33	1800	0.46800000	0.1544400
3	6	Li	0.075	940.00	15	0.00004875	0.0458250
3	7	Li	0.925	0.04	15	0.00051535	0.0000230
4	9	Be	1.000	0.01	1	0.00002889	0.0000002
5	10	B	0.199	3837.00	35	0.00018109	0.6948423
6	12	C	0.989	0.01	10000	0.21428333	0.0007564
6	13	C	0.011	0.01	10000	0.00220000	0.0000030
7	14	N	0.996	1.83	5	0.00009251	0.0001693
8	16	O	0.997	0.01	522000	8.46231165	0.0016078
8	17	O	0.001	0.23	522000	0.00303374	0.0007129
9	19	F	1.000	0.01	270	0.00369473	0.0000355
11	23	Na	1.000	0.93	3300	0.03730434	0.0346930
12	24	Mg	0.790	0.05	7100	0.06075647	0.0030986
12	25	Mg	0.100	0.19	7100	0.00738400	0.0014030
12	26	Mg	0.110	0.04	7100	0.00781710	0.0002986
13	27	Al	1	0.231	25300	0.24362960	0.0562784
14	28	Si	0.922	0.18	367700	3.14906159	0.5573839
14	29	Si	0.047	0.10	367700	0.15395219	0.0155492
14	30	Si	0.031	0.11	367700	0.09878873	0.0105704
17	35	Cl	0.758	44.10	10	0.00005629	0.0024822
17	37	Cl	0.242	0.48	10	0.00001703	0.0000082
19	39	K	0.932	2.1	11000	0.06838927	0.1436175
19	41	K	0.067	1.46	11000	0.00469472	0.0068543
20	40	Ca	0.969	0.41	39500	0.24889602	0.1025451
20	42	Ca	0.006	0.69	39500	0.00158207	0.0010884
20	43	Ca	0.001	6.20	39500	0.00032243	0.0019990
20	44	Ca	0.021	0.88	39500	0.00486891	0.0042846
20	48	Ca	0.002	1.09	39500	0.00040010	0.0004361
22	46	Ti	0.080	0.59	1500	0.00067826	0.0004001
22	47	Ti	0.073	1.70	1500	0.00060574	0.0010298
22	48	Ti	0.738	7.84	1500	0.00599625	0.0470106
22	49	Ti	0.055	2.20	1500	0.00043775	0.0009630
22	50	Ti	0.054	0.18	1500	0.00042120	0.0000754

Z	A	Elm.	Rel. ab.	σ (therm) (barn)	R. m. c. (ppm)	N. of Atoms (N) $10^{-2}(\text{mole}/\text{cm}^3)$	$N \cdot \sigma \cdot 10^{-2}$ (barn mole/ cm^3)
25	55	Mn	1.000	13.30	50	0.00023636	0.0031436
26	54	Fe	0.058	2.25	9900	0.00276467	0.0062205
26	56	Fe	0.917	2.59	9900	0.04215844	0.1091903
26	57	Fe	0.022	2.50	9900	0.00099347	0.0024837
26	58	Fe	0.003	1.28	9900	0.00012426	0.0001590
62	144	Sm	0.031	0.70	10	0.00000056	0.0000004
62	147	Sm	0.150	57.00	10	0.00000265	0.0001512
62	148	Sm	0.113	2.40	10	0.00000198	0.0000047
62	149	Sm	0.138	40140.00	10	0.00000241	0.0966593
62	150	Sm	0.074	104.00	10	0.00000128	0.0001334
62	152	Sm	0.267	206.00	10	0.00000457	0.0009408
62	154	Sm	0.227	8.40	10	0.00000383	0.0000322
64	152	Gd	0.002	735.00	10	0.00000003	0.0000251
64	154	Gd	0.022	919.70	10	0.00000037	0.0003385
64	155	Gd	0.148	60900.00	10	0.00000248	0.1511891
64	156	Gd	0.205	1.50	10	0.00000341	0.0000051
64	157	Gd	0.156	254000.00	10	0.00000259	0.6582968
64	158	Gd	0.248	2.20	10	0.00000409	0.0000089
64	160	Gd	0.219	0.77	10	0.00000355	0.0000027
Tot:							$2.9 \cdot 10^{-2}$
$\Sigma_{rock}(\text{cm}^2/\text{cm}^3)=$							$1.7 \cdot 10^{-2}$

Table 3.3: Calculation of the macroscopic thermal neutron absorption cross section for a sandstone elemental composition of the rock, Σ_{rock} . R. m. c. stays for rock matrix composition.

Z	A	Elm.	Rel. ab.	σ (therm) (barn)	Petroleum conc. (%)	Num. of Atoms (N) (mole/cm^3)	$N \cdot \sigma$ (barn mole/cm^3)
1	1	H	1.000	0.33	12.5	0.106250	0.0350625
6	12	C	0.989	0.01	85.0	0.059546	0.0002102
8	16	O	0.998	0.01	1.0	0.000530	0.0000001
16	32	S	0.950	0.53	0.5	0.000126	0.0000669
16	33	S	0.007	0.54	0.5	0.000001	0.0000005
16	34	S	0.042	0.23	0.5	0.000005	0.0000012
						Sum(b mole/cm3)=	$3.5 \cdot 10^{-2}$
						$\Sigma_{oil}(\text{cm}^2/\text{cm}^3) =$	$2.1 \cdot 10^{-2}$

Table 3.4: Calculation of the macroscopic thermal neutron absorption cross section for a petroleum typical composition, Σ_{oil}

Z	A	Elm.	Rel. ab.	σ (therm) (barn)	Petroleum conc. (%)	Num. of Atoms (N) (mole/cm^3)	$N \cdot \sigma$ (barn mole/cm^3)
6	13	C	0.011	0.00137	85	$6.1 \cdot 10^{-4}$	$8.4 \cdot 10^{-7}$
8	17	O	0.00038	0.235	1	$1.9 \cdot 10^{-7}$	$4.5 \cdot 10^{-8}$
7	14	N	0.99634	1.83	1	$6.0 \cdot 10^{-4}$	$1.1 \cdot 10^{-3}$
						Sum(b mole/cm3)=	$1.1 \cdot 10^{-3}$
						$\Sigma_{^{14}\text{C}}(\text{cm}^2/\text{cm}^3) =$	$6.7 \cdot 10^{-4}$

Table 3.5: Calculation of the ^{14}C production factor in Oil, $\Sigma_{^{14}\text{C}}$

^{14}N (%)	$^{14}\text{C}/^{12}\text{C}_{min}$ Sandstone	$^{14}\text{C}/^{12}\text{C}_{max}$ Sandstone	$^{14}\text{C}/^{12}\text{C}_{min}$ Limestone	$^{14}\text{C}/^{12}\text{C}_{max}$ Limestone
0	$1.06 \cdot 10^{-24}$	$1.74 \cdot 10^{-22}$	$2.80 \cdot 10^{-25}$	$1.35 \cdot 10^{-21}$
1	$1.32 \cdot 10^{-21}$	$2.15 \cdot 10^{-19}$	$3.48 \cdot 10^{-22}$	$1.67 \cdot 10^{-18}$
5	$6.53 \cdot 10^{-21}$	$1.03 \cdot 10^{-18}$	$1.73 \cdot 10^{-21}$	$8.00 \cdot 10^{-18}$
10	$1.29 \cdot 10^{-20}$	$1.96 \cdot 10^{-18}$	$3.42 \cdot 10^{-21}$	$1.52 \cdot 10^{-17}$
20	$2.54 \cdot 10^{-20}$	$3.58 \cdot 10^{-18}$	$6.72 \cdot 10^{-21}$	$2.78 \cdot 10^{-17}$
50	$6.02 \cdot 10^{-20}$	$7.08 \cdot 10^{-18}$	$1.59 \cdot 10^{-20}$	$5.49 \cdot 10^{-17}$

Table 3.6: Range of the ^{14}C production in underground in Sandstone and in Limestone. The nitrogen varies from 0 to 50 %. The levels obtained can explain the ^{14}C levels detected in CTF.

Bibliography

- [1] R. Zito, D.J. Donahue, S.N. Davis, H.W. Bentley, P. Fritz, *Possible subsurface production of Carbon-14*, Geophys. Res. Lett., vol. 7, No. 4, 235-238, (1980).
- [2] A.I. Levorsen, *Geology of petroleum*, edited by J.A. Gilluly and A.O. Woodford.
- [3] W.L. Russel, *Principles of Petroleum Geology*, edited by McGraw-Hill, 1960.
- [4] H.J. Neumann et al., *Composition and Properties of Petroleum*, edited by Heinz Bec.
- [5] Y. Feige et al., *Production Rates of Neutrons in Soils Due to Natural Radioactivity*, J. Geophys. Res. Vol. 73, No 10 (1968), 3135.
- [6] W. H. Fertl, *Gamma Ray Spectral Data Assists in Complex Formation Evaluation*, Dresser Atlas Division.
- [7] T. Florkowski et al., *Natural Production of Radionuclides in Geological Formations*, Nucl. Geophys Vol 2. No 1 pp 1-14 (1988).
- [8] J.N. Andrews et al., *Geochimica et Cosmochimica Acta*, Vol.53, pp.1803-1815.
- [9] A. Kreft et al., *Int. J. Appl. Radiat. Isot* 35(7), 373-375 (1984)
- [10] *Table of Isotopes*, R.B. Firestone, Virginia S. Shirley, cdrom edition vers. 1.0, March'96.
- [11] National Nuclear Data Center (Brookhaven National Laboratory), <http://www.nndc.bnl.gov>

The Counting Test Facility (CTF) of Borexino

The goal of CTF-1 ('95-'97) was to study the feasibility of Borexino with the main focus on radioactive impurities in the scintillator material. The energy range below 1 MeV was of primary interest. The CTF was designed for ^{238}U , ^{232}Th and ^{14}C spectroscopy and for the study of the optical response of a big volume of liquid scintillator. The sensitivity for neutrino interaction, ^{40}K , and ^7Be is not sufficient for Borexino because the surface/volume ratio limits the self-shielding. I will report in the next sections a short description of the structure of the detector and the main goals achieved from CTF-1.

Once completed the data taking of CTF-1 the construction of Borexino started. The goals of the test facility were then re-analysed. The radioactive contents of the materials selected for Borexino and its ancillary systems are measured with different counting methods. The techniques used are large volume Ge spectrometry [16] (U, Th sensitivity $\sim 10^{-10}g/g$), Rn emanation counting [17] (sensitivity down to several $\mu\text{Bq}/m^3$), NAA and mass spectrometry.

^{14}C levels at $^{14}\text{C}/^{12}\text{C} \sim 10^{-18}$ can only be measured with the CTF.

Moreover, Borexino liquid handling and purification systems should be tested and optimised with respect of radiopurity after installation on site in order to guarantee the high purity standard requested. The ideal facility for this campaign of measurements is the CTF. For these reasons the Counting Test Facility of Borexino restarted data taking during May 2000.

Some fundamental upgrades were introduced in order to increase the stability of the detector response and the Rn shield of the active part.

I will report in the following sections the description of the upgraded parts of the

detector, but in particular I will describe the preparation of the PMTs, and installation that correspond to a fundamental part of my contribution to the startup of this second phase of CTF.

4.1 Feasibility of Borexino: CTF-1

A brief description of the structure of CTF-1 and a summary of the main results achieved is reported here.

4.1.1 Structure of the Detector

The structure of the CTF detector is described comprehensively in [1]. Here, I will only report the main informations concerning the hardware setup which are of relevance for CTF-2.

CTF is located near Borexino in the hall C of the Gran Sasso underground laboratories. The active detector is composed by 4.8 m^3 organic liquid scintillator contained in a thin (0.5 mm) nylon spherical vessel of 2 meter diameter (Inner Vessel, IV). Two samples of liquid scintillator were tested: the first is PC (1,2,4-trimethylbenzene, density 0.88 g/cm^3) as solvent with PPO (2,5-diphenyloxazole, 1.5 g/l concentration) as fluor. The light yield of the mixture studied is 300 ± 30 photoelectrons/MeV. The second scintillator measured is based on PXE solvent (phenyl-o-xylylethane, $\text{C}_{16}\text{H}_{18}$, density 0.99 g/cm^3) with p-tp (2 g/l) as fluor and bis-MSB as shifter (20 mg/l).

The constraints that brought to the idea of a membrane balloon 0.5 mm thick rather than a rigid vessel were the optical transparency and the very low radioactivity level requested. The nylon vessel didn't show transparency deterioration during all the two years of data taking. On the other hand the lower density of PC with respect to water creates a buoyancy force in case of a water buffer that complicates the scintillator containment. The spherical shape was difficult to maintain. The PXE scintillator was proposed as its density is very similar to water density. Questions not yet solved about the optical properties of PXE requested a second test. For Borexino a PC buffer was chosen in order to eliminate the buoyancy force problem. PXE together with a water buffer is a back-up solution.

Radon diffusion through the nylon membrane was observed and can limit the sensitivity of the detector. In order to reduce this effect a second nylon vessel (Radon Barrier or Outer Vessel OV) is implemented for CTF-2 and Borexino.

The light emitted from the scintillator is detected by 100 PMTs placed on a spherical open structure 2.3 meters far from the IV. The PMTs are coupled with light concentrators in order to increase the surface coverage to about $\sim 31\%$.

All the structure is immersed in ~ 1000 tons of pure water contained in a carbon steel tank (D200). The water provides a 4.5 meter shield from γ - ray background from the rock of the hall and a 2.3 meter shield from the PMT induced background.

A water purification plant is placed near the D200. Water is purified through filtration, reverse osmosis, deionization, ion exchange, and nitrogen stripping [2, 3]. The CDI unit reduces the ionic activity of the raw water from 10^{-10} g U,Th/ g water to 10^{-14} gram of U and Th per gram of water. The radon contents in water after nitrogen stripping are reduced to ~ 20 mBq/m³. Conductivity, pH and temperature of the water inside the D200 were monitored at three different locations. Samples of water were tested for radon contamination directly in hall C with a preconcentration method followed by counting in a miniaturised low background gas counter that achieved a sensitivity of 1mBq/m³ [4]. Water samples were also tested for U and Th by inductively mass spectroscopy and neutron activation (NAA) [5] with a sensitivity of $2 \cdot 10^{-16}$ g U,Th/g water.

A fluid handling system performs the filling and the emptying of the inner vessel with different liquids (water, liquid scintillators), circulates scintillator through a purification system and maintains a pressure head on the liquid contained in the inner vessel.

The scintillator purification system was composed by sub-micron filtration, water extraction, vacuum distillation, and nitrogen stripping [8, 9]. Filtration removes suspended dust particles larger than $0.05 \mu m$. Water extraction removes ionizable species like metals (U, Th, K). Vacuum distillation removes low volatility components such as metals and dust particles. Nitrogen stripping removes dissolved gas impurities (^{85}Kr) and water dissolved in the scintillator.

A purification system based on a solid column was added during the last period of

data taking. It was tested on PXE scintillator. It succeeded in reducing the U and Th level of several orders of magnitude down to $\sim 10^{-17}$ g/g for U and $\sim 10^{-16}$ g/g for Th.

For mainly stripping operations but also for flushing D200 tank and inflating the IV pure nitrogen is needed (some $\mu Bq/m^3$). Nitrogen from commercial vendors was used but the Rn contents were one or two orders of magnitude higher than the requested level. For Borexino, CTF-2 and purification systems a nitrogen purification plan is added.

A test setup composed of two Ar-methane multiwire proportional chambers was added during the data taking in order to sample part of the muons that enter in CTF [10]. The results showed the need to identify muon signals in Borexino with an efficiency of 99.9999%. The flux of neutrons correlated with muons is ~ 0.3 neutrons/ton/day.

Details about PMTs and data acquisition are described below just for CTF-2.

4.1.2 Results Achieved

The results of CTF-1 are summarized in [1, 11, 12, 13] and the different phases of the entire data taking are described in details in [14]. I report here highlights which are useful for the following CTF-2 discussion.

The radioactive elements investigated are the ones that represent the fundamental sources of background in Borexino. As mentioned above, the three categories of radioactive contaminants which were investigated are the primordial ^{40}K and ^{238}U , ^{232}Th chains, the noble gases ^{222}Rn and ^{85}Kr and the cosmogenic elements ^{14}C , 7Be . The CTF-1 main results with PC(PPO) and PXE(TP) are summarized in Tab. 4.1 where I report for some elements the corresponding measurements realized with Neutron Activation Analysis (NAA) [5, 6]. NAA measures directly the concentration of ^{238}U and ^{232}Th nuclei while CTF detects the delayed coincidences $^{214}Bi(\beta\gamma) - ^{214}Po(\alpha)$ ($236\mu s$) and $^{212}Bi(\beta\gamma) - ^{212}Po(\alpha)$ (432.8 ns). In other words CTF is sensible to $^{226}Ra - ^{214}Po$ segment of ^{238}U chain and to the entire segment following ^{226}Ac in the ^{232}Th chain. If CTF and NAA measurements are in agreement the decay chains should be in secular equilibrium.

In CTF, α decays are separated from β events using the PSD (Pulse Shape Discrimination) analyzes. The identification efficiency of α events in CTF-1 is $\sim 97\%$ at 751 keV (^{214}Po) with an associated β misidentification of $\sim 2.5\%$. At lower energies it decreases to 90%. More details about the α/β discrimination are reported in the CTF-2 results section.

Rn emanation from the materials and its diffusivity in liquids and through solids were found fundamental problems to be addressed in a low energy experiment. During CTF-1 data taking, Rn was observed in the shielding water ($\sim 30\text{mBq/m}^3$) probably due to emanation of the materials present in the tank. In the scintillator Rn was found after each operation through the liquid handling or the purification system. A significant improvement in this field is realized in CTF-2.

Element	PC (CTF)	PC (NAA)	PXE (CTF)	PXE (NAA)
^{238}U	$(3.5 \pm 1.3) \cdot 10^{-16} \text{g/g}$	$\leq 2 \cdot 10^{-16}$	$(1.0 \pm 0.4) \cdot 10^{-15}$	$\leq 1 \cdot 10^{-17} \text{g/g}$
^{232}Th	$(4.4 \pm 1.5) \cdot 10^{-16} \text{g/g}$	$\leq 2 \cdot 10^{-15}$	$(2.0 \pm 0.5) \cdot 10^{-15}$	$\leq 2 \cdot 10^{-16} \text{g/g}$
^{85}Kr	$365 \pm 10 \text{count/day}$	-	-	-
$^{14}\text{C}/^{12}\text{C}$	$(1.94 \pm 0.09) \cdot 10^{-18}$	-	$9 \cdot 10^{-18}$	-
K_{nat}	$\leq 2.4 \cdot 10^{-11} \text{g/g}$	$\leq 4 \cdot 10^{-12}$		$\leq 6 \cdot 10^{-12}$

Table 4.1: CTF-1 results: ^{238}U and ^{232}Th CTF-1 results for PC are consistent with NAA measurements. We have no indication that secular equilibrium is broken. The sample of PXE measured with NAA corresponds to the last obtained after several purification column operations. Due to the shut down of CTF-1 it was not possible to measure the same sample in CTF-1. The value reported for CTF-1 measurements concerns a sample less purified. ^{85}Kr is tagged by the $^{85}\text{Kr}(\beta) - ^{85}\text{Rb}(\gamma)$ correlation. The initial Kr activity observed was successfully purified with nitrogen sparging down to the sensitivity level of CTF-1. The ^{14}C activity remained stable over a year of data taking. For K_{nat} we report an upper limit corresponding to the sensitivity level of CTF. The level needed in Borexino is $K_{\text{nat}} < 10^{-14} \text{g/g}$.

The study of a big volume of liquid scintillator in a 4π geometry has given interesting results also about the propagation of light in the scintillator. The mechanisms involved are discussed in [13] and are absorption and reemission of light from the fluor and the elastic scattering of light by the solvent. The quantification of these two effects was possible after the insertion of ^{222}Rn sources in CTF. From a comparison with simulation it was evaluated that in PC+PPO 46-56% of the original light

emitted is directly detected, 22% is absorbed and remitted and 12-14% is lost. Due to this effect the effective scintillator decay time of ~ 3.5 nsec increases to $4.5 - 5.0$ nsec.

4.2 Quality Control of Borexino: CTF-2

4.2.1 PMT: Characteristics, Sealing and Test.

In CTF the detection of the signal produced by the liquid scintillator is realized by 100 photomultipliers (PMT) Thorn EMI 9351 of 0.2 m diameter (same type as in Borexino). They are distributed on a spherical open structure composed by six horizontal rings centered along z axis. The PMTs are coupled to “truncated string cone” light concentrators (l.c.) which improve the scintillation light collection; they are 57 cm long and 50 cm aperture, they were fabricated with low radioactivity UV-transparent acrylic with thin layers of silver and copper deposited on the outer surface of the acrylic. The metal layers were coated with an acrylic paint [18]. The geometrical coverage of the active scintillator region is $\sim 21\%$. Less than half of the CTF-1 l.c. was damaged during the two years of immersion in water probably due to micro scratches on the acrylic surface. They were replaced with new ones of the same type.

A μ -metal shield is mounted on the PMT in order to screen the dynodes from the earth’s magnetic field.

Some of the most important characteristics of our PMTs are:

- *Photocathode quantum efficiency* of $\sim 25\%$ (peaked at 380 nm); this parameter influences critically the spatial resolution, the time resolution and the signal threshold.
- *Single photoelectron transit time spread* of 1 ns influences directly the spatial resolution in the event reconstruction and the overall uncertainty in the definition of the fiducial volume.
- *Afterpulses* can limit the possibility to distinguish alpha and beta induced signals. The selected tubes have a probability of 2.5%.
- *Dark count rate*: it determines the minimal number of coincident tubes chosen for the threshold definition that can keep within a reasonable limit the random trigger rate. The darknoise per tube is typically between $500 - 1000 Hz$.

- *Single photoelectron pulse height resolution*: it assures a precise threshold setting and a careful stability control of the tube performances during the operation of the detector.

The high voltage of the PMTs is set in order to have a fix amplification of 10^7 .

The development of a new water sealing design

PMTs are electrical devices that should work, in our case, in ultrapure and deionized water for a long period of time. Therefore, a sealing of the apparatus is needed. The sealing realized for the CTF-1 PMTs revealed several and serious structural problems causing a failure of more than half of them. A completely new sealing design was applied for the CTF-2 PMTs. The development was realized in parallel to Borexino PMTs sealing design and I participated in both developments.

The part of the tube to be protected, i.e. the pins and the voltage divider mounted in them, are enclosed in a cylindrical stainless steel housing filled with different layers of potting materials. An underwater connector and an underwater cable, the same developed for Borexino, assure the stability of the electrical response.

The development of the encapsulation, the qualification of the prototypes and the final production of the sealed PMTs were made in Gran Sasso lab. The work was developed in three main steps: the selection of the materials and the design of the prototype, the qualification of the prototype via accelerated aging test and the final production of 110 sealed PMTs.

The materials involved are selected on the base of the following parameters:

- *Water compatibility*: it is usually measured by the producer company in percent of water absorbed from the material at saturation. If the water absorbed is less than 2% the plastic can be considered water proof. We also performed water compatibility tests on different samples putting them in water for a long period at room temperature or for a shorter time at increased temperature $40 - 50^\circ\text{C}$.
- *Low radioactivity contamination*: in order to reduce as much as possible the insertion of radioactive contaminants in the detector each candidate material was measured and selected on the base of gamma ray activity and Rn emanated. The gamma activity was measured by means of germanium diodes at the underground Gran Sasso low background facility [16]. The Rn emanation is performed at Heidelberg by a collaborating group [17].

The results for the materials selected are summarised in Tab. 4.2. The radon emanation of the PMT glass bulb is $25 \mu Bq$. The total radioactive contribution of a PMTs is $\sim 3.8 Bq$.

The PMT sealing design realized for CTF-2 PMTs is sketched in Fig. 4.1.

An alternative sealing design was realized by the Munich group for the CTF-2 and Borexino muon veto PMTs. The PMT is in this case completely encapsulated in a stainless steel housing closed with a PET window. The volume inside is filled with mineral oil. 16 PMTs sealed in this way are installed on the floor of CTF in two concentrical rings in order to test them and to implement a partial muon veto.

	^{238}U ($10^{-9}g/g$)	^{226}Ra (g/g)	^{232}Th ($10^{-9}g/g$)	K_{nat} (g/g)	^{60}Co (mBq/kg)
PMT's Materials:					
ETL low rad. glass	31 ± 2	$66 \pm 19 \cdot 10^{-9}$	32 ± 3.2	$16 \pm 4 \cdot 10^{-6}$	-
Voltage divider	55 ± 3	-	79 ± 6	$1 \pm 0.1 \cdot 10^{-4}$	≤ 19
Potting Materials:					
Polyurethane (Sanyu resin)	2.6 ± 0.3	$\leq 7.7 \cdot 10^{-9}$	≤ 1.2	$\leq 2 \cdot 10^{-6}$	≤ 2.4
Silicone Gel (RTV 6196)	3.9 ± 0.7	-	≤ 3.7	$\leq 3.9 \cdot 10^{-6}$	≤ 4.5
BPA1000	≤ 4.05	-	≤ 7.38	$\leq 6.5 \cdot 10^{-6}$	≤ 20
Housing (AISI304)	0.22 ± 0.03	2.7 ± 0.4 (mBq/Kg)	0.4 ± 0.2	$\leq 7.5 \cdot 10^{-8}$	5.9 ± 0.2

Table 4.2: Radioactive levels of the different PMT's components.

In order to evaluate the long term effects of the water on the PMT the working group realized the following different setups:

- a little water tank for one PMT equipped with a heating and pressurized system. By increasing the temperature and the pressure we can stress the materials involved and simulate an accelerated aging of the prototype (ASTM test). This tank is used in the first phase of the development where the prototype is qualified. With this test we look for the main problems of a new design. The electrical response of the

sealed PMT is monitored during an immersion time of 1-2 months. The temperature applied is 45°C and the over pressure is 3 bar. This test was performed on 2 prototypes of the final design with success.

- 3 bigger water tanks for 20 PMTs that can be overpressurised at 2 atm are used to stress a higher number of prototypes. 5 CTF-2 prototypes were immersed for a period of 3 months at 2 atm without showing any particular damage.
- a 56 PMTs cylindrical tank, built in order to perform a two liquid (water/PC) test for the Borexino PMTs, is finally used for the final check of the water tightness of the sealed CTF-2 PMTs. The CTF-2 PMTs were immersed in water for a period of 2 weeks in order to control the possible presence of construction mistakes. No PMTs showed any problems during this immersion time.

The final encapsulated PMT was realized following the steps:

- Voltage Divider (VD) connection:

the first step is the installation of the VD on the PMT.

The main functions of the PMT VD are to maximise the PMT efficiency as well as to minimize the transit time "spread" and to produce a good shape of the analogous signal. The complete schematic diagram of the voltage divider for the Borexino and CTF-2 PMTs is showed in Fig. 4.2. A single coax cable carrying both the PMT output signal and the High Voltage will be used to connect PMT and front-end electronic input channel. Signal and HV are coupled/decoupled at the input of the front-end electronic on one side and at the divider on the other. On the divider side this is accomplished by R2, R3, R4 and C2. The two resistors R2 and R3 have been added to the circuit to optimise the signal shape. Their values, as well as the values of the dumping resistors on the last four dynodes (R6, R8, R10 and R12) have all been empirically determined for the same purpose. An "AC coupled resistor" network (C1/R1, 50 Ohm in series with 4.7nF) have been added to provide some level of cable back termination in order to minimise possible signal reflections on the transmission line. The dividers are supplied with positive high voltage. Current divider design provides a linear voltage distributions on all but the first two dynodes of the PMT. There we allow for a somewhat larger voltage drops in order to optimise the PMT performance for our purposes. The voltage across the cathode and the first dynodes is fixed, by means of use of the Zener diodes D1 to D3, to the value (600V) suggested by the PMT manufacturer for

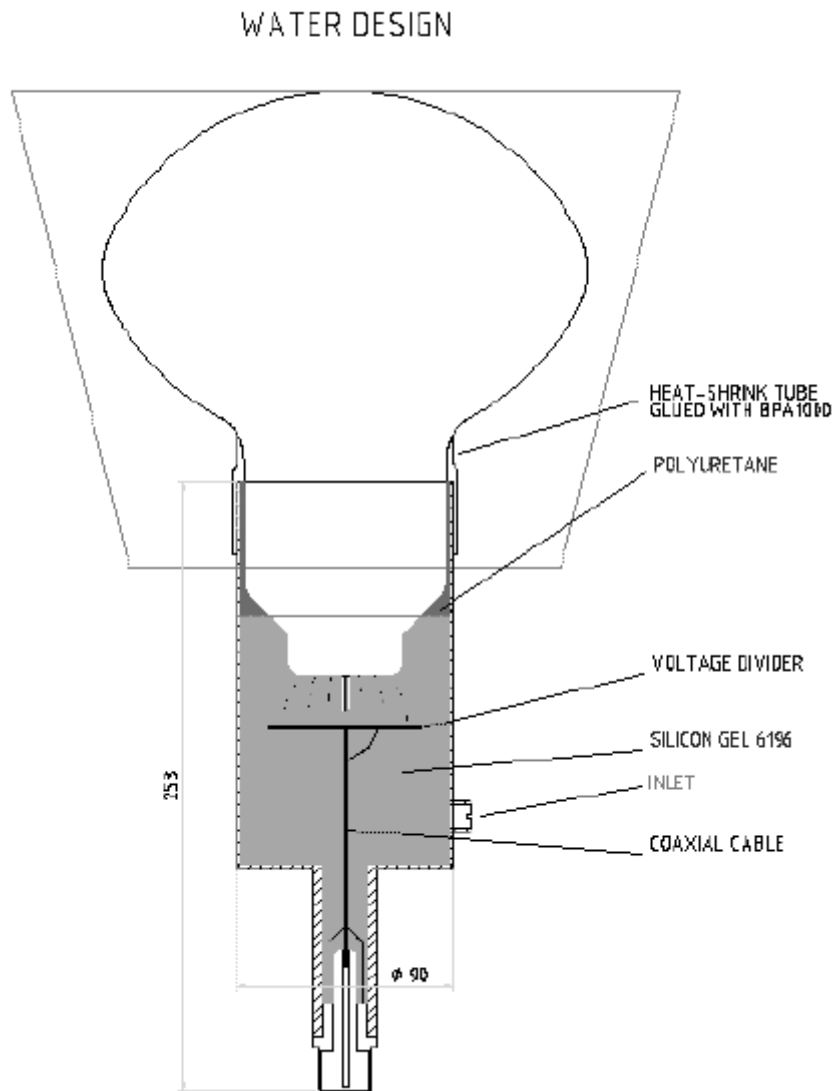


Figure 4.1: Design of the sealed CTF-2 PMT

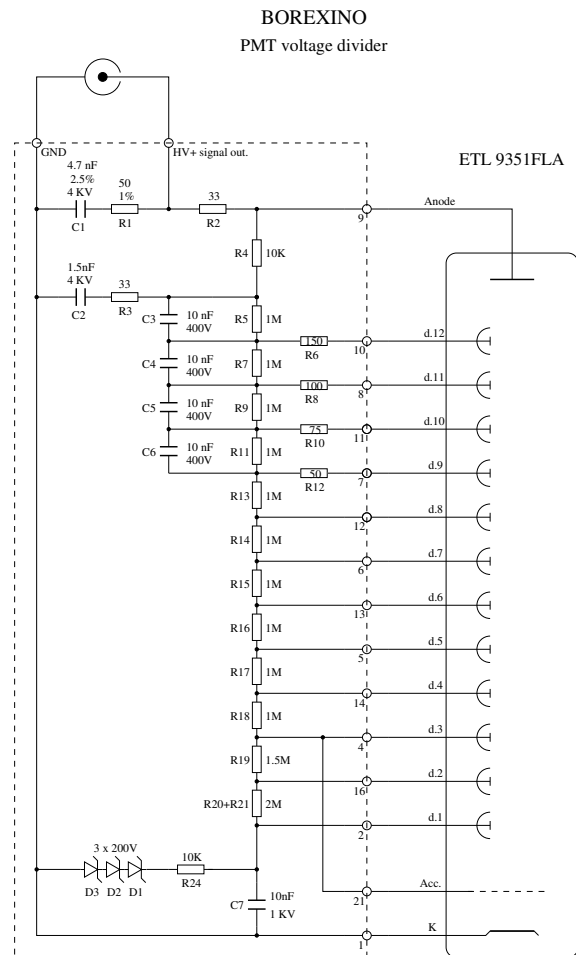


Figure 4.2: CTF-2 Borexino PMT voltage divider

the optimum PMT performance. An R-C low pass filter network (R24/C7) is used to minimise the wide band noise that might be introduced by the Zeners. The materials involved were checked for their radioactive contamination.

- Dark room test:

the electrical response of all the CTF-2 PMTs was tested before, during and after the sealing operation. The electrical connection of 3 PMTs broke during sealing operation. No other changes in the PMTs electrical performances were observed during sealing phase. The facility used for these tests is the Dark Room (DR) set up in Gran Sasso laboratories by the PMT working group. It is able to test and characterise 64 PMTs per time. The PMTs are placed on 4

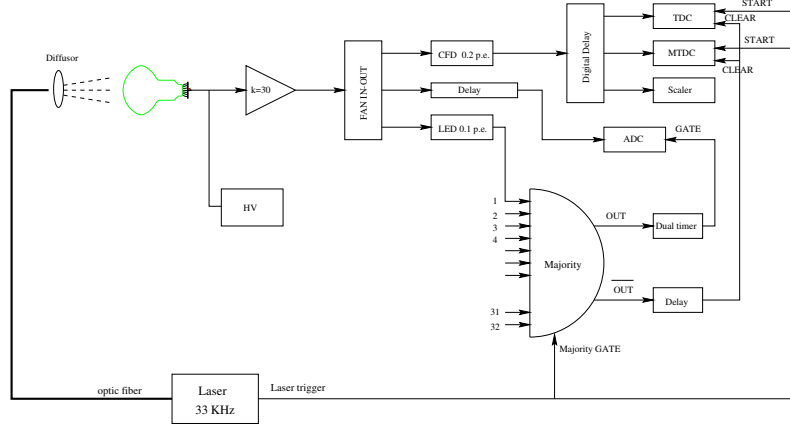


Figure 4.3: Electronic setup of CTF-2 and Borexino dark room. 64 PMTs can be tested in the same time.

tables which are introduced in a region of the room where the earth magnetic field (EMF) is shielded from a 6 square coils system. Magnetic fields even as weak as the EMF affect our PMT performances. Tubes with linear focusing dynodes like ours are most sensitive to magnetic influence when the field is parallel to dynodes. A 5% degradation of the PMT parameters (transit time spread, peak-to-valley ratio, single photoelectron response) is observed when the magnetic field along one reference axis is $10 \mu T$. In the room the EMF measured is about $35 \mu T$ in the vertical direction, $25 \mu T$ along the north-south direction and $8 \mu T$ along east-west direction. A daily change around $0.05 \mu T$ is observed.

Each table is equipped with a light fiber setup in order to have a known light source. The setup of the system is sketched in the Fig. 4.3.

- Sealing:

the female connector pre-mounted at the bottom of the stainless steel housing is connected via a 10 cm long cable to the Voltage Divider. The glass neck of the PMTs, never perfectly cylindrical, is then adapted to the housing with a Teflon tape (see Fig. 4.4). The external interface from the glass and the housing is fixed with a pretreated thermoshrink glued with a proper product named BPA1000 (see Fig. 4.5). After 3 days of polymerization (see Fig. 4.6) and a visual test of the good adhesion of the thermoshrink we started the potting of the internal volume of the housing. From a hole in the housing we



Figure 4.4: First step of the sealing: wrap teflon tape around the neck of the PMT in order to optimize the coupling from the bulb and the stainless steel housing.

inserted 20cc of a preselected polyurethane. The PMTs was in vertical position during polymerization. This layer strengthens the mechanical coupling PMT-housing but in a non rigid way. The remain volume was filled with a preselected reformable silicon gel (see Fig. 4.8) that will be the main water barrier. We selected a soft material in order to decrease the possible internal stresses due to temperature and pressure changes. Both glues were separately degased under vacuum (see Fig. 4.7) in order to avoid air bubble trapping that can decrease the barrier against water.



Figure 4.5: Second step of the sealing: glue the neck of the PMT to the stainless steel housing.

4.2.2 Cables and Connectors

In Borexino as in CTF cables and connectors will work immersed in ultrapure and deionized water for a long period of time. This has required to find solutions and materials explicitly developed for submarine applications. The two fundamental requests concern the material compatibility on long term immersion and the electrical performances. Plastic material with a very low water absorption plus a very low radioactivity contamination and a multiple barrier against radial and axial diffusion of water was the selection done. High density polyethylene coupled with a second layer of metal tape guarantees a good impermeable cover of the cable. The cable selected is a coaxial RG 213 from Huber-Suhner and has the following electrical characteristics: impedance $50 \pm 2\Omega$, attenuation ~ 6 dB/100m at 100 MHz, max operating voltage ≥ 2.5 kV rms. Other characteristics are: weight ≤ 17 kg/100m and minimum bending radius ≤ 70 mm (bending once).

Borexino and CTF connectors will work in a non critical pressure environment (< 2 bar), however the long time of immersion sets stringent constraints on the final choice. The wide research done from the PMT w.g., in particular from Eng. P. Lombardi and Eng. G. Ranucci comprised different companies with a long standing experience in submarine field. The final decision was for the Jupiter company.



Figure 4.6: Third step of the sealing: 3 days upside down for the polymerization.



Figure 4.7: Degasing of the silicon gel under vacuum. Air bulbes trapped in the glue can decrease the property of the glue.



Figure 4.8: After the silicon gel filling the PMTs stay 24 hours horizontal. After the polymerization of the gel we close the filling hole with a metal cap.

4.2.3 Electronic and DAQ System

The 100 PMTs of CTF are read from a NIM-CAMAC data acquisition system. The number of electronic channels is 64. 28 of them read single PMT and 36 read PMTs coupled to pairs. Two separate chains allow the record of delayed coincidences. The hardware installed is composed by:

- Group 1: it is the main electronic chain that records the charge and the time of arrival of the photons when a trigger happened. It is composed by 100 ADC, 64 TDC and scalars. 100 ADC are needed because the setting of the single photoelectron peak of each PMT HV is realized by ^{14}C monitor.
- Group 2: a separate chain records the charge and the time of the PMTs only if a second trigger within 8 msec arrives after the main one. With this logic we can record mainly the Bi-Po delayed coincidences. It is composed of 64 ADC, 64 TDC and scalars.
- α/β discrimination: the system from the CTF-1 is implemented. It is composed of 24 ADC and performs the standard tail/total ratio.
- Long Range TDC
- TTR: two modules record the shape of the pulse .
- Muon veto: 16 PMTs on the floor of CTF are dedicated to record the Čerenkov light produced in the water of the CTF. The reading is made by a dedicated system composed of 16 ADC and 16 TDC.

The Data Acquisition system (DAQ) is composed of three main parts:

- Producer: it handles the ADC, TDC registers of the 100 PMTs and the 16 muon veto PMTs, the LTDC registers, the α/β new and old system. It handles the HV software driver and it runs the HV tuning algorithm.
- Consumer: it creates the event buffer.
- Analyzer: it produces histograms needed for an on-line analysis.

4.2.4 Inner Vessel (IV) and Outer Vessel(OV)

The IV of CTF-2 was realized with no fundamental modification with respect to the IV of CTF-1. A nylon sphere with one meter radius is placed in the center of the open structure. The CTF-1 adjustable hold-down system that retains the vessel against the buoyant force was used. The main innovation concern the radon barrier or Outer Vessel (OV). As discussed before, the high radon level in the CTF-1 water (30 mBq/m^3 , instead of 1 mBq/m^3) limits the sensitivity of the internal background measurements. A second barrier is planned to keep the radon away from the scintillator vessel. It is produced with a nylon film of $100 \mu\text{m}$ thickness and it is placed at 1 meter distance from the IV (see figure below).

4.2.5 Water System and Nitrogen System

The Water System is essentially the old CTF-1 system with the following main improvements: a new resin system (Residion) specifically designed to reduce the radium contents in water, an improved radon concentration vessel that can perform measurements down to about 0.2 mBq/m^3 for ^{222}Rn and to about 2 mBq/m^3 for ^{226}Ra and an improved nitrogen system in terms of radon contents.

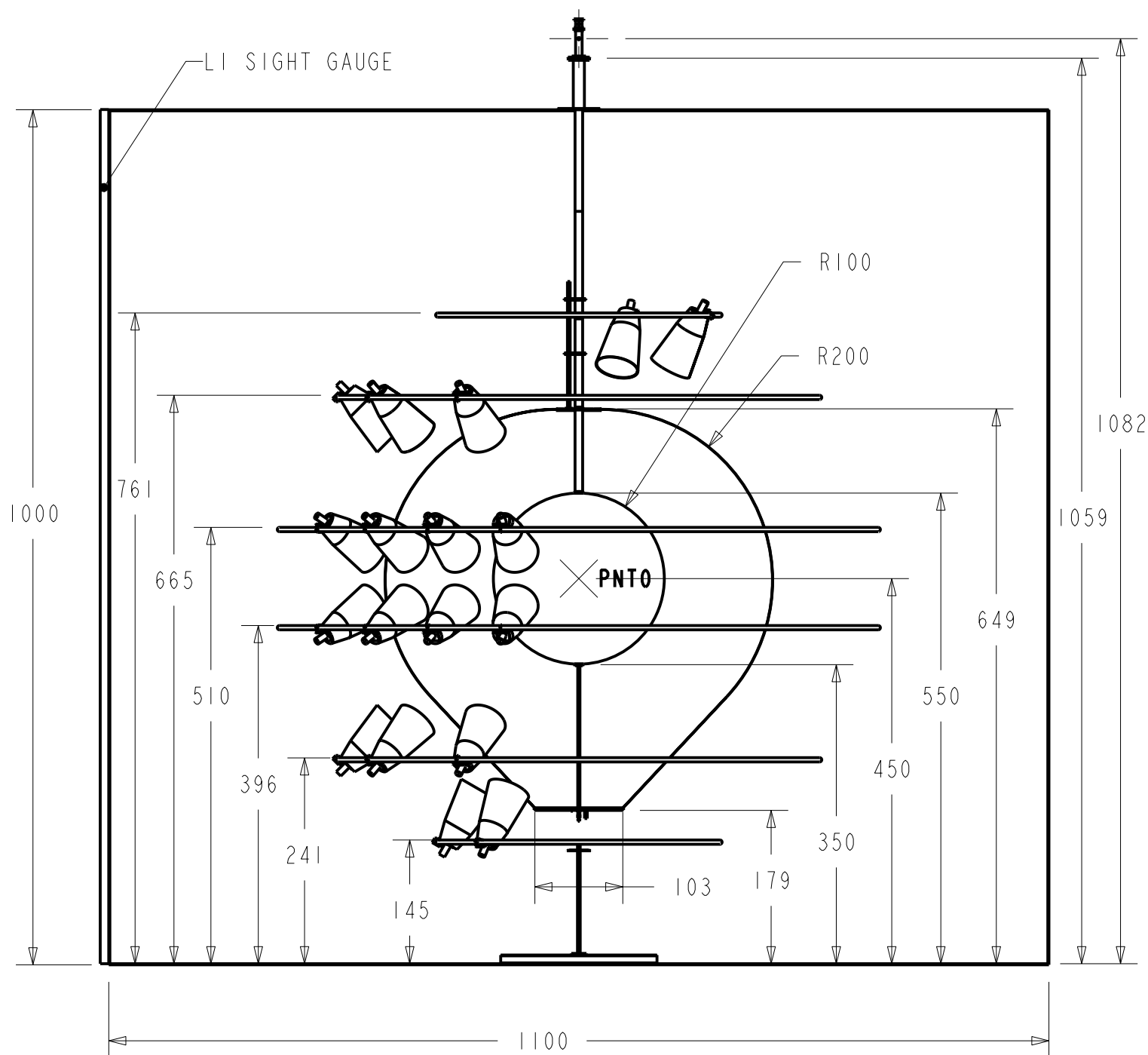
Uranium, Thorium are measured in different samples and are 10^{-14} g/g .

During CTF-1 it was not possible to understand whether the ^{222}Rn level observed as external background was due to a source placed inside the D200 tank like the Permatex layer applied on the walls, or whether the water itself contained a ^{226}Ra contamination. In order to understand the source of the Rn, a campaign of measurements on the water produced from the plant was realized ¹. I report in Tab. 4.3 only two of the many measurements performed. These are sufficient to exclude that radon in CTF-1 water was caused from a high radium level in the water coming from the water system.

4.2.6 CTF-2 Fluid Handling and Purification Systems

The load and unload of the scintillator in CTF-2 is realized from a modular part of the Borexino Liquid Handling system called Module-0 [7]. It is contained inside a building called Big Building East (BBE) in hall C. It is designed for the following operations:

¹The measurements were performed by M. Laubenstein, G. Heusser, W. Rau, H. Singen.



CTF-2 BASIC DIMENSIONS
 ALL DIMENSIONS REFERENCED TO FLOOR OF BLUE TANK
 ALL DIMENSIONS IN CM

	$^{222}\text{Rn} \text{ (Bq/m}^3\text{)}$	$^{226}\text{Ra} \text{ (mBq/m}^3\text{)}$
Sample 1	13.1 ± 0.4	≤ 180
Sample 2	$(3.1 \pm 0.4) \cdot 10^{-3}$	≤ 3

Table 4.3: Radon and radium contents measured in water. Sample 1 was taken from the system in the production mode with a stripping gas rate of $28\text{m}^3/\text{h}$. Sample 2 was taken from the system running in a loop mode concentrated on the 5m^3 tank. The water was stripped and deionized many times.

- volumetric loading and unloading of liquid scintillators to/from CTF IV;
- receiving scintillator from transport tanks;
- fluor mixing;
- batch purification with a solid silica gel column;
- radon degassing of scintillator;
- water extraction in process tank.

All fluid objects like tanks, column and ports are connected to the upper and lower manifold system of Module-0. These are connected by several bridges. The purpose of this organisation is to provide maximal flexibility of flow path. Some of Module-0 performances like stripping efficiency, Rn contamination via part of the connection were tested during the first data taking of CTF-2 with PXE.

4.3 Cleaning and Assembling: the Installation of CTF-2

The cleanliness requirements for CTF are very severe, not only during the preparation of the various parts of the apparatus, but also during the installation phase. For this reason the D200 tank is coupled to a class 100-1000 clean room. During installation the air of the tank is filtered to maintain it at a class of a few thousand. Different procedure of cleaning and preparation of the material are applied.

4.3.1 Cleaning Procedures Applied

The stainless steel housing of the PMTs were passivated and electropolished, then washed in an ultrasound bath, and packed in a plastic bag. The glass bulb of the PMTs was first cleaned with acetone and after each sealing step was inspected in order to remove possible residual of glues before their polymerization. The female connector arrived from the company cleaned and packed in a single plastic bag. The sealing was not realized in a clean room environment but in a mounting room in Hall di Montaggio. Nevertheless we set a standard of cleanliness in order to avoid main sources of dust: all the parts were handled with powder free lattice gloves, removable plastic layer were applied on the working tables, acetone was used to remove any dust observed.

The CTF-1 mu-metal shields were reused after the removal of the acrylic layer that was damaged during water immersion. The acrylic was removed with high pressure vapour. A careful cleaning of the mu-metal surface that presented some black grease probably from the original production was done scratching the surface with a fine metal brush (no sand paper was used because glass remain particulate can contaminate the surface). A standard degreaser was then applied in order to remove the last residual dust and a new layer of acrylic paint was applied. After this treatment of the mu-metal surface possible degradation of the acrylic layer in water should be minimised and cleaning level inside the detector improved.

The assembling parts of the PMTs were cleaned in clean room with clean room solvents.

The new light concentrators were washed in pure water and then stored in clean room. The old one were stored inside the CTF tank. They were then packed in plastic bags and transported in HdM's clean room where we assembled the PMT. After sealing and testing the PMTs all the parts were transported in the HdM's clean room. They were cleaned with the proper clean room solvent and pure water produced from the underground water purification plant. PMT, concentrator and mu-metal were there assembled and all the structure packed in a double plastic bag. All the 100 assembled PMTs were then transported in underground and before the insertion in the D200 clean room the external bag was removed. The internal bag was removed only at the end of the installation.

The cables (56 m long) packed in single bags were cleaned directly in the D200 clean room with clean room solvents.

The D200 tank was inspected and partially cleaned after the dismounting of CTF-1. During all the installation an effort was invested in order to keep the tank as clean as possible and a final cleaning was realized at the end of the installation: the protection floor was removed, the floor of the tank washed with clean water and wiped with clean room wipers. The walls of the tank were inspected and founded clean. Parts of the Permatex layer were found damaged probably due to a wrong deposition of the epoxy resin itself. In order to reduce the deterioration we applied a very thin layer of acrylic paint on the most damaged parts. The roof of the tank was found with some particulates on it. Only a part of the roof was cleaned.

4.3.2 Installation Inside CTF Tank

In order to reach the top of the D200 tank we installed inside an electrical platform. This was first dismounted and washed outside the clean room; then all the parts were cleaned in the D200 clean room and then the platform was installed inside CTF. The first elements installed were the cables. The installation was done passing the cables from the inside of the tank to outside via a feed-through flange. Outside the cables were stretched out on the roof of the tank under a grid and from the D200 tank they passed to the nearby BBW (Big Building West) where the electronic room is placed. Each cable has a label on both ends with a serial number. The number of the cable corresponds to the position of the PMT inside the tank (only in few cases we had to change the association). The installation of the cable took 2 weeks and 4 people.

For the installation of the PMTs a standard scaffold was installed inside the open structure. With the use of a bridge it was possible to reach all the positions on the structure. The PMT was lifted up with a rope still packed in one plastic bag in order to reduce possible scratches on the l.c. surface. It was then fixed to the open structure and connected with its cable. Only at the end of this operation the plastic bag was removed. The PMT fixed to the open structure was then aligned to the center of the IV. The centre of the structure was signed with a little ball (~ 2 cm diameter). A laser mounted on a plexiglass structure was adjusted in the centre of the light concentrator and the PMT was oriented until the laser pointed on the little ball in the centre. After this operation the light fiber used for time calibration was fixed at the light concentrator with a little connector. During the installation electrical tests were performed on the PMTs.

The complete installation took 5 weeks and 4 people.

All the PMTs were installed except the lower ring. This space was left for the IV and the OV installation. A dedicated scaffold was built inside the open structure. First the IV was installed and inflated with nitrogen. During this phase the outside surface of the IV was wrapped with Rn and dust protection layer (Sahran film). The OV built in two parts was partially installed. Two vertical zippers closed it. Just before the conclusion of the installation and after the starting of the nitrogen flowing inside the shroud the Sahran film was removed from the IV. In this way the radon contact from the tank air and the IV surface is minimized.

Only after the completion of this installation the last 8 PMTs were fixed, orientated and connected.

The last 16 muon veto PMTs were installed on the floor of the tank in two concentric rings.

The tank was closed and filled with Nitrogen. A safety valve on the top of the tank guarantees that the over-pressure in the tank is never greater than 10 mbar.

Just before the water filling started we observed the IV collapse. After inspection 3 leaks were found: two of these leaks were 4 cm cracks of the Nylon film, one at 45 degrees from the north pole, the other at 45 degrees from the south pole. The third leak was at a thread in the south pole cap. The leaks were repaired without exposing the inner vessel (significantly) to normal air. The two cracks were repaired by gluing and screwing nylon plates in a sandwich technique around the leak. The leaking thread was sealed again. The two cuts developed in the nylon probably due to the very high dryness of the nitrogen atmosphere. The nylon in this condition becomes very brittle and can develop creaks. In these conditions it was decided to proceed with a water filling test and a data taking with PXE in order to conclude the optical study of this scintillator and in the same time characterize the detector. For the most stressful PC campaign it was decided to produce a new set of vessels to be installed after the completion of these preliminary measurements.

4.4 Water Filling and Water Data Taking

After the filling of the tank with nitrogen the tank and the two vessels were filled with ultra-pure water. A new water filling system with respect to CTF-1 was installed because of the change of the vessel design. The technical design is reported in

Fig. 4.9, [21].

The filling procedure applied can be summarized in the following steps [21]:

- 0- *Initial conditions*: D200 tank is full of nitrogen with an overpressure respect to the ambient pressure in hall C of 10 cm. The IV and the OV are inflated with nitrogen. The water production plan is running for different days in order to give performances at equilibrium with a maximum flux of $2m^3/h$. The nitrogen plant is working, the nitrogen storage tanks are full and the supply pressure is 10 bar.
- 1- *Approach to the south pole of the shroud*: water is inserted only in the D200 tank with a flux of $2m^3/h$. This means that the water level in the tank will rise about 2 cm/h. Every two hours we record some data about the system: level of the water in the tank, in the outer vessel and in the IV, flow rates, water temperature, water resistivity, nitrogen flux used for the stripping, IV gas pressure, OV gas pressure. The water level in the D200 is measured via a sight gauge. We stop 5 cm below the OV south pole.
- 2- *Crossing the OV south pole*: a water filling schedule for the first 25cm of the OV is worked out evaluating the volume to be filled in the OV and in the tank. The two volumes are filled separately in order to avoid overfilling or underfilling of the OV. The OV volume is not defined due to the fact that it is a flexible membrane. For this reason the evaluation of the volume to be filled is made thinking of an imaginary column of 1m diameter. The sight gauge of the D200 tells us the level in the tank and an inverted U-tube tells us the differential pressure from the OV and the tank. An overhead gas pressure on the OV between 1 and 2 mm is maintained.
- 3- *Approach to south pole of the Inner Vessel*: the filling continue alternating the filling of the OV volume and the D200 volume separately. We stop 5 cm below the IV. An underwater videocamera equipped with a light gives a visual image of the water filling.
- 4- *Filling the IV*: the IV must be filled in a way that preserves its shape. It cannot be under- or overfilled. The level difference between the IV and the tank is monitored measuring the boyance force with the strain gauge ($\sim 5kg$) or measuring the relative water column heights with an inverted U-tube. The IV is

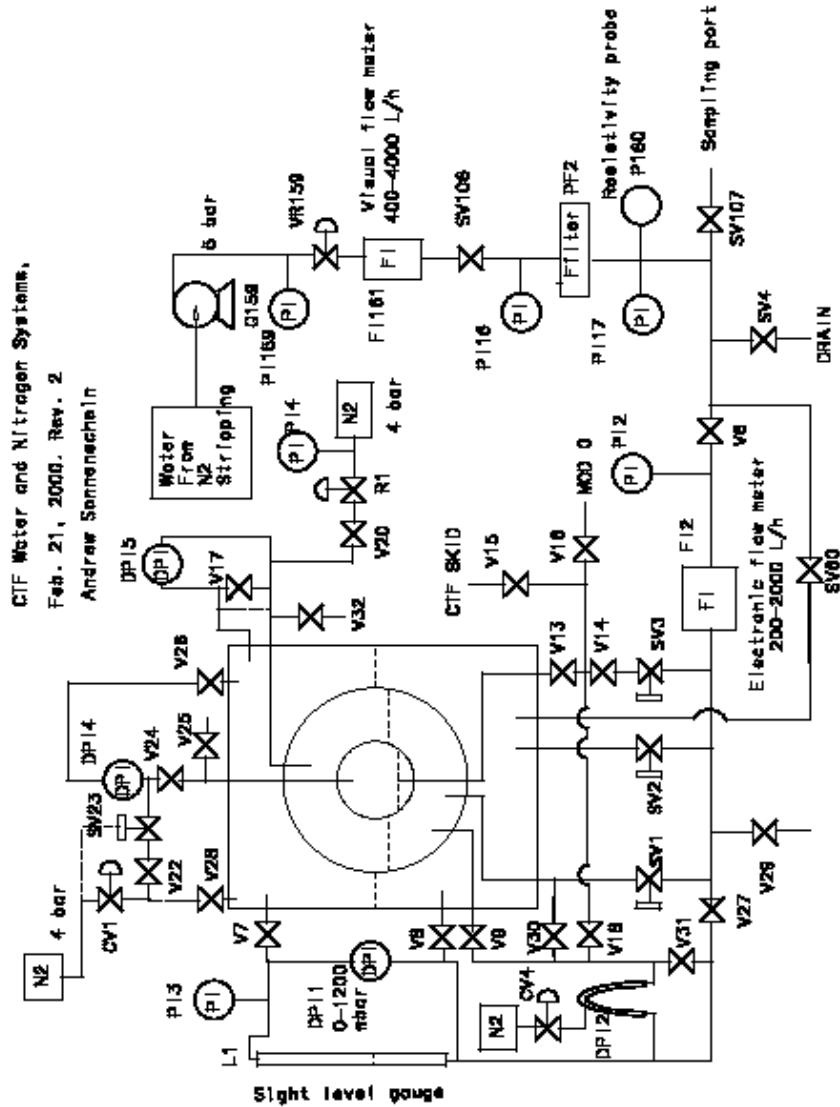


Figure 4.9: Technical design of CTF-2 water and nitrogen system. The volumes to be filled are three: the IV, the radon barrer and the tank. Only one volume per time is partially filled.

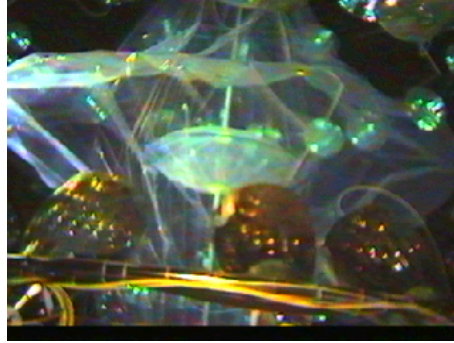


Figure 4.10: CTF-2 during water filling. The IV is just visible in the center of the picture.

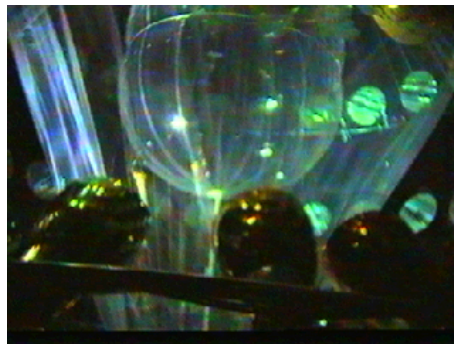


Figure 4.11: CTF-2 during water filling. The equator of the IV is passed. Reflections on the surface (the light comes from the bottom) are now reduced.

filled at 100 l/h rate and constantly controlled via the underwater videocamera (see Fig. 4.10, Fig. 4.11, Fig. 4.12).

- 5 *Filling to the top of the tank:* after the completion of the OV we proceed with the filling of the last part of the tank. Air trapped on the top of the OV creates some problems solved depressurizing the OV and concluding the filling of the OV in a very slow way.

4.4.1 Start Data Taking: Čerenkov Event Identification

When the D200 tank was completely filled with water as the IV and the OV, the data taking started. The event parameters measured in CTF are:

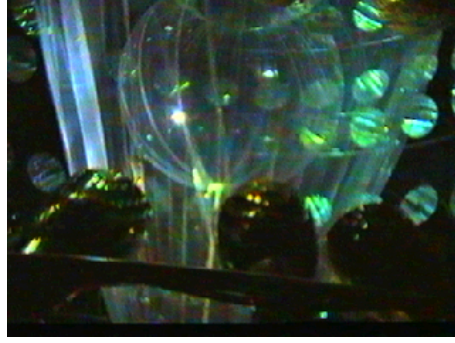


Figure 4.12: CTF-2 during water filling. The filling is completed.

- total charge collected by the PMTs (calorimetric measurement);
- arrival time of the photons on the PMTs (spatial reconstruction);
- pulse shape (α/β discrimination);
- time elapsed between sequential events (tag time correlated events).

The number of hit channels versus the number of photoelectrons was evaluated via a simulation using the probability relation between these two variables. From this comparison and from a similar one made on the data we extracted the photon-electron yield.

The through-going muons penetrating the rock overborde and γ -rays from radon in the water produce Čerenkov radiation. The total energy spectrum detected with CTF-2 is reported in Fig. 4.14. Čerenkov light produced by γ -rays interests the part of the energy spectrum less than 20-30 photoelectrons ². The two components show different mean arrival time of the photons and light distribution. The mean arrival time distributions is in Fig. 4.15. The light detected by the tubes is disuniform for the muons which mainly come from the top but uniform for the gamma as shown in Fig. 4.16. The comparison with the similar distribution for the scintillator events gives us an efficient way to disentangle Čerenkov events from scintillating events. Čerenkov light is rejected from scintillation light applying the following cuts:

²The number of photoelectrons is the sum of each ADC signal after the pedestal subtraction and the division by 50. The calibration with laser sets the single photoelectron peak at ch50 of each ADC.

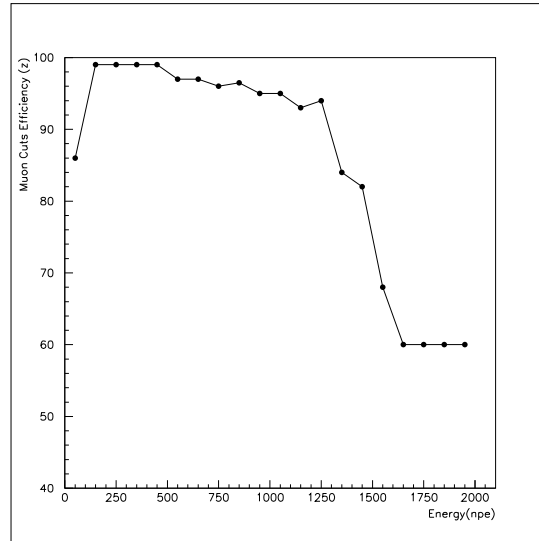


Figure 4.13: Energy dependence of the efficiency of the cuts applied on Čerenkov events.

- CUT 1: Mean Arrival Time of the photons lower than 16 nsec (the arrival time of Čerenkov events is higher);
- CUT 2: Ratio of the light collected from the upper hemisphere and the total greater than 0.4 (Čerenkov light comes mainly from the top of the tank).

The energy dependence of the cuts efficiency is reported in Fig. 4.13. In the neutrino window the efficiency is $\sim 99\%$ but at higher energy decreases.

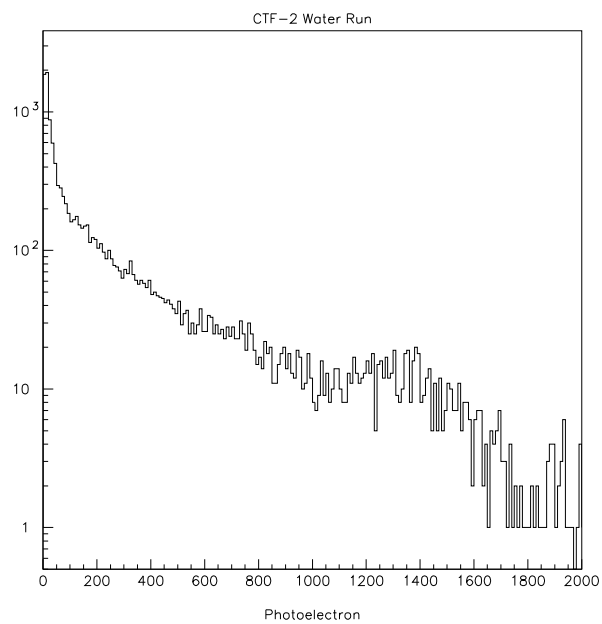


Figure 4.14: Energy spectra of the Čerenkov radiation detected in CTF-2.

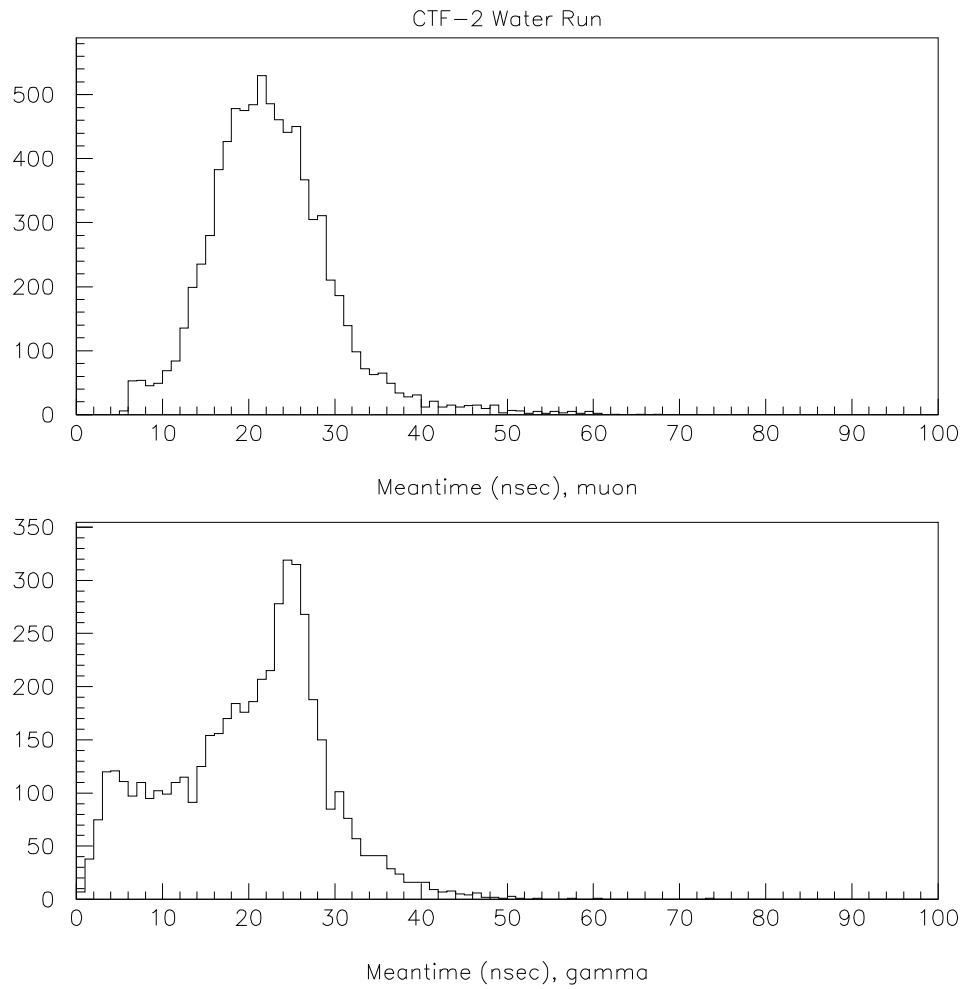


Figure 4.15: Photon arrival time distribution for the two components of Čerenkov radiation. The upper plot concerns the energy region greater than 20 pe and the lower concerns the energy region less than 20 pe.

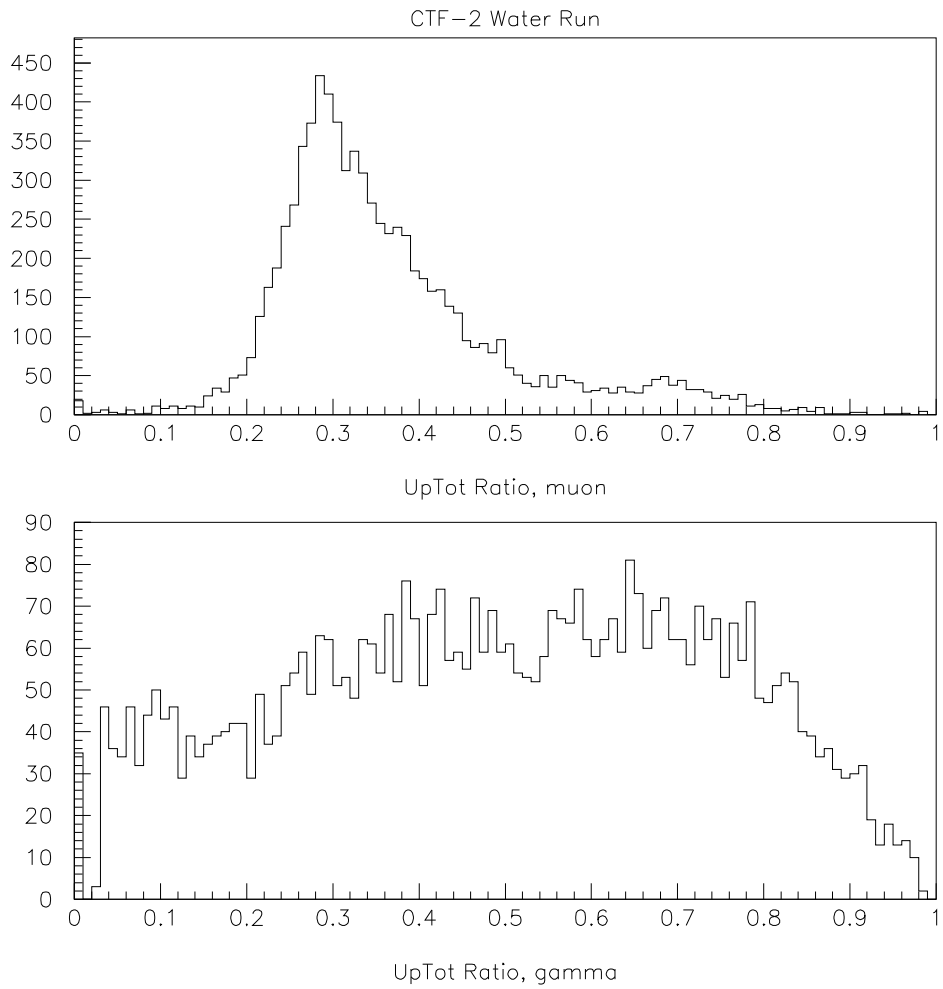


Figure 4.16: Fraction of the light detected by the tubes of the upper hemisphere over the total. The muons give a disuniform distribution because they come mainly from the top.

Bibliography

- [1] Borexino Coll., NIM A406, (1998) 411.
- [2] M. Balata et al, NIM A370 (1996) 605.
- [3] M. Giammarchi et al., Ultrapure Water Journal 13 (1995) 59.
- [4] M. Laubenstein et al., NIM A409 (1998) 484.
- [5] T. Goldbrunnert, *J. Radioanalytical and Nuclear Chemistry* 216(2) (1997) 293.
- [6] <http://www.e15.physik.tu-muenchen.de/borexino/memo.htm>
- [7] S. Schönert, K.-H. Schuhbeck, *A Liquid Handling and Purification Module for CTF and Borexino*, Borexino Internal Report 99-04-01.
- [8] J. Benziger et al., NIM A417 (1998) 278.
- [9] F. Hartmann et al., to be submitted.
- [10] T. Hagner et al., to be submitted.
- [11] Borexino Coll., *Phys. Lett. B* 422 (1998) 349.
- [12] Borexino Coll., *Astrop. Phys.* 8 (1998) 141.
- [13] Borexino Coll., NIM A440 (2000) 360.
- [14] C. Galbiati, Tesi di Dottorato, Univ. degli Studi di Milano, (1999).
- [15] M. Deutsch et al., Borexino coll., “Proposal to NSF” (1996); L. Oberauer and S. Schönert, Proc. of the IVth SFB-375 Ringberg Workshop, “Neutrino Astrophysics” (1997) 33-36; M. Chen et al., Borexino Coll., “Proposal to NSF” (1998).

- [16] C. Arpesella, *Appl. Radiation. Isot* Vol. 47 No. 9/10, pp.991-996, 1996.
- [17] W. Rau, G. Heusser, *Appl. Radiation. Isot* 53 (2000) 371-375.
- [18] J.X. Prochaska, *The design and fabrication of optimal light collectors for the CTF*, Thesis, Princeton University (1993).
- [19] P. Lombardi, Tesi di Laurea, Politecnico di Milano (1997).
- [20] G. Ranucci, A. Goretti, P. Lombardi, *NIM A* 412 (1998) 374-386.
- [21] A. Sonnenschein, private communication.

PXE Characterisation in CTF-2

The results obtained from CTF-1 PXE test (October '96 - July '97) left open various questions concerning the optical behaviour of the scintillator studied. The very low α/β discrimination capability observed in CTF was not understood. On laboratory samples PXE shows an α identification efficiency similar to the one measured on PC samples as reported in Tab. 5.1. In order to complete the PXE study, a PXE test was realized. It was mainly devoted to the study of the α/β discrimination capability. Important information about internal and surface background and the study of the performances of part of the Borexino liquid handling were also obtained during this test.

For the filling operations a sub-system of the Borexino liquid handling (Module-0) was used.

The PXE tested in CTF-1 was stored in underground in one of the EP-tank of Module-0. It was used again for the new test in CTF-2. The scintillator cocktail used was PXE + tp (2.0 g/l) + bisMSB (20mg/l).

The filling of the total volume of PXE (4 tons) was realized in three different steps:

- *First Filling:* the first scintillator operation represents the start up of the Module-0 liquid handling and purification system. Moreover, questions concerning the tightness of the IV pushed us to use only $\sim 1m^3$ (912 Kg) of PXE for the first filling. The operation was realized on the 3rd of June 2000. The data taking started on the 4th. The run number is from 717 to 723.
- *Second Filling:* additional $\sim 2m^3$ were inserted in the IV on the 11th of June 2000. The total scintillator mass in the IV was then 3132 Kg. The run numbers that concern this data taking are 724 - 757.

- *Third Filling*: the remaining amount of PXE was inserted on the 15th of July 2000. The run concerning this data taking goes from 758 to 788.

At the end of the data taking with PXE was performed a calibration of the detector with radon sources. The source was placed along and off z axis. The main goal of this type of calibration is the study of the spatial reconstruction code response and it is typically done at the end of a data taking in order to avoid possible contamination problems. The runs that concern the calibration are 791 - 810.

I will discuss separately the data analysis realized after the first two fillings together and after the last filling separately. For the calibration results I will refer to [10].

Sample	Energy Region (pe)	β identification	α identification
PXE+tp+bisMSB	48-70	98%	79.2 %
	80-135	98%	98.84 %
PC+PPO	48-70	98%	85.8 %
	80-135	98%	99.7 %

Table 5.1: α/β discrimination capability measured on laboratory samples. The value is calculated using the ratio of the integrated charge after 25 nsec and the total charge [4].

Element	Energy (MeV)	Quenched Energy in PXE+tp+bisMSB (KeV)
^{222}Rn	5.49	530 ± 8
^{218}Po	6.02	622 ± 8
^{214}Po	7.69	961 ± 9

Table 5.2: α quenching in PXE+tp+bisMSB [1].

5.1 First and Second Partial Fillings

The scintillator before the filling is prepared in the following way: it passes through a silica gel column in order to remove ionic impurities and particulates. Then, the

Element	CTF-2 silica gel (Bq/kg)	CTF-1 silica gel
^{238}U	2.7 ± 0.5	1.6 ± 0.3
^{226}Ra	3.8 ± 0.2	2.28 ± 0.11
^{210}Pb	2.6 ± 0.5	1.6 ± 0.3
^{228}Ra	3.2 ± 0.3	1.4 ± 0.1
^{228}Th	2.2 ± 0.2	1.4 ± 0.1
^{40}K	≤ 2.1	1.9 ± 0.4

Table 5.3: Silica gel radioactive contamination used in CTF-2 and in CTF-1.

gaseous impurities present in PXE or passed from the silica gel to the scintillator¹ are removed with an unknown efficiency using a strong nitrogen flux. Normal nitrogen is used during the first stripping period and only at the end ultra-pure nitrogen is applied.

The filling was realized via a volumetric exchange in a closed loop with the water contained in the IV. The details and the safety aspects of the filling operation are reported in [6]. At the time of the first filling the second electronic chain was not yet optimized so the data analysis of this period cannot be completed. Nevertheless, the raw data on group 1 show good general performances of the detector (see Fig. 5.1, Fig. 5.2).

The scintillator for the second filling was prepared with small differences with respect to the first filling and was filled following the same procedure.

During the second period of data taking the electronics was completed set up so different information can be extracted. Some of the arguments that can be analysed are:

- i) Radon level introduced during filling.
- ii) On-line energy calibration.
- iii) Čerenkov events discrimination.
- iv) Abundance of ^{14}C in the scintillator.

¹The radioactive contamination of the silica gel used is reported in Tab. 5.3. The radon emanation rate is $\sim 170\text{mBq/kg}$ as was measured during the PXE test in CTF-1 [5].

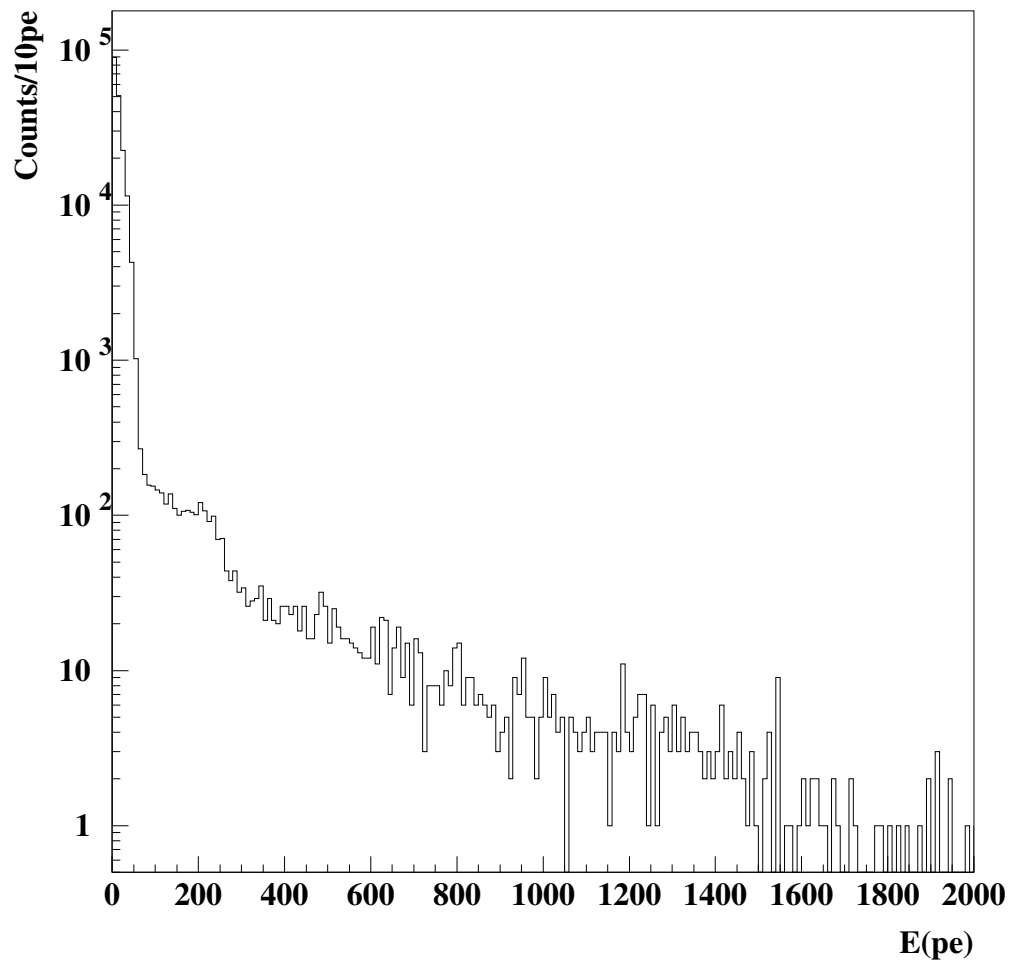


Figure 5.1: Group 1 raw events for $1m^3$ of PXE. In the region less than 100 photoelectrons (pe) ^{14}C dominates the count rate. A peak is visible at ~ 200 pe that indicates ^{222}Rn presence.

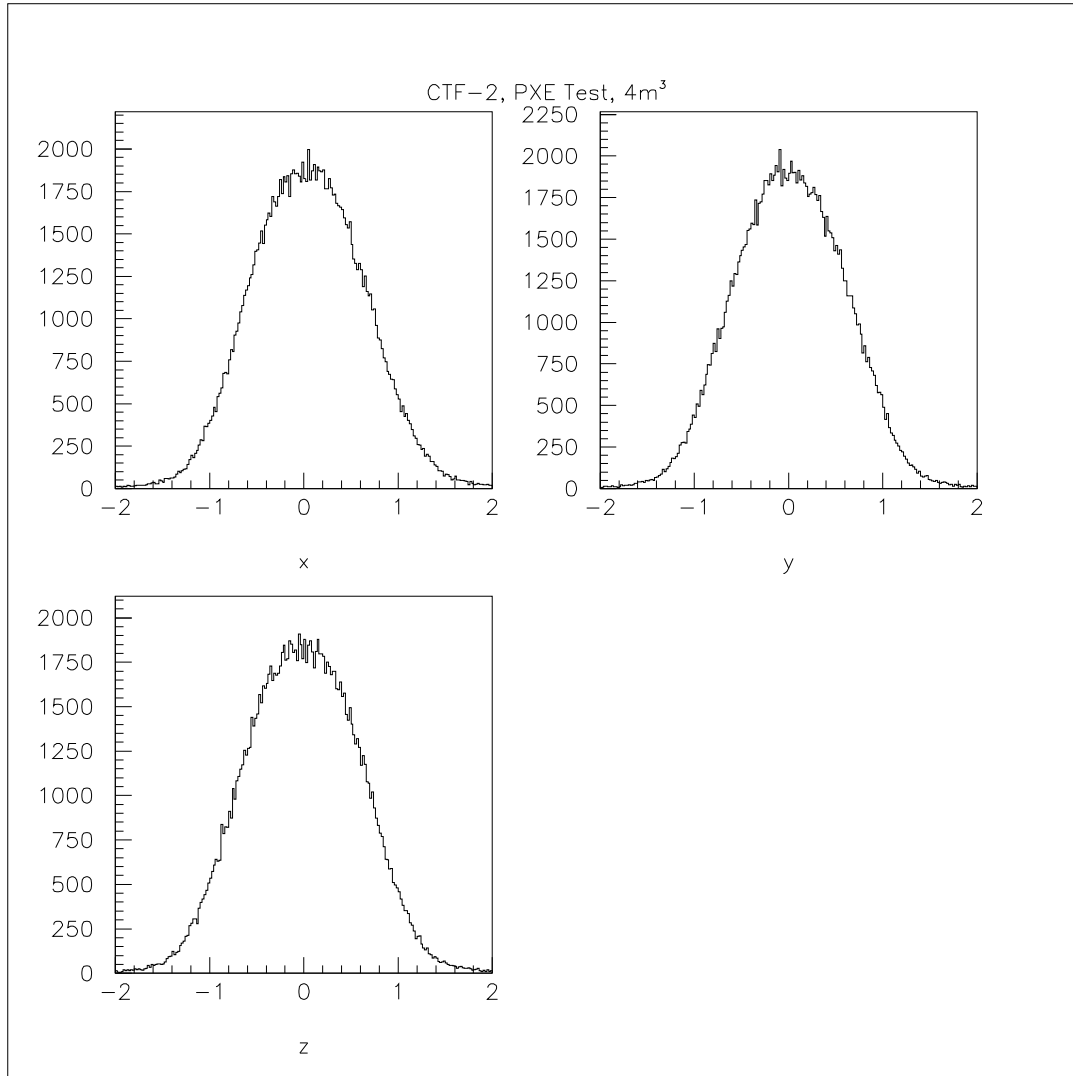


Figure 5.2: x, y, z distributions for the reconstructed events with $1m^3$ of PXE. It is evident the asymmetry in z indicating that the scintillator is on the higher part of the IV.

5.1.1 Radon Level Inserted During Fillings

Radon introduced during filling operations can limit low background measurements for long time. Moreover, the build up of radon daughters ^{210}Bi and ^{210}Po is a dangerous source of background in CTF and Borexino. For these reasons a particular effort is devoted to the realization of “radon free” fillings.

For the first filling we can study only group 1 events. Radon contamination can be detected in CTF not only via group 2 chain that is dedicated to this purpose but also studying group 1 events. α decay of ^{222}Rn and ^{218}Po should appear forming a pronounced peak around 200 pe in the energy spectrum of group 1 (Fig. 5.1). This spectrum shows the presence of a peak around the energy region of interest. This indicate that during the first filling some radon was inserted. Via a comparison with the analogue spectra obtained after the second filling, where the second electronic chain was working, we can set an upper limit of ~ 50 counts/day of ^{222}Rn . This limit is very encouraging and represent the first filling operation without a high radon contamination.

The total amount of radon inserted during the second filling is higher than during the first and corresponds to ~ 840 counts/day including the remaining radon counts from the first filling (less than 10 counts/day). Possible variations of the stripping time or the use of both buffer tanks can be the reason of the different performance obtained. In Fig. 5.3 is reported the comparison between the group 1 energy spectrum immediately after the filling and the group 1 energy spectrum after 2 weeks of data taking. Both spectra are normalised in counts/hour. It is visible the decreasing of ^{222}Rn - ^{218}Po peak at $\sim 200\text{pe}$.

5.1.2 Energy Calibration

A first estimation of energy calibration can be evaluated directly from the data even without the use of dedicated sources. The α peak of ^{214}Po (Fig. 5.4) visible on the group 2 chain and the α peak of ^{222}Rn and ^{218}Po visible on the group 1 (Fig. 5.3) are the main “internal sources” useful for the energy calibration. The quenched energy in PXE for the α ’s coming from ^{222}Rn is reported in Tab. 5.2. Moreover, at lower energies the ^{14}C spectrum can be used as a check of the linearity of the calibration. The energy calibration calculated using the α mentioned before corresponds to:

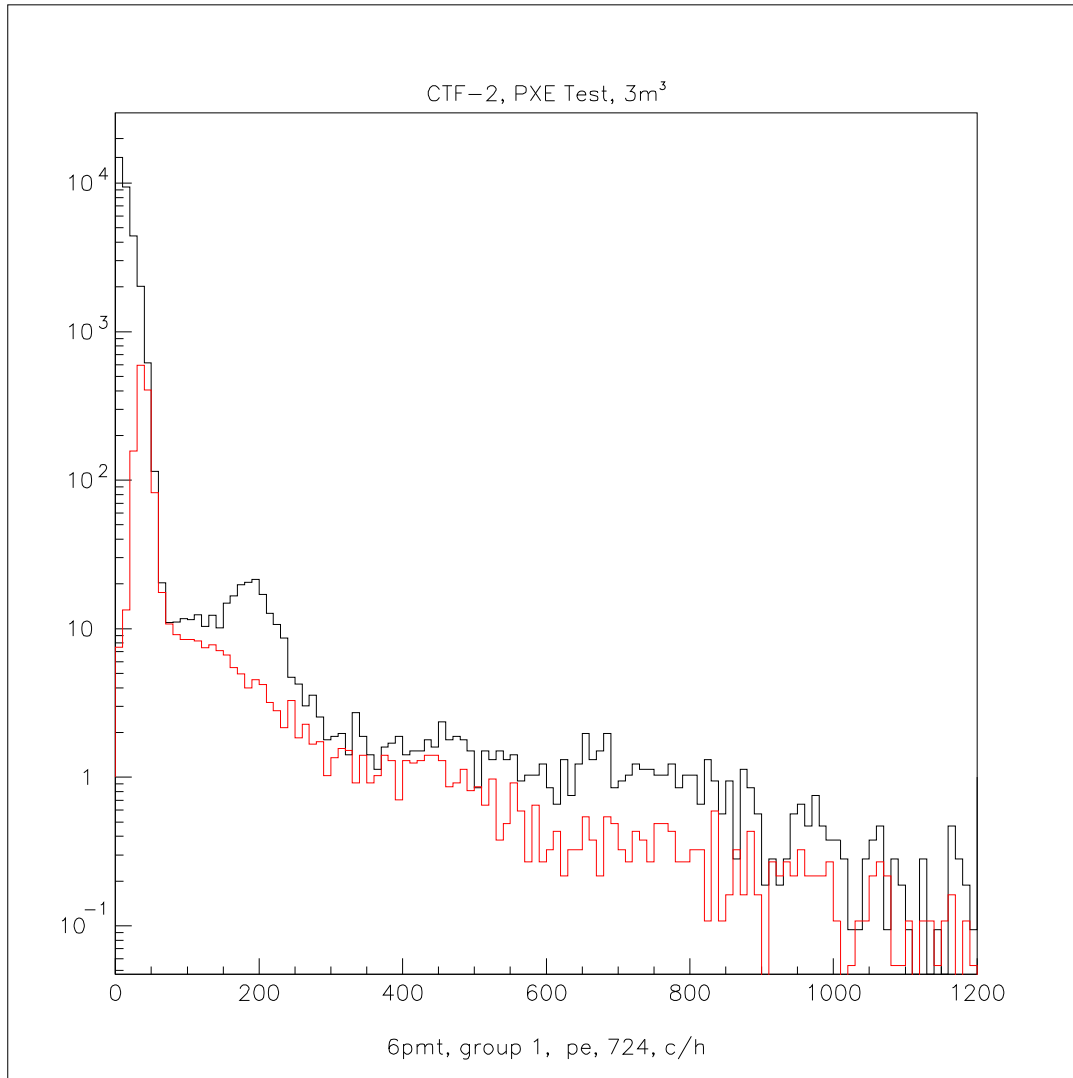


Figure 5.3: Group 1 events (counts per hour) for the first run after the second filling (black) and a run after 2 weeks of data taking (red). It is visible in the black plot the α peak of ^{222}Rn and ^{218}Po around 200 photoelectrons.

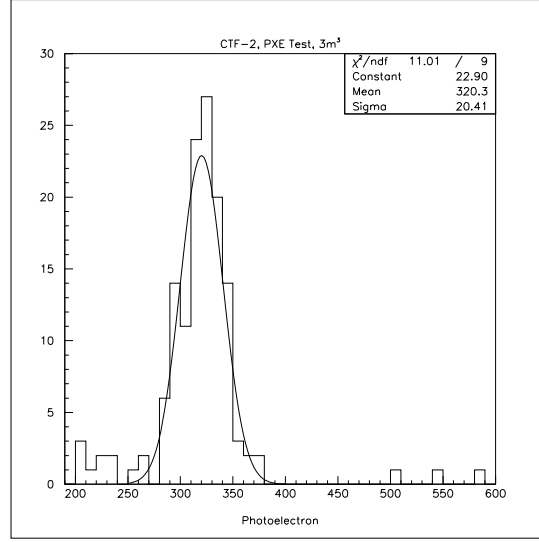


Figure 5.4: ^{214}Po peak on the group 2 chain for 3m^3 PXE. From the energy fit we can extrapolate the first estimation of the energy calibration.

$$Q/E = 330 \pm 20 \text{ pe/MeV} \quad (5.1)$$

The energy resolution is $\sigma \sim 7\%$ at the energy of the ^{214}Po α and is supposed to scale with energy as $1/\sqrt{N}$ (N =number of photoelectrons). A confirmation of the calibration at higher energy comes from an unexpected peak visible at ~ 400 pe that can correspond to the ^{40}K γ emission. This contamination is analyzed in the next section where the filling is completed.

5.1.3 Čerenkov Events Identification

In Borexino a dedicated muon veto system will reject muon events with a design efficiency of 99.9999%. In CTF-2 a cluster of 16 PMTs was installed on the floor of the CTF tank in order to function as muon veto. At the time of the data taking the system was not yet optimised. Nevertheless, the discrimination of Čerenkov events produced from through-going muons in the water buffer from the scintillation events can be realized on the base of the following considerations:

- the distributions of the photon arrival time for Čerenkov events and for scintillation events are very different (see Fig. 5.5, Fig. 4.15 and Fig. 4.16);
- the spatial distribution of the Čerenkov light produced by the through-going muons that pass in the water buffer is not uniform. Due to the directionality of the incoming muon flux more light is detected by the bottom hemisphere PMTs than by the top PMTs. In contrast, scintillation events emit isotropically.

Just using these parameters we can reject most of the Čerenkov events. Requesting that the mean arrival time of the photons is lower than 16 nsec and the ratio of the light collected from the upper hemisphere and the total light collected is greater than 0.4 we reject most of the muons. The efficiency of these cuts are discussed in the previous chapter.

5.1.4 Abundance of ^{14}C

The total event rate in CTF-2 for the run 724 - 740 (6.4 days, 153 hours) is 5.75 Hz (6 PMTs in trigger, $3m^3$ PXE). The dead time measured is 75 msec. This corresponds to $\sim 43\%$ of the total time of data taking. Scaling the event rate for the dead time we have that the dead time corrected events in CTF-2 is ~ 13 Hz. Due to the high dead time the energy threshold is increased progressively from 6 PMTs till 21 PMTs after the run 740. The raw data are fitted, as in [2], with the function:

$$S(W_e) = \int N(W'_e) g(W'_e, W_e) dW'_e + B(W_e) \quad (5.2)$$

where $N(W'_e)$ is the theoretical β spectrum, $g(W'_e, W_e)$ is the detector response function and $B(W_e)$ is a polynomial which accounts for the background contribution. The theoretical β spectrum has the form:

$$N(W_e)dW_e = p_e W_e (W_0 - W_e)^2 F(Z, W_e) C(W_e) dW_e \quad (5.3)$$

where p_e , W_e are the momentum and total energy of the emitted electron, W_0 is the end-point, $F(Z, W_e)$ is the Fermi function (for the influence of the nuclear Coulomb field), and $C(W_e)$ is the “shape factor” [3]:

$$C(W_e) = 1 - (0.37 \pm 0.04)W_e \quad (5.4)$$

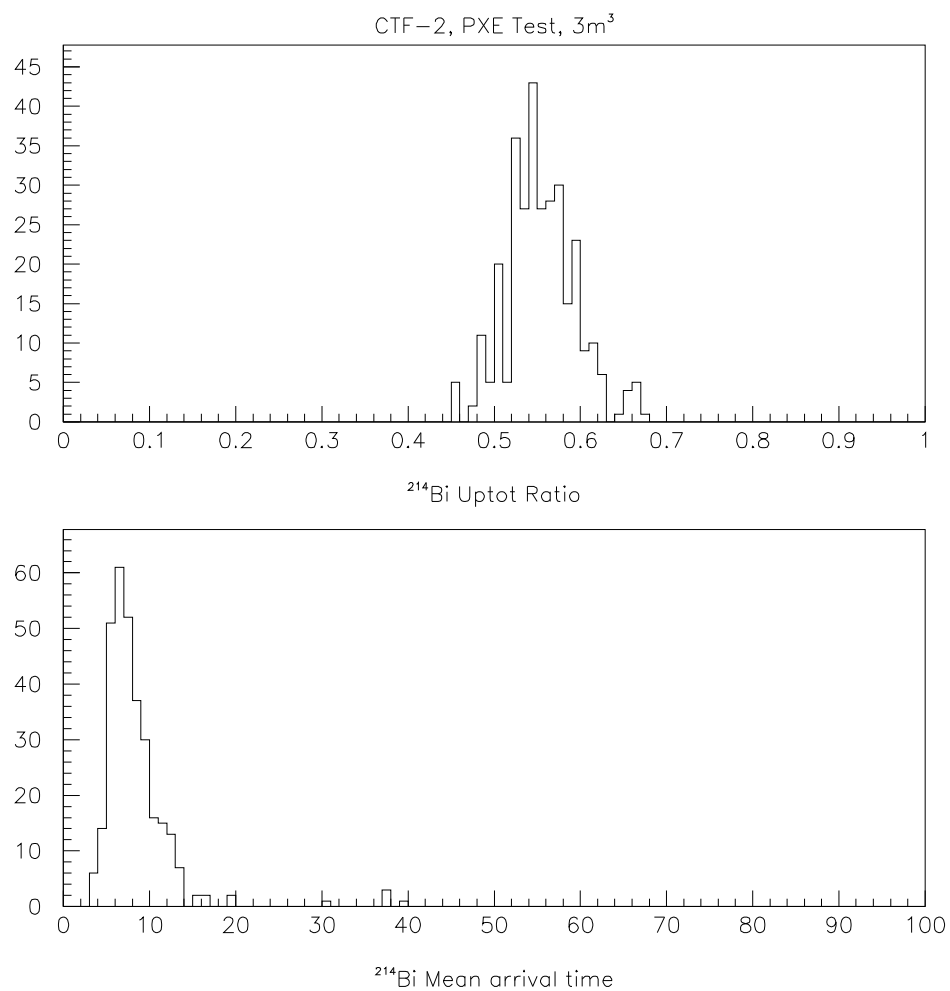


Figure 5.5: Light collected from the upper hemisphere vs the total light collected and mean arrival time of the photons for ^{214}Bi events in nsec.

Using ^{214}Po α distribution it is known that $g(W'_e, W_e)$ has a Gaussian shape. Its σ depends on the energy and scales approximately with its square root.

$B(W_e)$ is parameterized as first order polynomial. It is fitted in the region above the ^{14}C energy range 75-200 pe and the polynomial obtained is: $0.009651x+18.55$ (x is in units of photoelectrons). The background is then fixed during minimisation process.

The total PXE mass is $m=3132$ kg. The entire data taking considered lasted $T=153$ hours. The results of the fitting procedure are:

- P(1) = overall normalisation factor that corresponds to the ^{14}C activity.
 $P(1) = 2035400 \pm 4418$ counts/T.
 The activity A in Bq recorrect for the dead time is:

$$A(Bq) = \frac{P(1)}{T(sec) \cdot \epsilon_{dead}} = 6.47 \pm 0.01 Bq. \quad (5.5)$$

- P(2) = energy calibration. The result obtained is:

$$Q/E = 311.0 \pm 0.3 pe/MeV. \quad (5.6)$$

where Q is the measured photomultiplier charge in units of photoelectrons. This result is in very good agreement with the energy calibration obtained in 5.1 giving however a higher precision.

- P(3) = energy resolution. The result obtained is:

$$\sigma(E)/\sqrt{(E)}(keV^{-1}) = 2.50 \pm 0.01 keV^{1/2} \quad (5.7)$$

The $^{14}\text{C}/^{12}\text{C}$ ratio is given by

$$^{14}\text{C}/^{12}\text{C} = A \frac{\tau M}{16 N_A m} = (11.74 \pm 0.03) \cdot 10^{-18} \quad (5.8)$$

where A is the activity in Bq, M is the molar weight of the PXE molecule ($C_{16}H_{18}$), N_A is the Avogadro number. The comparison with the results obtained in CTF-1 with PC sample is reported in Tab. 5.4 together with the results obtained with PXE. The fitted spectrum is in Fig. 5.6.

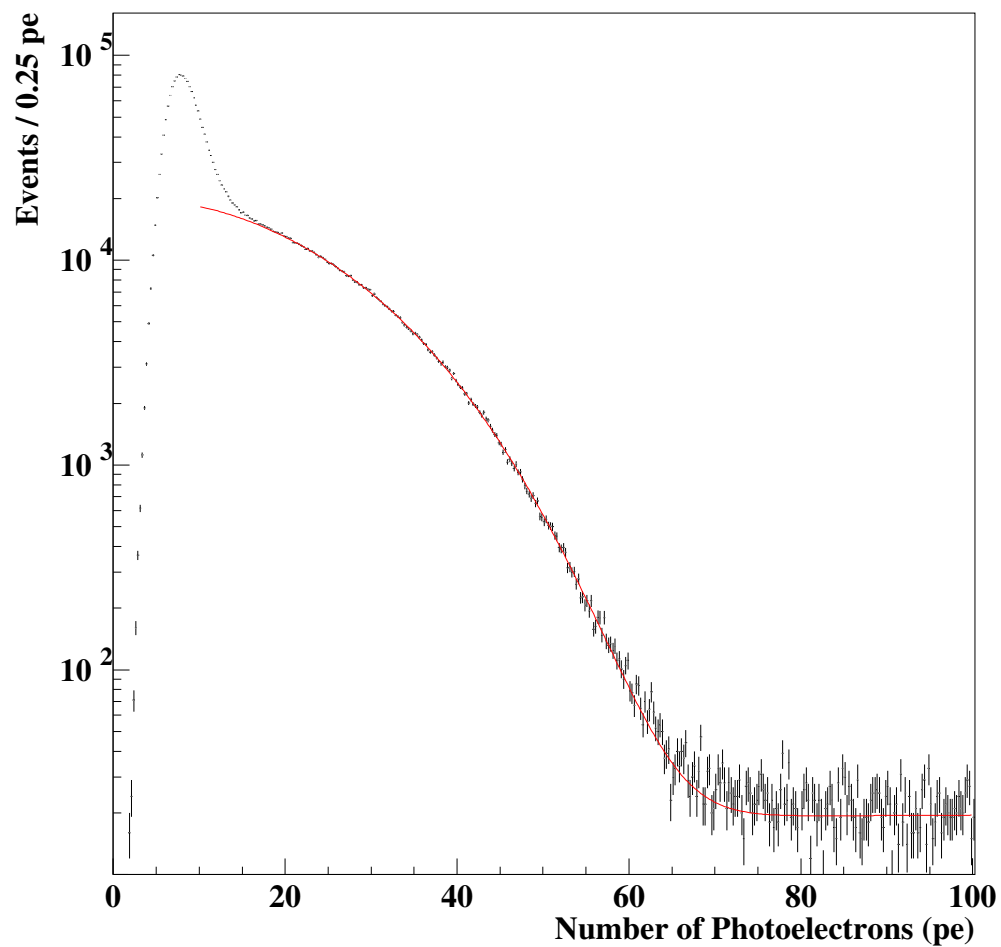


Figure 5.6: Data and fit of PXE in CTF-2. The bin width is 0.25 pe and the collection period is 153 hours.

	PC in CTF-1 [2]	PXE in CTF-2
Data Collection Time [d]	13.6	6.4
χ^2/ndf	236/201	204/196
^{14}C activity [Bq]	1.425	6.47
Detector Mass [tons]	4.24 ± 0.21	3.132
$\sigma(E)\sqrt{(E)}[keV^{-1}]$	2.88 ± 0.01	2.502 ± 0.0134
$Q/E[MeV^{-1}]$	273 ± 0.1	311 ± 0.3
Ratio $^{14}\text{C}/^{12}\text{C}[10^{-18}]$	$1.94 \pm 0.01 \pm 0.09$	11.74 ± 0.03

Table 5.4: Results obtained from fitting the low energy CTF-1 data with PC scintillator and CTF-2 data with PXE.

5.2 Completion of the Filling

The preparation of the scintillator and the filling operation for the third filling were realized in an analog way as for the previous fillings. Several issues which characterize the detector performances and radioactive background during this period have been analyzed:

- i) Radon level introduced during filling;
- ii) α/β discrimination efficiency;
- iii) ^{40}K contamination;
- iv) Limit of ^{238}U contents in PXE.

5.2.1 Radon Inserted During Filling

The radon level after completion of the third filling corresponds to a total of ~ 90 counts/day. About ~ 30 counts/day were still present from the previous filling. The energy spectrum of ^{214}Po peak is in Fig. 5.7.

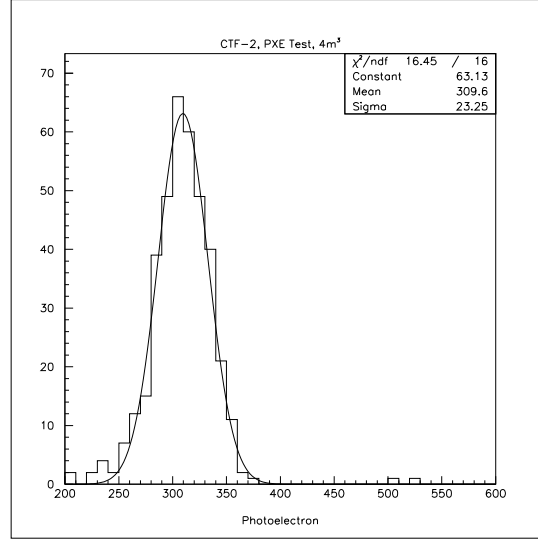


Figure 5.7: ^{214}Po peak on the group 2 chain for $4m^3$ PXE.

5.2.2 α/β Discrimination Efficiency of PXE

The pulse shape of the scintillation light induced by α and β particles is derived experimentally through the application of the so called “single-photon sampling technique”. The pulse shape discrimination (PSD) is carried out through the charge integration technique. This method consists in measuring both the total charge collected from the PMTs and the charge in the tail. The tail to total ratio is then the separation parameter used [8].

The data samples analyzed are:

- α from ^{214}Po : the electronic group selected is the second, the energy region is from 250 pe to 380 pe (97.88% efficiency) and the coincidence time is from 50 μsec to 1000 μsec (82.5% efficiency).
- β from ^{214}Bi (Energy ≥ 150 pe): is selected as the event that precedes the ^{214}Po decay with energy greater than 150 pe.

The energy spectrum of the two clusters of events is in Fig. 5.8. Two tail/total charge ratios are evaluated: R32 that corresponds to the 32 nsec tail and R48 that

corresponds to the 48 nsec tail. The different distributions of the ratios are fitted with a Gaussian distribution. In order to evaluate the discrimination efficiency I fixed the β identification efficiency at 98% and calculated the corresponding identification efficiency of α events. The scatter plots (Fig 5.9) show intuitively the discrimination capability of the two samples of events.

A radial analyses is then applied ². The results are summarised in Tab. 5.5. We have to underline that the spatial distribution of the ^{214}Po alphas is not uniform. We observed that the decay time of ^{222}Rn was longer than expected. The spatial distribution of radon events in the last runs, when the radon level was constant (~ 20 counts/day), reveals a disuniform distribution that suggests the presence of an internal source (Fig. 5.10). A dedicated analysis of this cluster of events is reported later in the context with the $^{238}\text{U}_{eq}$ estimation.

$r(m) \leq$	R32 μ_α	R32 σ_α	R32 μ_β	R32 σ_β	R32 α ident %	R48 α ident (%)
-	0.50	0.036	0.34	0.044	90.5	64.8
0.9	0.49	0.030	0.33	0.038	97.7	68.3
0.8	0.48	0.026	0.32	0.030	99.9	89.0
0.7	0.48	0.026	0.31	0.022	99.9	89.3
0.6	0.48	0.026	0.31	0.022	99.9	89.3

Table 5.5: Radial analysis of α/β discrimination capability. In correspondence of the two tail/total charge ratios are reported the mean value (μ) and the standard deviation (σ) of the fitted distribution. Setting a 98% efficiency of identification of β events I calculated the identification percentage of the α events. The ratio R32 is superior to R48. Increasing the radial cut the efficiency as expected increases.

²The decision to use the spatial reconstruction code comes only after the source calibration runs.

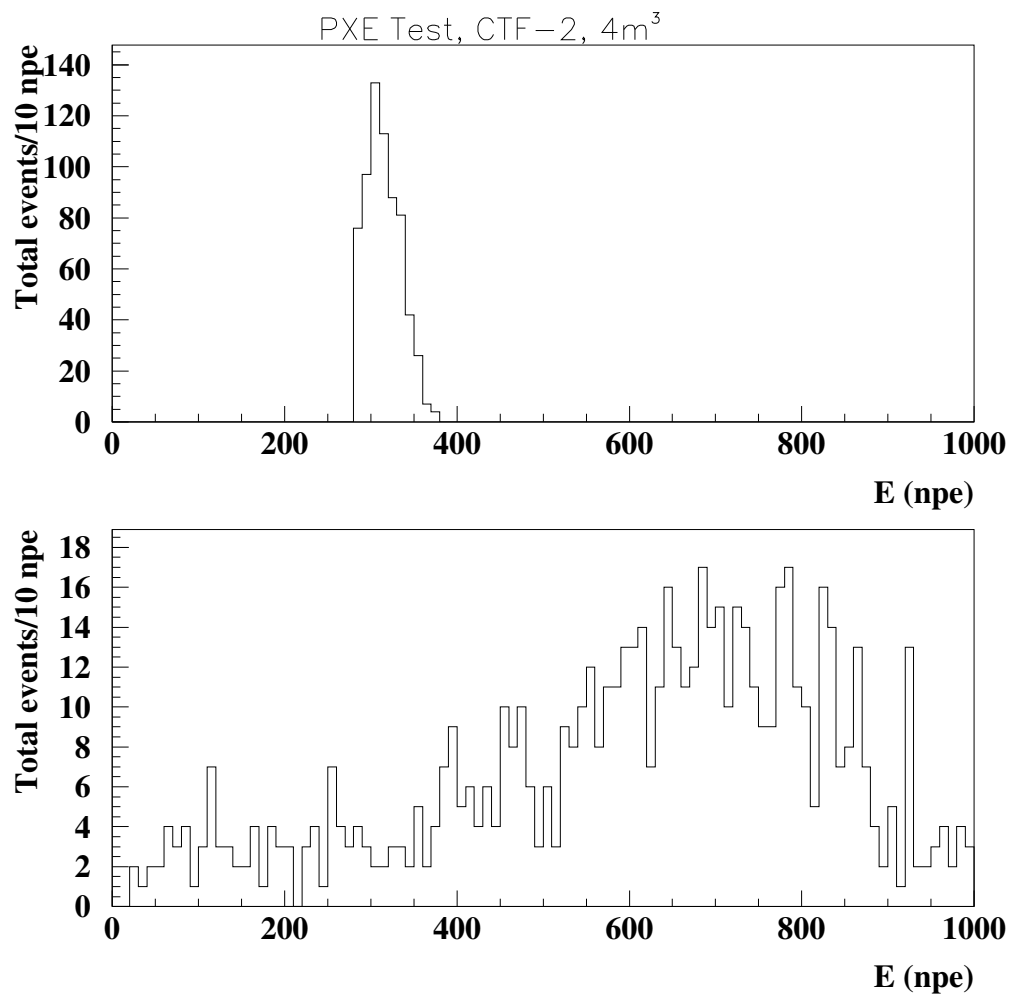


Figure 5.8: Energy spectrum of the two clusters of events used for α/β discrimination analysis. The upper is the ^{214}Po α and the lower is the ^{214}Bi beta spectrum.

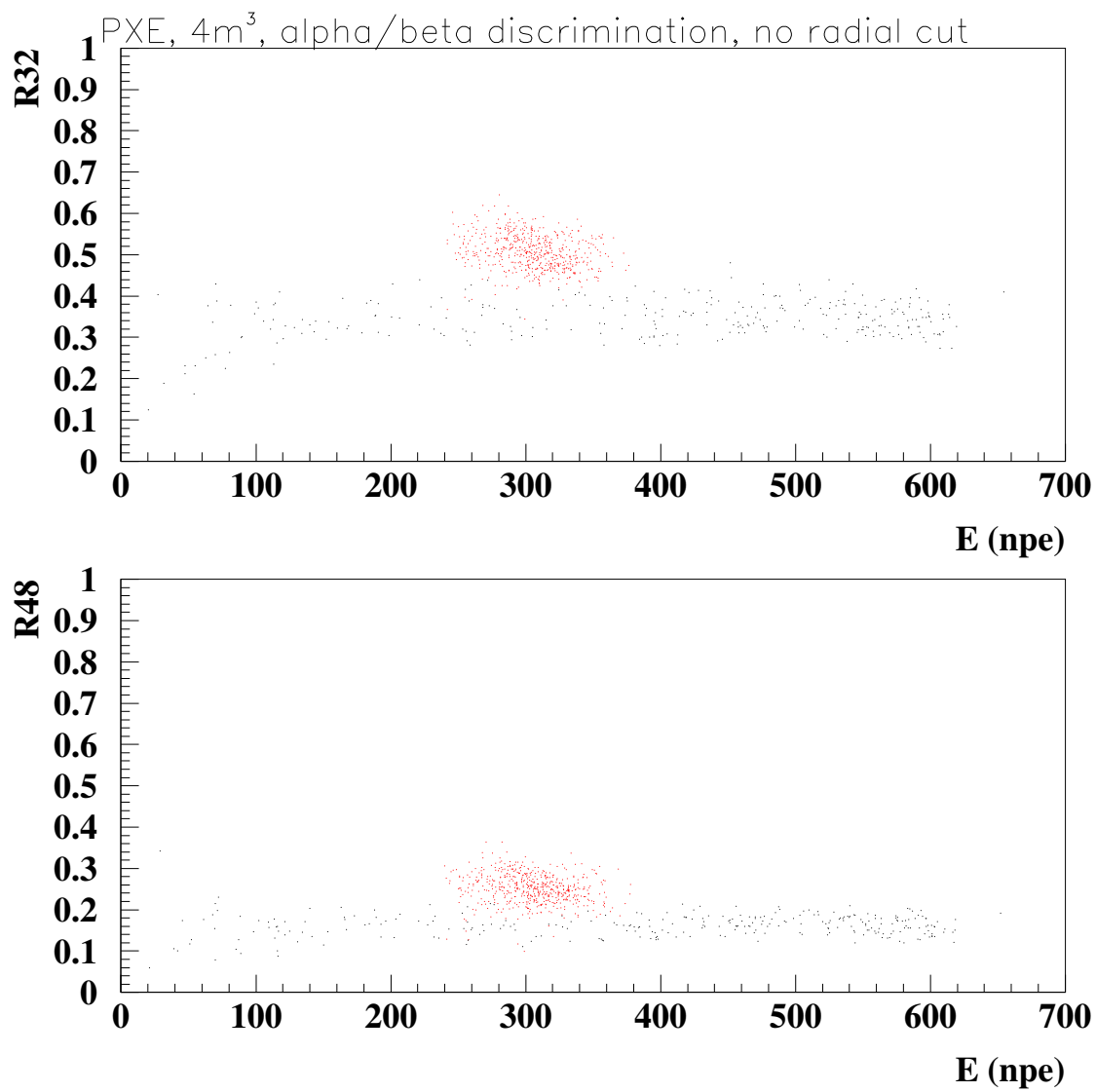


Figure 5.9: α/β discrimination capability in 4m³ of PXE. The ratio "tail/total" is plotted for a delay of 32 nsec in the upper plot and 48 nsec in the lower one. No radial cuts are applied.

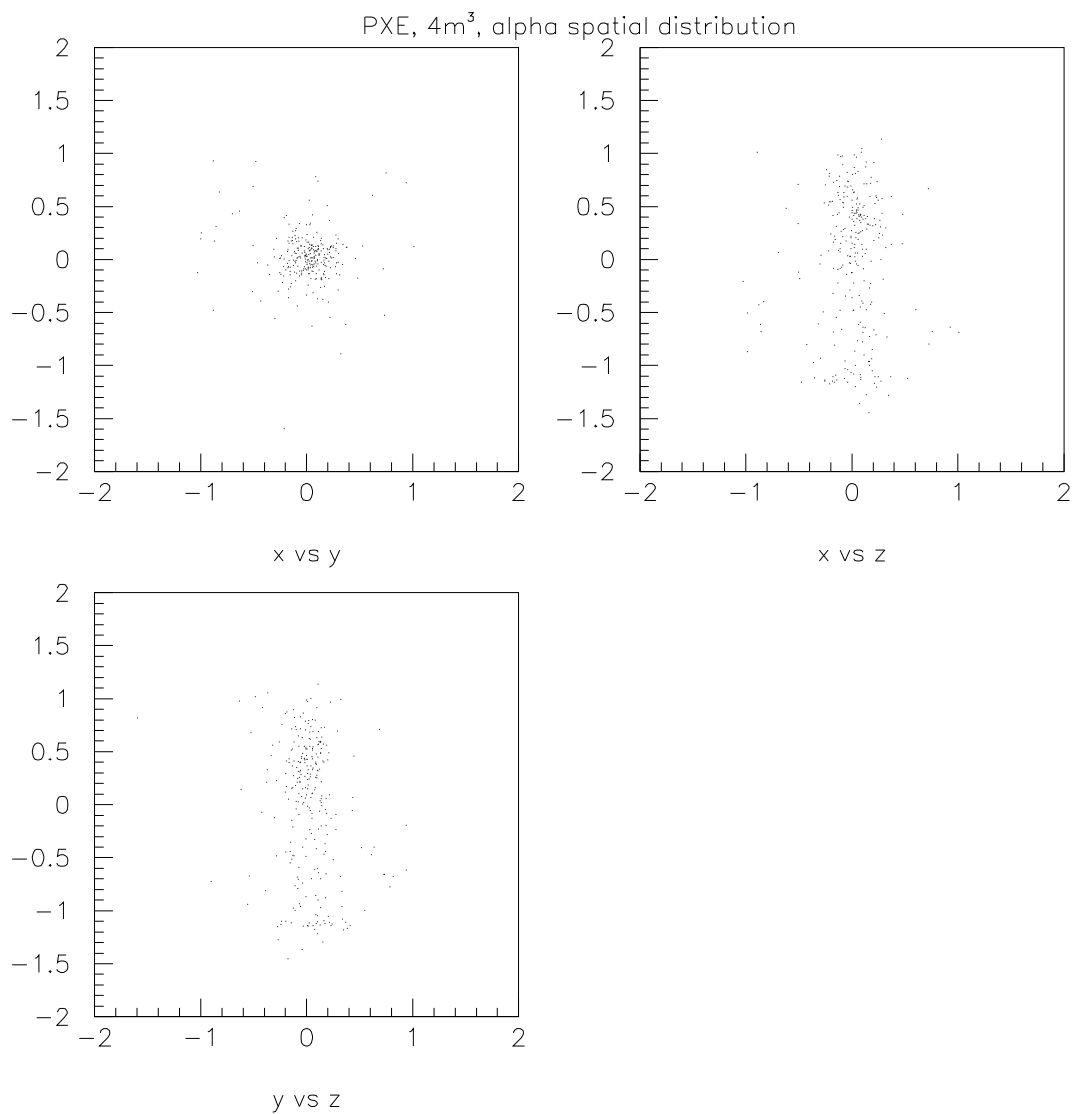


Figure 5.10: Spatial distribution of ^{214}Po alpha events during the last period of data taking. The rate during this runs was ~ 20 counts/day constant. The disuniform distribution suggests the presence of an internal or a surface radon source.

5.2.3 ^{40}K Contamination

^{40}K decays via two different channels:

$$^{40}\text{K} \rightarrow ^{40}\text{Ca}(\beta^-, 89.3\%B.R.) \quad (5.9)$$

$$^{40}\text{K} \rightarrow ^{40}\text{Ar}(\beta^+, EC, 10.7\%B.R.) \quad (5.10)$$

The former is a β^- decay ($Q=1.3$ MeV) and the latter is an electron capture with a γ emission of energy 1.46 MeV. A peak that can fit very well the γ emission of ^{40}K was observed on the data (Fig. 5.12) but the corresponding β emission was strongly suppressed. Moreover, the spatial reconstruction shows that the peak is shifted to higher values of z (Fig. 5.11). The missing β events can be explained if the source of the contamination is not internal but on the surface or outside the IV. Different scenarios were studied [9]:

- *IV nylon film*: in order to explain the potassium observed, this contamination should be two orders of magnitude higher than the value measured of 3 ppb (Tama '94). Moreover, the expected spatial distribution will be uniform.
- *Vectran ropes*: the IV is hold down with Vectran strings that pass on the higher hemisphere of the vessel. The strings are 1 mm thick and electron herein produced can pass the 0.05 cm IV membrane. The measured contamination is 45 ppm and in order to explain the contamination observed 31 ppm are needed. Due to the arrangement of the string a disuniformity versus higher z is expected.
- *Nylon endcaps*: the potassium contamination in these parts is 0.6 ppm and the value requested to explain the measure is ~ 32 ppm.
- *Nylon pipes*: also in this case the measured potassium contents of 1-3.6 ppm do not match the contamination requested in order to explain the data of ~ 12.5 ppm.

In Fig. 5.13 are reported the MonteCarlo energy spectra of the possible ^{40}K sources: internal, IV nylon, Vectran ropes, nylon endcaps and nylon pipes [9]. The comparison between simulated spectra and CTF-2 data for different scenarios is reported in Fig. 5.14.

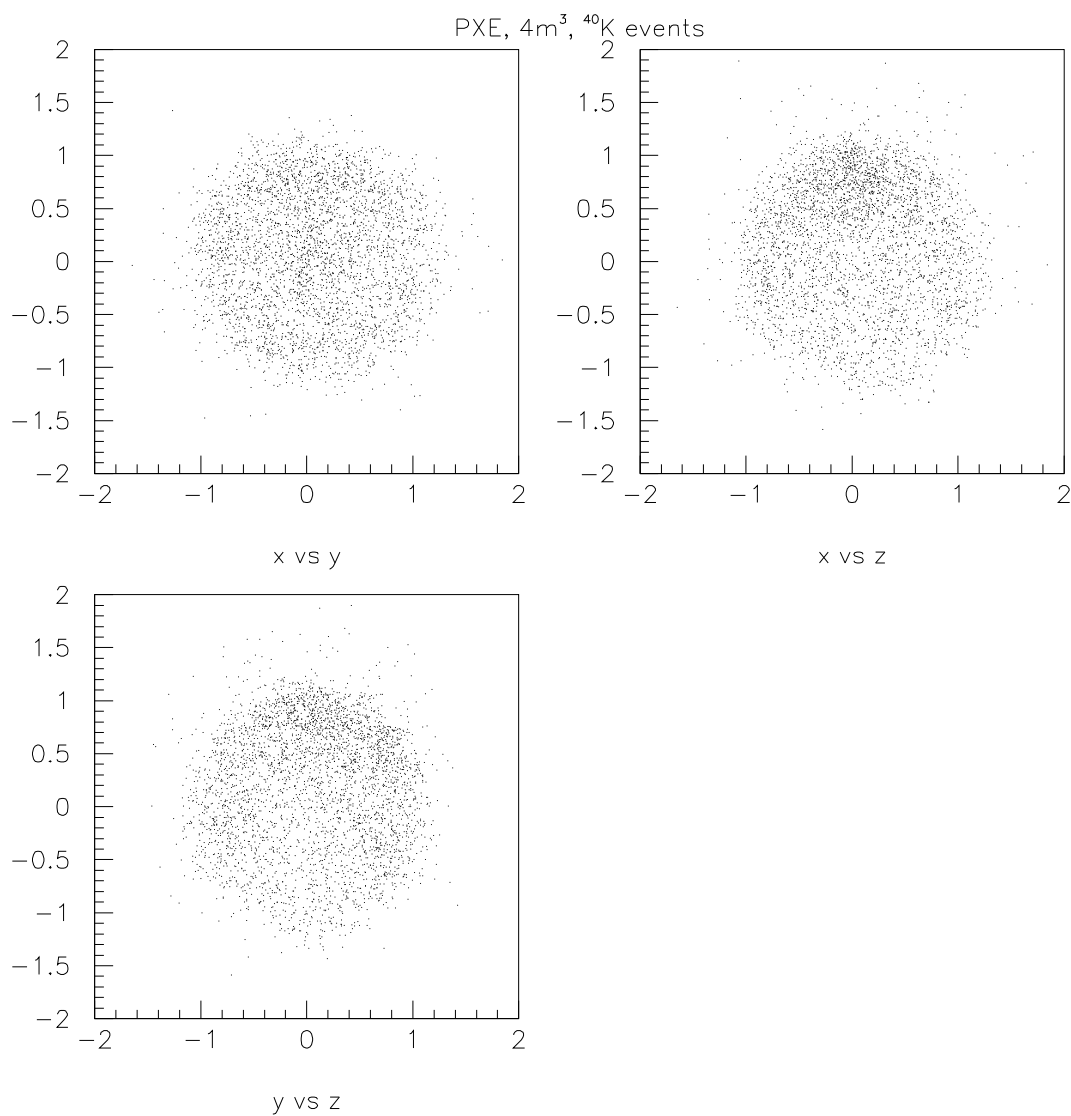


Figure 5.11: Spatial distribution of ⁴⁰K events. The increased event rate on the upper part of the IV suggested the string to be the origin of the contamination.

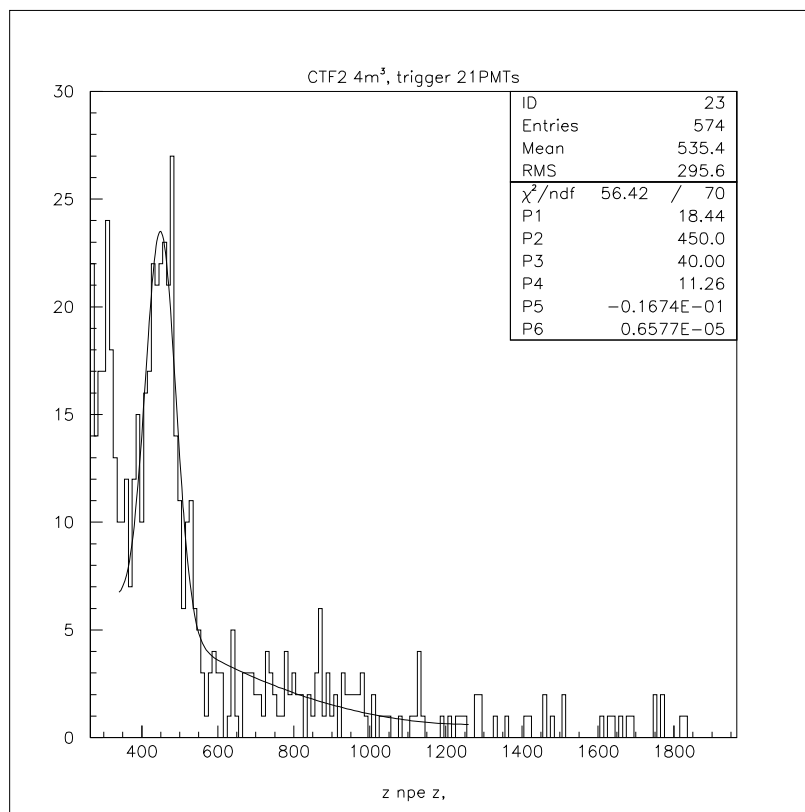


Figure 5.12: Energy spectra of Group 1 events with muon cuts applied. The peak is fitted with a 2nd degree polynomial in order to disentangle a possible background and a Gaussian. The corresponding potassium activity is ~ 200 counts/day.

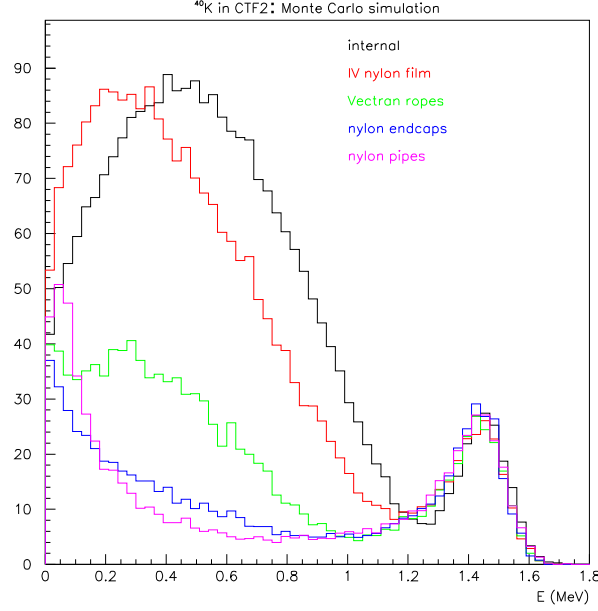


Figure 5.13: Simulated energy spectra from different ^{40}K sources in CTF-2 [9].

5.2.4 Limit of ^{238}U Contents in PXE

In CTF uranium (^{238}U) is assayed via the characteristic decay sequence of its daughters ^{214}Bi and ^{214}Po . Assuming secular equilibrium of the total decay chain, the “Bi-Po-rate” can be expressed as uranium-equivalent; a Bi-Po-rate of 1.35/d/ton corresponds to a concentration of 10^{-15}gU/g .

Data taking with 4m^3 of PXE lasted for 52 days. The radon contamination introduced during filling was small (90 counts per day), hence, the measuring period was sufficiently long such that the initial radon had time to decay away ($\tau(\text{Rn}) = 5.48$ days). We observed however after an initial decrease a constant Bi-Po rate indicating an internal source. Moreover, as shown in Fig. 5.10, it emerged that the radon was not uniformly distributed. Basically all events were detected close to the central vertical axis (z-axis). Performing a spatial analysis of the Bi-Po event distribution, we could derive a limit on the intrinsic uranium concentration of the PXE under investigation. The result obtained is

$$^{238}\text{U} = (7.3 \pm 2.4) \cdot 10^{-16} \text{g/g} \quad (5.11)$$

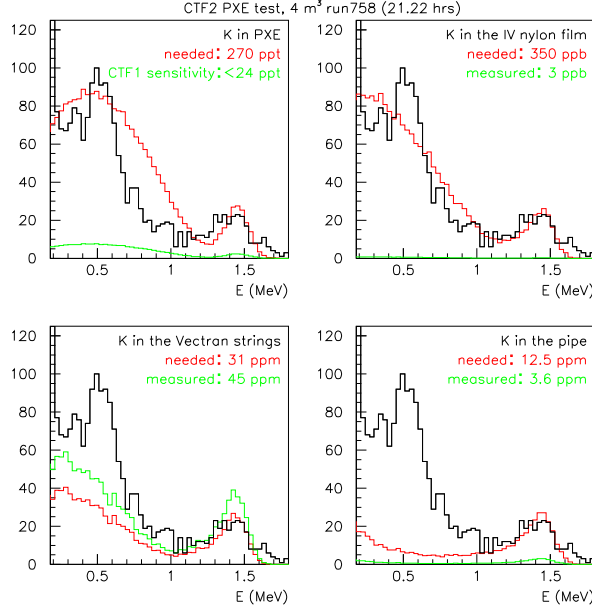


Figure 5.14: Comparison between simulated scenarios and CTF-2 data [9].

I discuss here the main steps of the analysis.

The thesis that I will demonstrate here is that the Bi-Po events detected come from three sources:

- 1) *Radon from the external environment*: during filling a certain amount of radon is introduced in PXE (n_{Rn}). This source must be uniformly distributed inside the IV and decay with the mean life of ^{222}Rn ($\tau(Rn)$).
- 2) *Radon from an “unknown” source*: a group of events is reconstructed inside a vertical cylinder (n_{cyl}) and is constant in time.
- 3) *Radon from ^{226}Ra supposed in secular equilibrium with ^{238}U* : the ^{238}U intrinsically contained in PXE produces a certain amount of Bi-Po events (n_{238U}) uniformly distributed in the scintillator and constant in time.

The observations that bring us to this thesis are:

- i) The total rate of Bi-Po events (n) decays with a mean life (τ_{tot}) longer than the mean life of ^{222}Rn (τ_{Rn}):

$$n(t) = n(0) \cdot e^{-t/\tau_{tot}} \quad (5.12)$$

The first scenario studied is the simplest: a constant background internal source (k) is present.

$$n(t) = n(0)e^{-t/\tau_{Rn}} + k \quad (5.13)$$

For large t , $n(t) \rightarrow k$. Considering the last period of data taking we found indeed $n(t) \sim 1 \text{ count/hour} = k$. Studying the distribution of the Bi-Po events $n(t) - k$ we found that the remaining count rate decay with $\tau \sim \tau_{Rn}$ (Fig. 5.15).

- ii) The spatial reconstruction code reconstructs the constant background events along z axis inside a cylindrical region (Fig. 5.16).
- iii) The source calibration showed that the reconstruction code works even if no optimization for the PXE was done [10] (Fig. 5.17). On the basis of this result it is possible to exploit the spatial distribution in the analysis.
- iv) If we consider ^{14}C as monitor of the detector performances we can observe that it is reconstructed uniformly inside the IV (Fig. 5.18). No intrinsic disuniformity in the data is observed. The Bi-Po events reconstructed inside the vertical cylinder are a peculiarity.
- v) The Bi-Po events present the correct coincidence time and the correct energy spectrum (Fig. 5.19). No misidentification of ^{214}Po events is observed.
- vi) A spatial analysis is applied in order to disentangle the different radon sources. We subtract from the total IV the volume inside a cylinder of radius R_C and we consider the Bi-Po contents of the remaining volume as uranium daughters. The last two periods of continuous data taking are analyzed. Period 1 lasted 6.66 days (Run 774 - Run 781) and Period 2 5.8 days (Run 784 - Run 788). They are separated by an interval of 60 hours. The Bi-Po events detected in the different volumes and the ^{238}U equivalent activity is evaluated and reported in Tab. 5.6. The α events of ^{214}Po are selected as group 2 events with a coincidence time in the interval $50 \mu\text{sec} - 1000 \mu\text{sec}$ (Efficiency 82.5%) and energy in the interval 250-380 pe (Efficiency 97.9%).

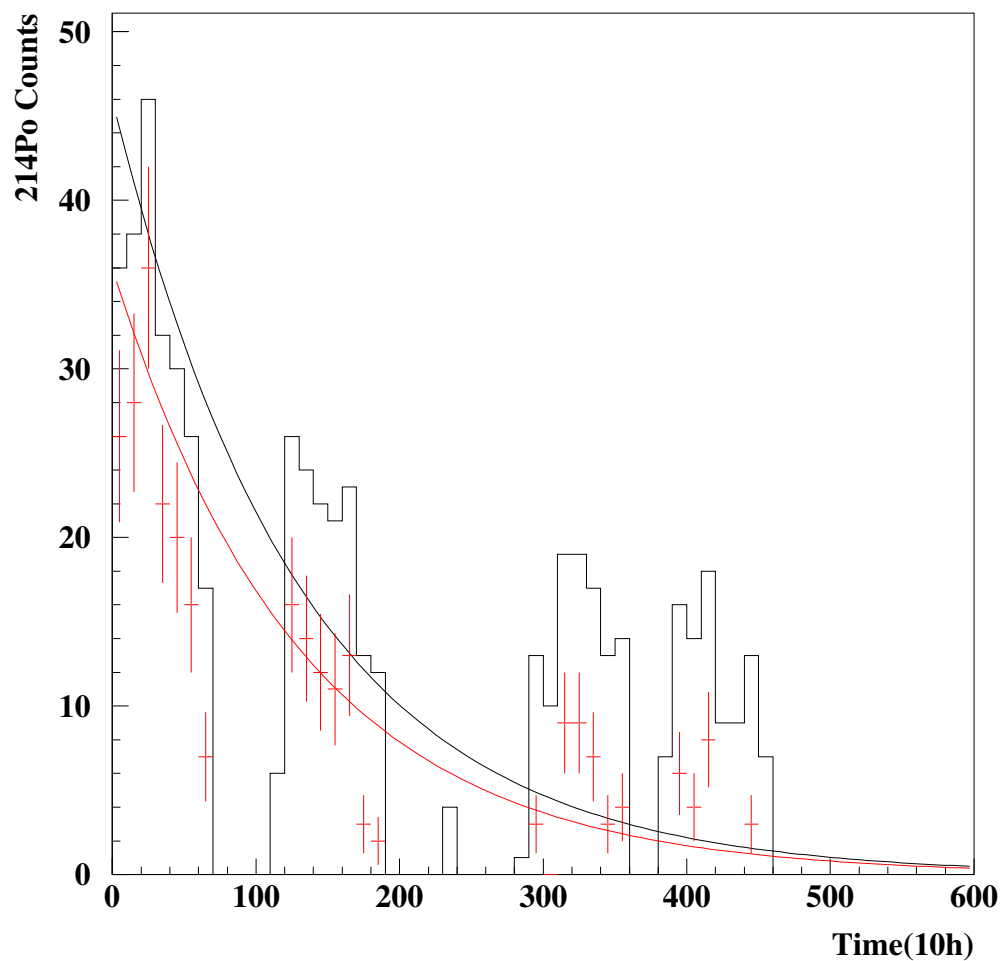


Figure 5.15: Count rate of Bi-Po events before and after the subtraction of a constant value k (1 count per hour). In black (upper plot) is reported the total time distribution of Bi-Po events and the ^{222}Rn decay curve normalised on the first bins. In red (lower plot) is the distribution of Bi-Po events after the subtraction of the constant background k and the relative decay curve.

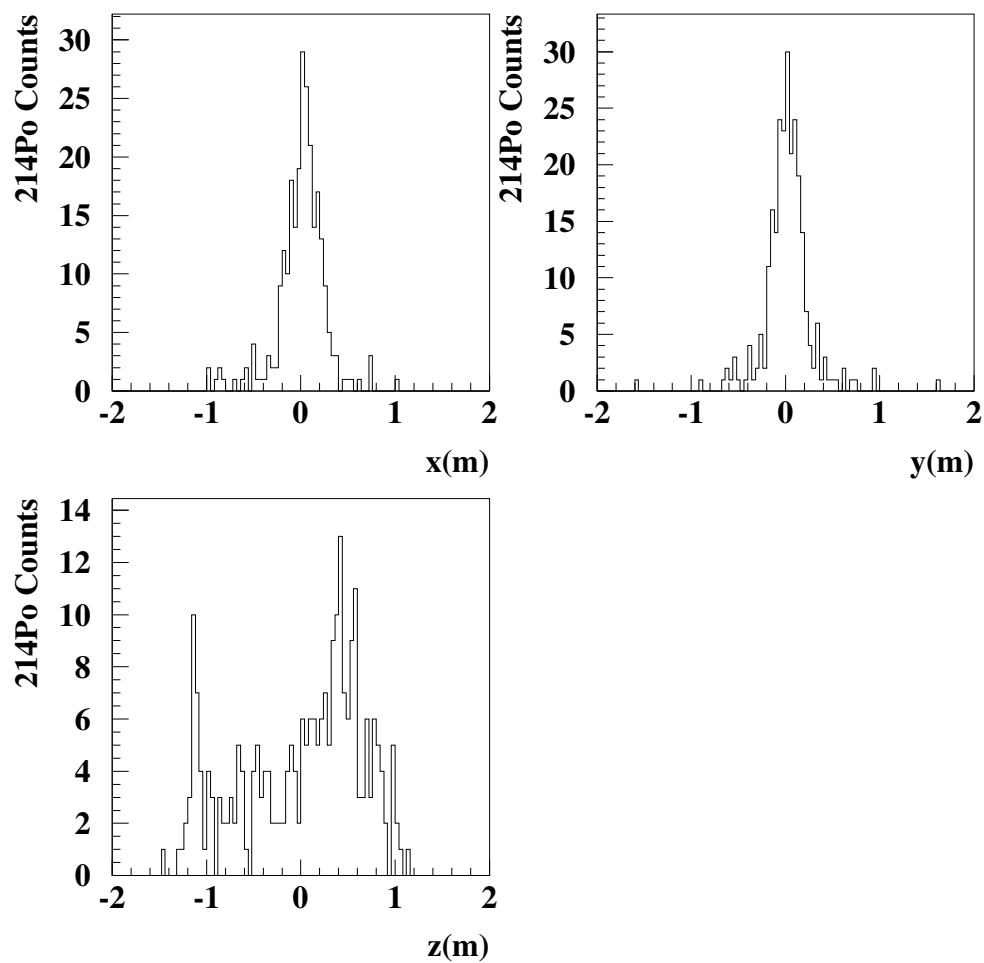


Figure 5.16: Spatial reconstruction of Bi-Po events during the last period of data taking (Run 777 – Run 789).

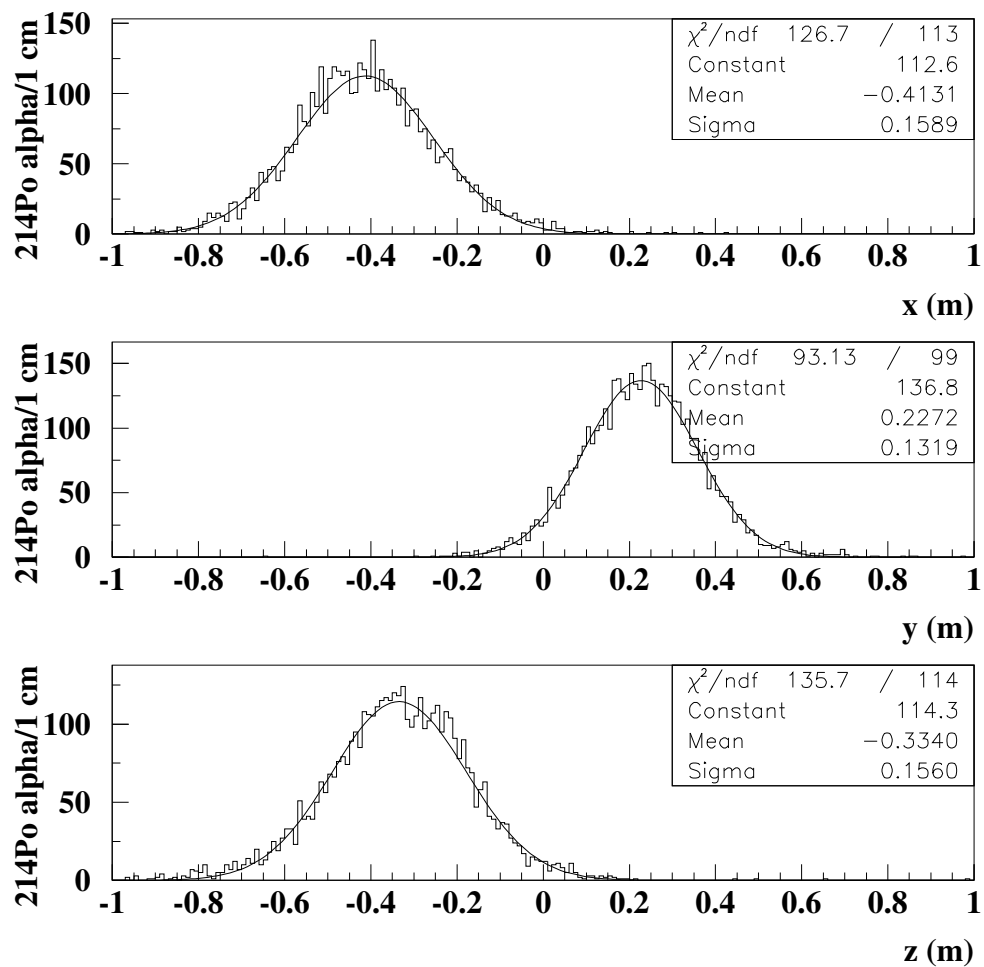


Figure 5.17: Radon source in CTF-2. The nominal position of the source is $x=-40\text{cm}$, $y=27\text{cm}$, $z=-30\text{cm}$ (Run 801). No optimisation of the reconstruction code for PXE is applied.

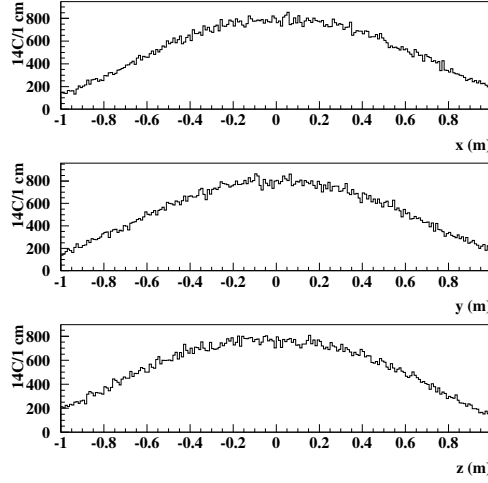


Figure 5.18: ^{14}C reconstructed events (20-50 pe) used as monitor of the reconstruction. No disuniformity is present.

5.3 Final Results: Single Counts

The results obtained with the previous analysis can be summarized in the plot reported in Fig. 5.21.

The energy calibration obtained fitting ^{14}C spectra (311 pe/MeV) is applied to all the energy range of interest. A confirmation of the linearity of the calibration comes from radon alphas and potassium gamma peaks. The raw spectrum is compared with the spectrum obtained after the rejection of muon events and alphas events and after the definition of a fiducial volume. The subtractions are realized applying different cuts studied in the previous sections.

Čerenkov events represent a background that influence the overall spectra. It has to be subtracted with a very high efficiency in CTF and in Borexino. In CTF-2 the muon cuts are realized via software cuts and not via a hardware veto as will be in Borexino (the muon veto system installed in CTF-2 was not yet optimised during this data taking). The efficiency of this *standard cuts* is high in the NW (250-800 keV) (99%) but decreases at higher energy.

^{222}Rn and ^{218}Po alpha decays appear inside the NW. For this reason they represent

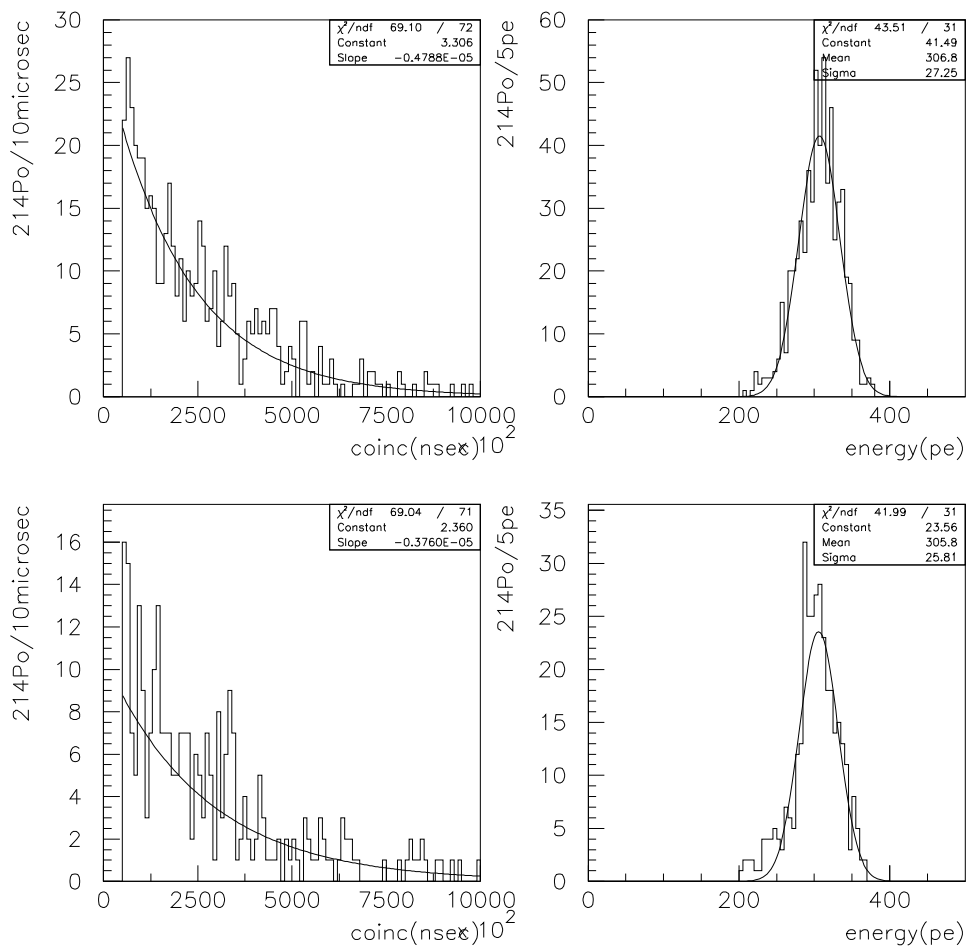


Figure 5.19: Coincidence time and energy spectrum of ^{214}Po events. The upper spectra concern the events outside the cylinder ($R_C > 0.2m$) and the lower ones inside ($R_C < 0.2m$).

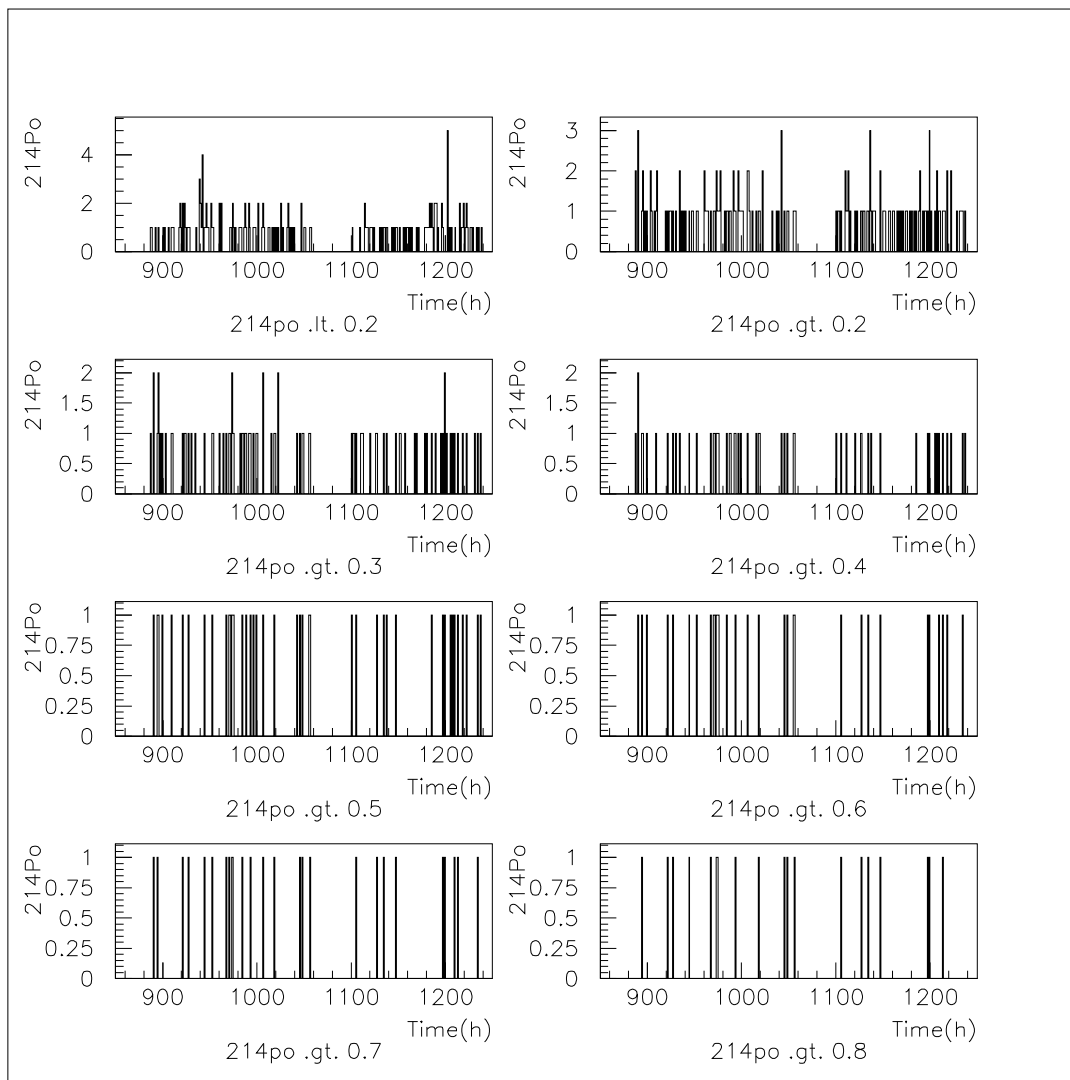


Figure 5.20: ^{214}Po events inside and outside the cylindrical region of R_C during the last 10 days of data taking. Time 0 is the first hour of $4m^3$ data taking.

Space Cut (m)	Mass (ton)	Period 1 (counts)	$^{238}U_{eq}$ ($10^{-15}g/g$)	Period 2 (counts)	$^{238}U_{eq}$ ($10^{-15}g/g$)
$R_C > 0.2$	3.93	89	3.1 ± 0.3	74	2.9 ± 0.3
$R_C > 0.3$	3.64	53	2.0 ± 0.3	36	1.5 ± 0.2
$R_C > 0.4$	3.23	35	1.5 ± 0.2	20	0.96 ± 0.2
$R_C > 0.5$	2.72	27	1.4 ± 0.2	17	0.96 ± 0.2
$R_C > 0.6$	2.14	21	1.3 ± 0.3	10	0.73 ± 0.2
$R_C > 0.7$	1.51	17	1.5 ± 0.4	9	0.96 ± 0.3
$R_C > 0.8$	0.92	12	1.8 ± 0.5	7	1.2 ± 0.4
$R_C < 0.2$	0.25	93	51 ± 5	75	47 ± 5

Table 5.6: Results of $^{238}U_{eq}$ analysis: R_C =radius vertical cylinder considered; Period 1 (6.66 days) and Period 2 (5.80 days) are the last two periods of data taking before the source test. During these periods radon contamination from external environment has completely decayed. $10^{-15}gU/g = 1.35/d/ton$. The activity is recorrect for the efficiency of the cuts applied in order to identify ^{214}Po α events.

a very serious concern for Borexino internal background. We observed that a cut on the ratio tail (32 nsec) to total charge greater than 0.4 is very efficient in rejecting alpha events in the energy region $\sim 1MeV$. I applied this cut on the overall spectrum.

After source calibration we know that the reconstruction code works. Defining a fiducial volume we reject external and surface background. The residual events after all the cuts applied are alphas of radon in the NW and gamma of potassium. The single counts corresponding to the different cuts applied are reported in Tab. 5.7.

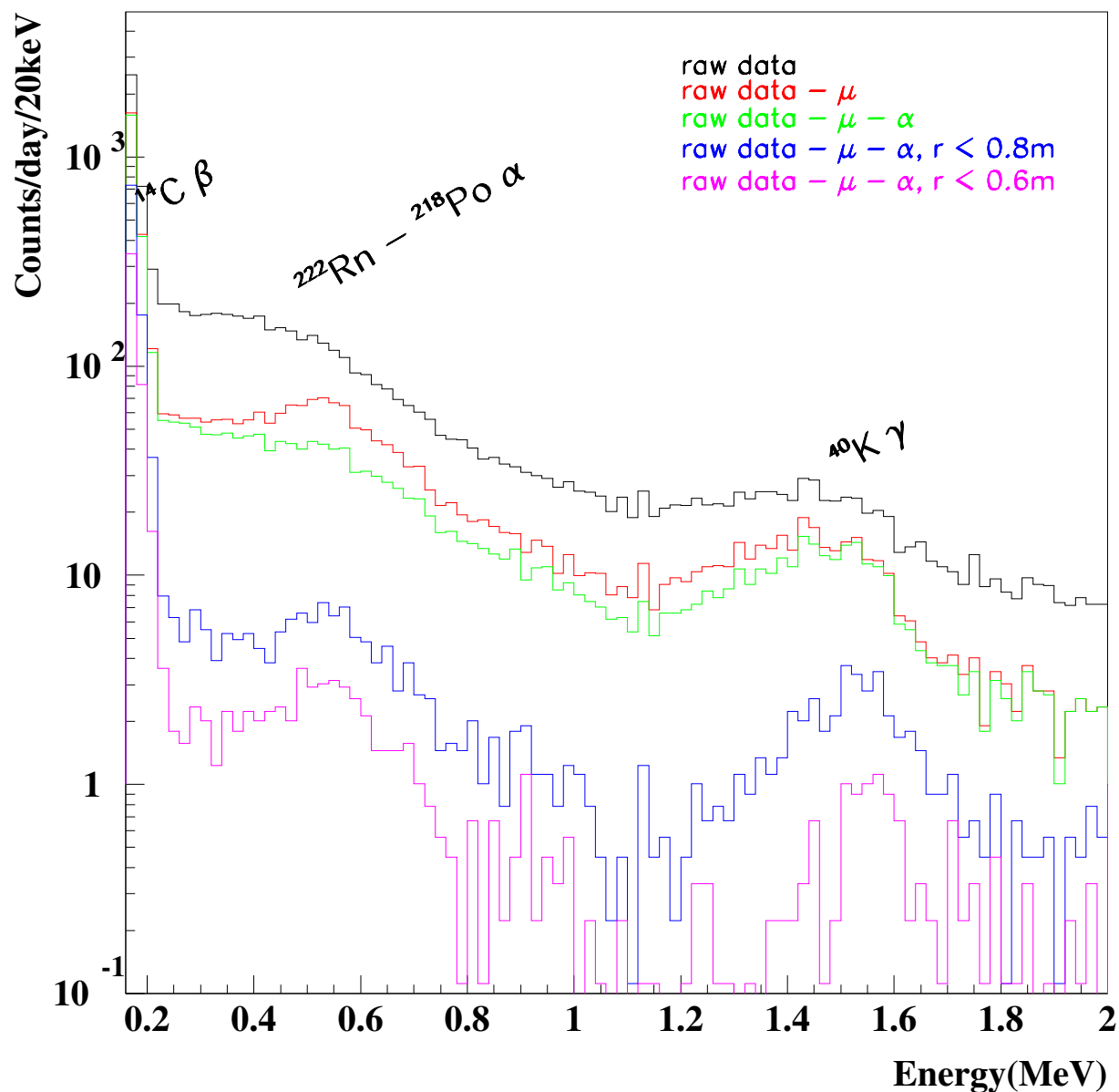


Figure 5.21: Energy spectra in MeV of the CTF-2 data taking. The energy calibration applied is 311 pe/MeV as extracted from ^{14}C spectrum. Cherenkov events are subtracted using standard cuts. Alphas are reduced using $R32 > 0.4$. Radial cuts are applied using Milan spatial reconstruction code.

	NW (c/day/4 ton)	$\geq NW$ (c/day/4 ton)
Raw Data	3411	1208
Raw Data - μ	1399	570
Raw Data - μ - α	1031	460
Raw Data - μ - α , $r < 0.8$	256	137
Raw Data - μ - α $r < 0.6$	245	83

Table 5.7: Count rate in CTF-2 inside and outside the Neutrino Window (250-800keV). Progressively cuts before studied are applied. All the rates are expressed in counts per day per the entire IV mass of PXE that is 4 tons.

Bibliography

- [1] M. Goeger, Privat Communication.
- [2] Borexino Coll., Physics Letters B 422 (1998) 349-358.
- [3] A. Garcia, B.A. Brown, Phys. Rev. C 52 (1995) 3416.
- [4] P. Lombardi, Tesi di Laurea, Politecnico di Milano (1997).
- [5] S. Schoenert, Private Communication.
- [6] C. Hagner, S. Schoenert, *Loading the Inner Vessel of CTF2 with PXE*, Borexino Project, Test Procedure TEST-BX-004.
- [7] Oleg Smirnov, Private Communication.
- [8] G. Ranucci, A. Goretti, P. Lombardi, NIM A 412 (1998) 374-386.
- [9] L. Cadonati, *Potassium Peak in the CTF2 Data*, Borexino Internal memo, Aug. 27 (2000).
- [10] M. Goeger, *Memo on the Source Tests in CTF2*, Privat Communication.

Description of the Data Taking

I report here the list of good runs that can be used for data analysis. Moreover, I describe here how to recover groups of runs where problems like dead time or other hardware problems are present.

Run 715 - Run 716: Water Runs.

Run 717: $1m^3$ PXE. 6 PMTs in trigger. Dead time $\sim 50\%$. The group 1 events can be reincorrect. The group 2 events are not reliable.

Run 724: $3m^3$ PXE. 6 PMTs in trigger. 43% dead time. For the Group 2 only the first 366700 events are good.

Run 725: $3m^3$ PXE. 6 PMTs in trigger. 43% dead time. For the Group 2 only the first 50000 events are good.

Run 726: $3m^3$ PXE. 6 PMTs in trigger. 43% dead time. For the Group 2 only the first 50500 events are good.

Run 728: $3m^3$ PXE. 6 PMTs in trigger. 43% dead time. For the Group 2 only the first 100000 events are good.

Run 729: $3m^3$ PXE. 6 PMTs in trigger. 43% dead time. For the Group 2 only the first 376200 events are good.

Run 736: $3m^3$ PXE. 6 PMTs in trigger. 43% dead time. For the Group 2 only the first 300000 events are good.

Run 737: $3m^3$ PXE. 6 PMTs in trigger. 43% dead time. For the Group 2 only the first 150000 events are good.

Run 738: $3m^3$ PXE. 6 PMTs in trigger. 43% dead time. For the Group 2 only the first 250000 events are good.

Run 739: $3m^3$ PXE. 6 PMTs in trigger. 43% dead time. For the Group 2 only the first 100000 events are good.

Run 740: $3m^3$ PXE. 6 PMTs in trigger. 43% dead time. For the Group 2 only the first 475000 events are good.

Run 741: $3m^3$ PXE. 8 PMTs in trigger. 27% dead time. For the Group 2 only the first 150000 events are good.

Run 742: $3m^3$ PXE. 10 PMTs in trigger. 21.5% dead time. For the Group 2 only the first 26000 events are good.

Run 743: $3m^3$ PXE. 10 PMTs in trigger. 21.5% dead time. For the Group 2 only the first 43000 events are good.

Run 744: $3m^3$ PXE. 13 PMTs in trigger. 20% dead time. For the Group 2 only the first 47100 events are good.

Run 745: $3m^3$ PXE. 13 PMTs in trigger. 20% dead time. For the Group 2 only the first 132400 events are good.

Run 746: $3m^3$ PXE. 13 PMTs in trigger. 20% dead time. For the Group 2 only the first 12000 events are good.

Run 747: $3m^3$ PXE. 21 PMTs in trigger. 0.02% dead time. For the Group 2 only the first 750000 events are good.

Run 749: $3m^3$ PXE. 21 PMTs in trigger. For the Group 2 only the first 100000 events are good.

Run 750: $3m^3$ PXE. 21 PMTs in trigger.

Run 756: $3m^3$ PXE. 21 PMTs in trigger.

Run 758-759-760: $4m^3$ PXE. 21 PMTs in trigger.

Run 761: $4m^3$ PXE. 21 PMTs in trigger. This run has to be reconstruct with the following modification in the source code:

```
char comments[80]
```

```
char comments1[80]
```

Run 763-764-767-768-769-770-771-772-773-774-775-776-777-778-779-781: $4m^3$ PXE. 21 PMTs in trigger.

Run 783-784-785-786-787-788: $4m^3$ PXE. 21 PMTs in trigger.

Run 791-793-795: $4m^3$ PXE. 21 PMTs in trigger. Radon source number 1.

Run 797-798-799-800-801-802-803-804-805-807-809-810: $4m^3$ PXE. 21 PMTs in trigger. Radon source number 2.

Acknowledgments

At the end of this human and scientific experience I want to thank all the collaborators and friends that made this work possible.

I am in debt to Prof. Giulio Manuzio, my tutor. He gave me the possibility to carry out my research project independently at the Gran Sasso laboratories. This was possible only because I had his support and friendship.

Thanks to Prof. Gianpaolo Bellini, spokesperson of the Borexino collaboration. He gave me responsibilities inside the CTF-2 working group though it was my first experience. I had the chance to learn and to challenge myself every day.

Thanks to the PMT working group. In particular to Gioacchino Ranucci, Paolo Lombardi, George Korga, Laslo Papp and Augusto Brigatti. Sealing 120 PMTs for CTF-2 was an experience!

Caren Hagner, Marianne Neff, Roger von Hentig, K.H. Schuhbeck, Stefan Schönert thank you! During the installation of CTF-2 PMTs I learned how to work hard in a friendly atmosphere.

To the Gran Sasso engineers Roberto Tartaglia, Stefano Gazzana and Augusto Goretti a big "grazie" for supporting the CTF-2 team underground during a very hot period for the installation of Borexino.

Thanks to the "woman team" Prof. Emanuela Meroni, Prof. Silvia Bonetti, Barbara Caccianiga, Laura Cadonati, Marianne Neff and Caren Hagner. I enjoyed making data analysis and all the useful discussions.

I appreciated the right words at the right moment of Steve Kidner.

The lovely and relaxing moments that I spent with all the Gran Sasso friends Matthias, Alessandra, Alba, Cristina, Francesco, Nicola, Michael, York, George, Laslo, Paolo, Stefano, Augusto were fundamental during the daily life at the laboratory.

To my parents, to Silvia and Paolo, and to my German family: I love you. To my little Emil: you are my best result. To Stefan: I can't find the right words to thank you and to express all my love.